

---

Universität Duisburg-Essen

Fakultät für Physik

---

# Ab initio investigation of ground-states and ionic motion in particular in zirconia-based solid-oxide electrolytes

Von der Fakultät für Physik der Universität Duisburg-Essen zur  
Erlangung des akademischen Grades eines Doktors der  
Naturwissenschaften (Dr. rer. nat.) genemigte Dissertation

von *Julian Arndt Hirschfeld*

aus Meerbusch

Tag der Disputation: 11.12.2012  
Gutachter: PD Dr. Hans Lustfeld  
Prof. Dr. Peter Entel  
Prof. Dr. Lars Bergqvist





# Contents

<b>1. Introduction</b>	<b>7</b>
<b>2. Fuel cell functionality</b>	<b>13</b>
2.1. Operating principle . . . . .	13
2.2. Thermodynamic aspects . . . . .	15
2.3. Fuel cell polarization . . . . .	18
2.3.1. Activation overpotential . . . . .	18
2.3.2. Ohmic overpotential . . . . .	20
2.3.3. Concentration overpotential . . . . .	21
2.3.4. The fuel cell polarization curve . . . . .	21
2.4. Fuel cell efficiency . . . . .	23
2.5. Fuel cell types . . . . .	26
2.5.1. Proton exchange membrane fuel cell (PEMFC) . . . . .	26
2.5.2. Direct methanol fuel cell (DMFC) . . . . .	27
2.5.3. Alkaline fuel cell (AFC) . . . . .	27
2.5.4. Solid oxide fuel cell (SOFC) . . . . .	28
<b>3. Electronic Structure Calculations</b>	<b>31</b>
3.1. Density Functional Theory . . . . .	31
3.1.1. Hohenberg-Kohn Theorem . . . . .	32
3.1.2. Kohn-Sham Equations . . . . .	34
3.1.3. Exchange-Correlation Approximations . . . . .	35
3.2. Vienna Ab Initio Package (VASP) . . . . .	36
3.2.1. Plane Wave Expansion and Brillouin zone sampling . . . . .	36
3.2.1.1. Plane wave basis set . . . . .	36
3.2.1.2. Charge density in the plane wave expansion and Brillouin zone sampling . . . . .	38
3.2.2. Determining the electronic ground state . . . . .	39
3.2.3. Ionic relaxation . . . . .	40
3.2.4. Projector Augmented Wave Method (PAW) . . . . .	43
<b>4. Transition States and their determination</b>	<b>45</b>
4.1. Transition State Theory . . . . .	45
4.1.1. The diffusion rate . . . . .	46
4.2. Ionic Conductivity . . . . .	50
4.2.1. Crystal defects . . . . .	50
4.2.2. Phenomenological description of the ionic conductivity . . . . .	52

4.3.	Determination of the Transition State . . . . .	53
4.3.1.	Finding the minimum energy pathway . . . . .	53
4.3.2.	Nudged Elastic Band Method . . . . .	54
<b>5.</b>	<b>A new NEB based optimization scheme</b>	<b>59</b>
5.1.	NEB in the neighborhood of a minimum . . . . .	60
5.2.	The MsNEB Algorithm . . . . .	62
5.3.	Applications . . . . .	65
5.3.1.	Finding the most stable isomer of the $P_4$ cluster . . . . .	66
5.3.2.	Finding the most stable isomer of the $P_8$ cluster . . . . .	66
<b>6.</b>	<b>Electrolyte materials</b>	<b>73</b>
6.1.	SOFC electrolytes . . . . .	73
6.1.1.	Requirements to SOFC electrolyte materials . . . . .	73
6.1.2.	Yttrium Stabilized Zirconia (YSZ) and Scandium Stabilized Zirconia (SSZ) . . . . .	74
6.1.3.	Other electrolyte materials under development . . . . .	75
6.2.	Zirconium-dioxide $ZrO_2$ . . . . .	76
6.2.1.	Zirconia Phases . . . . .	76
6.2.2.	Electronic properties of zirconia . . . . .	78
6.2.3.	Charged vacancies in zirconia . . . . .	79
<b>7.</b>	<b>Strain Dependent migration barrier</b>	<b>87</b>
7.1.	Strain dependence in $ZrO_2$ . . . . .	87
7.1.1.	Ab initio approach . . . . .	87
7.1.1.1.	DFT Calculations . . . . .	87
7.1.1.2.	DFT Results . . . . .	89
7.1.2.	Analytic Approach . . . . .	93
7.1.2.1.	Model Description . . . . .	93
7.1.2.2.	Model Results . . . . .	95
7.2.	Strain dependence in YSZ . . . . .	97
7.2.1.	Low-doped YSZ . . . . .	98
7.2.2.	High-doped YSZ . . . . .	101
7.2.3.	Yttrium at the barrier position . . . . .	102
7.3.	Strain dependence in SSZ . . . . .	105
7.4.	Discussion of strain induced effects in doped zirconia . . . . .	106
<b>8.</b>	<b>Anisotropic YSZ</b>	<b>111</b>
8.1.	The layered structure . . . . .	111
8.2.	Stability considerations . . . . .	114
8.3.	Vacancy-Vacancy interactions . . . . .	117
8.4.	Molecular Dynamics . . . . .	123
8.4.1.	Computational Results . . . . .	124
8.5.	Conclusions . . . . .	127

---

<b>9. Summary</b>	<b>129</b>
<b>A. Appendix</b>	<b>131</b>
A.1. Solvers for eigenvalue problems . . . . .	131
A.1.1. Blocked Davidson algorithm (DAV) . . . . .	131
A.1.2. Residual minimization scheme, direct inversion in the iterative sub- space (RMM-DIIS) . . . . .	132
A.2. Charge mixing methods . . . . .	133
A.2.1. Broyden Mixing . . . . .	133
A.2.2. Kerker Mixing . . . . .	134
A.3. Consideration of ion fixing for the barrier height in strained zirconium oxide	134



# Erklärung über vorherige Publikationen

Aus Gründen des wissenschaftlichen Fortschritts und um die Prioritäten zu sichern, sind Teile dieser Dissertation bereits in den zwei Zeitschriften, Physical Review B und Physical Review E veröffentlicht.

1. J. A. Hirschfeld, H. Lustfeld, “First-principles study and modeling of strain-dependent ionic migration in  $ZrO_2$ ”, Physical Review B **84**, 224308 (2011).
2. J. A. Hirschfeld, H. Lustfeld, “Finding stable minima using a nudged-elastic-band-based optimization scheme”, Physical Review E **85**, 056709 (2012).

Diese Veröffentlichungen sind den Prüfungsexemplaren als Anhang beigelegt.

Jülich den 29. Juni 2012

(Julian Hirschfeld)



## Abstract

Electrolytes with high ionic conductivity at lower temperatures are the prerequisite for the success of Solid Oxide Fuel Cells (SOFC). One candidate is doped zirconia. In the past, the electrical resistance of zirconia based SOFC electrolytes has mainly been decreased by reducing its thickness. But there are limits to reducing the thickness and one can say that nowadays the normal ways are basically exhausted to further enhance the conductivity of well-known electrolyte materials. Hence, new approaches need to be found to discover windows of enhanced ionic conductivity. This can be achieved by understanding the quantum-mechanical oxygen transport in unconventional configurations of doped zirconia. Therefore, such an understanding is of fundamental importance. In this thesis two approaches are pursued, the investigation of the strain dependent ionic migration in zirconia based electrolytes and the designing of an electrolyte material structure with enhanced and strongly anisotropic ionic conductivity.

The first approach expands the elementary understanding of oxygen migration in oxide lattices. The migration barrier of the oxygen ion jumps in zirconia is determined by applying the Density Functional Theory (DFT) calculations in connection with the Nudged Elastic Band (NEB) method. These computations show an unexpected window of decreased migration barriers at high compressive strains. Similar to other publications a decrease in the migration barrier for expansive strain is observed. But, in addition, a migration barrier decrease under high compressive strains is found beyond a maximal height of the migration barrier. A simple analytic model offers an explanation. The drop of the migration barrier at high compressions originates from the elevation of the ground-state energy. This means: Increasing ground state energies becomes an interesting alternative to facilitate ionic mobility.

The second approach is based on the idea, that actually, only in the direction of ion transport the ionic conductivity in SOFC electrolytes is required to be high. Using a layering of zirconium and yttrium in the fluorite structure and applying DFT and NEB again, a high vacancy concentration and a very low migration barrier in two dimensions is observed, while the mobility in the third direction is sacrificed. The ionic conductivity of this new structure at  $500^{\circ}\text{C}$  surpasses that of the state of the art electrolyte Yttrium Stabilized Zirconia (YSZ) at  $800^{\circ}\text{C}$ .

Throughout the process of searching for augmented ionic conductivity, the NEB method has particularly been used extensively and has been examined in detail. This method has been applied to quite different systems to gain a better understanding of it. While NEB has been applied, it has been found that a certain modification of the NEB, the Minimum search Nudged Elastic Band (MsNEB), is able to find global minima in a complex phase space. Furthermore, the MsNEB turns out to be complementary to simulated annealing and the genetic algorithm. This new scheme has not been applied to electrolyte materials, yet. However, its capabilities have been demonstrated by detecting the most stable isomers of the phosphorus  $P_4$ ,  $P_8$  molecules and the corresponding molecules of  $As_n$ ,  $Sb_n$ ,  $Bi_n$ , ( $n = 4, 8$ ). In the case of  $P_8$ , the new MsNEB has led to a hitherto unknown configuration, being more stable than the previously assumed ground state.



## Zusammenfassung

Elektrolyte mit hoher ionischer Leitfähigkeit bei niedrigen Temperaturen sind die Voraussetzung für den Erfolg von Feststoffelektrolytbrennstoffzellen (SOFC). Ein Kandidat für solch ein Material ist dotiertes Zirkonoxid. In der Vergangenheit wurde der elektrische Widerstand der Elektrolyten hauptsächlich durch Verringerung der Schichtdicken verbessert. Allerdings können diese nicht beliebig dünn werden und man kann sagen, dass die üblichen Methoden die Leitfähigkeit gut bekannter Elektrolyte weiter zu verbessern praktisch ausgeschöpft sind. Daher müssen neue Fenster verbesserter Leitfähigkeit gefunden werden. Dies kann durch das Verstehen des quantenmechanischen Sauerstofftransports in unkonventionellen Zirkonoxidkonfigurationen erreicht werden. Somit ist ein solches Verständnis von essenzieller Bedeutung. In dieser Thesis werden zwei Ansätze verfolgt, die Untersuchung der dehnungsabhängige Migrationsbarriere und die Konstruieren eines Elektrolytmaterials mit verbesserter und stark anisotroper ionischer Leitfähigkeit.

Der erste Ansatz erweitert das elementare Verständnis des Sauerstofftransports in Oxidgittern. Die Migrationsbarrieren des Sauerstofftransports in Zirkonoxid wird durch Anwendung der Dichtefunktionaltheorie (DFT) in Verbindung mit der “Nudged Elastic Band” (NEB) Methode bestimmen. Diese Rechnungen zeigen ein unerwartetes Abnehmen der Barriere unter starker Kompression. Ähnlich zu anderen Veröffentlichungen wurde ein Abfall der Barriere bei Expansion des Gitters beobachtet. Zusätzlich wurde ein erneuter Abfall der Barriere bei starken Kompressionen jenseits eines Barrierenmaximums gefunden. Ein einfaches analytisches Modell zeigt hierfür eine Erklärung auf: Eine Anhebung der Grundzustandsenergien bei hohen Drücken führt zu dem erneuten Abfall der Barriere. Hieraus folgt: Eine Erhöhung der Grundzustandsenergie kann ein interessanter alternativer Ansatz zur Verbesserung ionischer Leitfähigkeit sein.

Der zweite Ansatz folgt der Idee, dass ionische Leitfähigkeit in SOFC Elektrolyten prinzipiell nur in der Richtung des Ionenflusses hoch sein muss. Wird eine Schichtung von Zirkonium und Yttrium im Fluoritgitter verwendet, so erreicht man eine hohe Leerstellenkonzentration und beobachtet eine sehr niedrige Barriere in zwei Dimensionen, während in der dritten Richtung die Mobilität der Ionen geopfert wurde. Die ionische Leitfähigkeit dieser neuen Struktur übertrifft sogar schon bei  $500^{\circ}\text{C}$  die von Yttrium stabilisiertem Zirkonoxid (YSZ) bei  $800^{\circ}\text{C}$ .

In der Suche nach verbesserter Leitfähigkeit, wurde vor allem die NEB Methode ausgiebig verwendet. Um ein besseres Verständnis dieser Methode zu erlangen wurde diese auf viele sehr verschiedene Systeme angewendet. Dabei hat sich herausgestellt, dass eine bestimmte neue Modifikation von NEB, die “Minimum search Nudged Elastic Band” (MsNEB) Methode, in der Lage ist globale Minima in komplexen Phasenräumen zu finden. Weiterhin stellt sich heraus, dass MsNEB komplementär zu “Simulated Annealing” und dem “Genetischen Algorithmus” ist. Diese neue Methode wurde zwar noch nicht auf Elektrolyte angewendet, hat aber ihr Potential bereits dadurch demonstriert, dass sie die stabilsten Konfigurationen von Phosphor  $P_4$ ,  $P_8$  Molekülen sowie von entsprechenden  $As_n$ ,  $Sb_n$ ,  $Bi_n$ , ( $n = 4, 8$ ) Molekülen gefunden hat. Im Fall von  $P_8$  hat MsNEB zu einer bisher unbekanntenen Konfiguration geführt, die stabiler als der bisher angenommene Grundzustand ist.



## 摘要

在较低温度下仍然有着较高的离子导电性的电解质是固体氧化物燃料电池得以成功被应用的前提。一个可选的电解质是掺杂氧化锆。之前，基于掺杂氧化锆固体氧化物燃料电池中的电解质的电阻，是通过减小电解质的厚度的方式来减小的。但是，电解质的厚度只能够有限程度地被减小，而且同时，现今通常用的方法基本可以说是难以再进一步增强众所周知的电解质材料的导电性了。因此，新方法需要被建立，以寻找增强的离子导电性的窗口。这个新的方法可以通过对于掺杂氧化锆在量子力学中的非传统组态下的氧气运输的原理的理解而被找到。因而，此理解是具有根本的重要意义的。本文使用了两种方法：在基于氧化锆的电解质中应变依赖的离子迁移，以及设计一个电解质材料，此材料有着强各向异性的、增强了的离子导电性。

第一个方法拓展了对于氧化物晶体中氧离子迁移的基础理解。通过应用密度泛函理论 (DFT) 的计算结果和Nudged Elastic Band (NEB)算法，氧化锆中的氧离子跳跃的迁移能垒被测定。这些计算显示了一个没有预料到的，在高压缩应变下减小了的迁移障碍的窗口。和其他文献所述相似的是，在膨胀应变下产生的迁移障碍的减小是可以被观测到的。但是，除此之外，在高于最大高度的高压缩应变下，迁移障碍的减小也被发现了。对此，一个简单的解析模型提供了一个解释。在高压缩应变下，迁移障碍的下降来源于基态能量的升高。这意味着：增加的基态能量成为了一个有趣的促成离子迁移的选择。

第二种方法是基于以下构想的：实际上，只有在离子迁移的方向上才需要固体氧化物燃料电池中的电解质有高离子导电性。运用锆和钇萤石型结构的层叠结构，并且通过应用密度泛函理论 (DFT) 和NEB算法，一个很高的空位浓度和一个很低的迁移障碍可以在两个维度中观测到；同时，第三个维度上的导电性被保持在一个低水平上。这个新结构的离子在500摄氏度时导电性要优于在先进的钇稳定氧化锆电解质在800摄氏度时的离子导电性。在寻找的离子导电性增强了的电解质的过程中，NEB算法被非常广泛的使用，并且被在细节上检验。为了更好地理解此算法，它被应用于不同的系统。在它被应用的过程中，做了一定修改的NEB算法，即the Minimum search Nudged Elastic Band (MsNEB)算法，可以在一个复杂的相空间中找到全局的最低点。而且，MsNEB算法是与模拟退火算法、遗传算法互相补充的。这个算法还没有被应用于电解质材料。但是，在检测磷的最稳定异构体 $P_4$ 、 $P_8$ 分子和相应的 $Sb_n$ 、 $Bi_n$ ，( $n = 4, 8$ )分子时，它的潜力得到了证明。在计算 $P_8$ 时，新算法MsNEB导出了一个前所未有的构型。此构型比之前假设的基态还要稳定。



# 1. Introduction

Among fuel cells the high temperature Solid Oxide Fuel Cell (SOFC) is a very promising candidate due to its high power density and its wide variety of possible fuel types (hydrogen,  $CO$ , methane, ammonia etc.). At present one problem of the SOFC is the required high temperature ( $T > 700^\circ\text{C}$ ). The standard electrolyte being used, the Yttrium Stabilized Zirconia  $Y_{2x}Zr_{1-2x}O_{2-x}$  (YSZ), has a negligible ionic conductivity below  $700^\circ\text{C}$  and the progress from the  $800^\circ\text{C}$  SOFC to the  $700^\circ\text{C}$  SOFC was mainly achieved by fabricating extremely thin [1] electrolyte layers. Nowadays electrolyte-thicknesses of  $10\ \mu\text{m}$  and less are possible. To construct a mechanically stable and gas-tight layer of that thickness is, however, a challenging task.

It seems that decreasing the thickness of the electrolyte further will come to its limits in a not too far future. Therefore, it is necessary to look for alternative approaches overcoming the problem of the high operating temperatures in SOFCs. A prerequisite is an understanding of the electrolyte under various conditions. Here, two approaches are investigated and assessed what kind of windows for enhanced ionic transport in solid oxide electrolyte they provide. Namely, the strain dependence of the ionic conductivity and the assumption of anisotropic ionic mobility in a new type of zirconia based electrolyte material are analyzed. It will be showed that both the variation of the lattice strain and the here-investigated anisotropic structure enhances the ionic mobility.

Due to different thermal expansion coefficients of the materials in use, the electrolyte already experiences strain. Engineering the strain in such a way, that it has a positive effect on the ionic conductivity of the electrolyte, will lead to an additional enhancement of the fuel cell efficiency. Previous investigations [2, 3, 4, 5, 6, 7, 8, 9, 10, 11] on the strain dependence already pointed out the increase in conductivity under expansion of the crystal lattice and a decrease under compression. Four groups [2, 3, 4, 10] proposed sandwich-type epitaxially grown structures consisting of YSZ and an additional oxide with a larger lattice constant (e.g.,  $Y_2O_3$ ), one group investigated a single layer YSZ of different thickness on a MgO substrate [9] and two other groups applied pressure directly to the electrolyte material [5, 8]. In 1998 Suzuki et al. [2] investigated the ionic motion of oxygen in YSZ/ $CeO_2$  sandwich structures by molecular dynamics simulations. They found an increase of the diffusion coefficient in YSZ by a factor of 1.7 in comparison to bulk conductivity due to the expansive strain the  $CeO_2$  layers induce in the electrolyte. In 2005 Kosacki et al. [9] showed in their experiment, that the conductivity of an epitaxial layer YSZ on MgO substrate is increased by up to an order of magnitude in comparison to the bulk material, while the activation barrier decreases by a factor of two. Three years later Korte et al. [3] presented an experiment, in which they measured the ionic conductivity in YSZ/ $Y_2O_3$  sandwich structures. For increasing numbers of sandwich repetitions (i.e., increasing number of YSZ layers of decreasing thickness) they found an

enhancement of the ionic conductivity perpendicular to the layers. From a layer thickness of 200 nm down to 24 nm the conductivity increased by a factor of about 1.3 showing a decrease in activation energy of about 0.14 eV. In 2009 they reported experiments with three different YSZ/oxide structures for both compressive and expansive strain showing an exponential dependence of the conductivity on the lattice mismatch [4]. Pennycook et al. [10] investigated the structure and the ionic conductivity in a zirconia slab sandwiched between STO by means of molecular dynamics simulations. They found under an expansive strain of 7% that a new oxygen sub-lattice structure occurs and estimated the conductivity increase to be six orders of magnitude. This work is preceded by an experimental work by Garcia-Barriocanal et al. [12] measuring an eight orders of magnitude higher ionic conductivity than in YSZ. Both these results are, however, highly controversial. It is not clear, whether the experiments measure the ionic conductivity in the YSZ or an electrical one in the STO layers. Furthermore, there are, until now, no other experiments showing a comparable conductivity in such structures. On the theoretical side, this is a very hot topic at the present time, but the work by Pennycook et al. was the only one reporting such high conductivities. Araki et al. [5] presented an experiment in which they directly exposed the electrolyte material to external expansive pressure. They also observed an increase in ionic conductivity but did not find a change in the activation energy, while Sate et al. [8] observed an increase in activation energy under compressive strain in a similar experiment. In 2010 Kushima and Yildiz published an extensive investigation [6] about the strain dependence of the migration barrier in YSZ for five different migration configurations based on Density Functional Theory (DFT) computations. They showed for one migration process without any impurities in the direct vicinity, that the migration barrier decreases with expansive strain even towards a barrier of height zero. However, for the other migration processes they could not find a clear behavior, only a rough decreasing trend in their calculations. A review article [13] from 2010 covers most of these approaches in a more extensive way.

While all these investigations address only expansive strain, or very small compressive strain, this thesis will cover a much larger strain range and reveal unexpected behavior at large compressions. The strain dependence of the ionic migration in zirconia based on DFT calculations is investigated and a conclusive analytic discussion of the phenomenon provided. First the focus lies on one basic migration configuration without any correlation effects<sup>1</sup> over a wide range of strain to understand the physics behind the strain dependence. The performance of the electrolyte will only be assessed from the migration barrier at a given strain. Since the ionic conductivity depends exponentially on the migration barrier ( $\propto \exp(-\Delta E/k_B T)$ ), it is a crucial material quantity. Other material parameters, like the Vineyard coefficient [14] describing the local vibrational properties of the lattice or the jump distance, affect the conductivity only linearly and will have a minor influence. An exponential dependence of the ionic conductivity with respect to external strain has been reported [3, 4, 6, 8, 9, 10] supporting this kind of procedure. By using the DFT method in combination with the Nudged Elastic Band (NEB) method

---

<sup>1</sup>This refers to two types of correlations: the vacancy-vacancy correlations and the vacancy-dopant correlations

[15, 16, 17], the strain dependence of the migration barrier is determined. For expansion and low compressions the barrier will show the well-known behavior, which is a decrease with an expansion of the lattice. When applying larger compressions, the system exhibits a maximum in migration barrier with a following decrease down to a barrier of the height zero. This drop could be accounted to the elevation of the initial and final configurations of the jump, effectively reducing the barrier until the “barrier position” becomes the ground state of the system. Utilizing such a behavior could lead to new ways for enhancing ionic migration in electrolytes. This analysis will be complemented by investigations of doped zirconia.

However, the scope of the thesis goes further than gaining fundamental understanding. As mentioned before a new structure with augmented conductivity for low temperature SOFC applications will be proposed. This presents the possibility to obtain higher ionic motion in electrolytes by systematically disregarding the ionic mobility in one or two directions of the electrolyte to enhance motion into the third direction. This newly proposed structure is an impressive example for this new type of electrolyte materials with superior ionic conductivity in one plane. The improvement in conductivity arises not only from the strain effect as in typical sandwiched structures (e.g. [2, 3, 4, 10]), but also from a number of other effects leading to further enhancement. Ab-initio molecular dynamics calculations will show that the conductivity of the new structure at  $500^{\circ}\text{C}$  outperforms the state of the art electrolyte YSZ at  $800^{\circ}\text{C}$ .

While applying the NEB method vastly to determine the migration barriers in the electrolyte materials, the NEB method itself was examined in further detail to gain fundamental understanding of its functional principle. In this process, it was discovered that a specific modification of the NEB was able to find global minima in the complex phase space of a given system. This modification will be called the Minimum search Nudged Elastic Band (MsNEB) method. On the one hand is this a considerable extension of the understanding of the NEB method, on the other hand is the purpose of the modification itself very intriguing. Because of the band character of the MsNEB, the probability to escape a local minimum depends on the width of a minimum in phase space. This contrasts to many typically used optimization schemes, as many of them rest on simulated annealing [18] and the genetic algorithm [19]. Both of these methods are energy based, which means that the probability to escape a local minimum in these schemes depends on the depth of the minimum. Under this consideration, the new MsNEB is complementary to the energy based global optimization schemes and will find different types of minima. In fact, it turned out that the MsNEB method was able to find an unknown most stable isomer in the test system  $P_8$ .

This thesis is structured in the following way: First, an introduction to fuel cells is given in which the fundamentals of SOFC thermodynamics are discussed, as well as the factors determining the efficiency. Furthermore, a short comparison of the different types of fuel cells is given. In the chapters 3 and 4 the theoretical background of the tools used in this thesis is presented. First, the Density Functional Theory is introduced starting from the many-body wave function. Since, except for the hydrogen atom, not even a single atom can be approached computationally using the exact quantum-mechanical description, an auxiliary system of non-interacting particles is used

to determine the electronic ground state of the atomic system. This is the Kohn-Sham formalism described and used in the DFT making it possible to describe complicated quantum-mechanical systems with non-negligible exchanges and correlations of the electrons convincingly accurate. This method revolutionized the computational solid-state and molecular sciences. This is also the framework used to accurately compute the relevant quantities in the materials of interest in this thesis. Furthermore, it is described how the plane-wave basis embeds into the DFT in the way it is used in the Vienna Ab Initio Package (VASP), which is the program of choice for all DFT computations presented in this work.

In the following chapter (Chap. 4) the Transition State Theory (TST) is introduced. Since the motion of ions in condensed matter describes a rare-event diffusion, it can be treated with equilibrium-statistics. This theory shows that it is possible to obtain the diffusivity and ionic conductivity of a migration process as long as the corresponding migration barrier is known, and some minor assumptions are done. These migration barriers are determined in the framework of the DFT using the NEB method. This scheme, being described in the last part of this chapter, considers a band of interacting system images. By using artificial spring forces between these images and following the real potential in all but the direction of the band, it is possible to find the Minimum Energy Pathway (MEP) between two points. The migration barrier is simply the maximum of this MEP. The amazing feature of this method is, that it changes the search for a saddle point (the migration barrier is a maximum along the MEP and a minimum in all other directions) to a minimum search, for which many highly efficient algorithms exist.

The newly developed optimization method MsNEB is described in chapter 5. After introducing the scheme itself, it will be applied to the test cases of phosphorus  $P_4$ ,  $P_8$  and the corresponding molecules of arsenic, antimony and bismuth to show the power of the method.

In the following chapter, the focus lies on the electrolyte materials of SOFCs. First, an introduction to the various types of SOFC electrolytes and their individual advantages and disadvantages is given. Then, the material of choice in the thesis, the zirconia based electrolytes, are discussed in more detail. Especially the effect of charged vacancies in zirconia will be investigated based on DFT calculations. It will become obvious that the vacancies in YSZ are positively charged, and that it has a serious effect on the migration properties in pure zirconia, if neutral vacancies are assumed.

In chapter 7 the analysis of the strain dependent ionic migration in zirconia based on DFT calculations is presented together with an analytic model employing interactions of the Lennard-Jones type to understand the previously mentioned unexpected behavior at high compressions. The investigation of the strain dependence is then deepened by studying the effects, which the strain has on the dopants yttrium and scandium in zirconia.

In the last content-chapter of this thesis, the knowledge obtained in chapters 6 and 7 is harnessed with information from literature to invent a new zirconium-yttrium-oxide based electrolyte material having superior ionic conductivity in two spatial dimensions and a very low one in the third dimension. A structure having alternating layers of zirco-

niium and yttrium in the fluorite structure exhibits high charge carrier concentrations of 12.5% and strongly reduced migration barriers in two dimensions. The performance even surpasses the one of LSGM and CGO, making applications of this material in SOFCs at temperatures below  $500^{\circ}\text{C}$  possible. The price paid for gaining this improved performance is a complex synthesizing procedure. This is, however, a price to be paid if the material shows a comparable performance in experiment.

A summery of the results will finalize the thesis.



## 2. Fuel cell functionality

The purpose of this chapter is to provide an overview over the principles of fuel cells and to enhance the understanding of how the goals investigated in this thesis embed into the overall fuel cell problems<sup>1</sup>.

### 2.1. Operating principle

A fuel cell is a galvanic element, which converts chemical energy of constantly added fuel into electrical energy. A galvanic element consists of an electrolyte, a cathode, an anode and a casing. To produce an external electrical current between the electrodes, the anode needs to be engulfed by fuel and the cathode by an oxidizing agent. In fuel cells different kinds of fuels, like natural gas, methanol or hydrogen, can be used (depending on the electrolyte). On the cathode side there is only the choice between pure and atmospheric oxygen. The reaction is more efficient if pure oxygen is used, nevertheless air has the advantage of being cheap and omnipresent in terrestrial applications. The most efficient reaction occurs if hydrogen is used as fuel and pure oxygen as the oxidizing agent. It is in addition the simplest reaction from a chemical point of view. A mixture of oxygen and hydrogen is called detonation gas, which reacts highly exothermic. In an exothermic reaction chemical energy is released. Though by burning the detonation gas the chemical energy is completely converted into heat. In the direct reaction



a total reaction enthalpy<sup>2</sup> of about  $\Delta H^{(H_2O)l} = -286 \text{ KJ} \cdot \text{mol}^{-1}$  is released<sup>3</sup>, if water is produced in liquid form. However, in a fuel cell the direct reaction is prevented by keeping fuel and oxidizing agent separated. The total reaction is divided into the fuel oxidation at the anode and the oxygen reduction at the cathode.

---

<sup>1</sup>Since this chapter only aims at promoting the readers understanding, it performs the same function as in my diploma thesis [20] and is therefore given here again, in a strongly to the SOFC adapted way.

<sup>2</sup>The reaction enthalpy  $\Delta H$  is the change of heat. The inner energy  $U$  of a substance is primarily given by the binding energy of its atoms. The change of inner energy  $\Delta U$  in a reaction causes a pressure-volume work  $p\Delta V$  and a change of heat. Thus,  $\Delta H$  is given by the change of inner energy minus the pressure-volume work:  $\Delta H = \Delta U + p\Delta V$  (in an exothermic reaction  $\Delta U$  and  $\Delta H$  is negative).

<sup>3</sup>If chemical energy is released in a reaction, it is called an exothermic reaction and the change of reaction enthalpy is negative. If energy needs to be added to the reactants to keep the reaction running, it is called an endothermic reaction and the change in reaction enthalpy is positive.

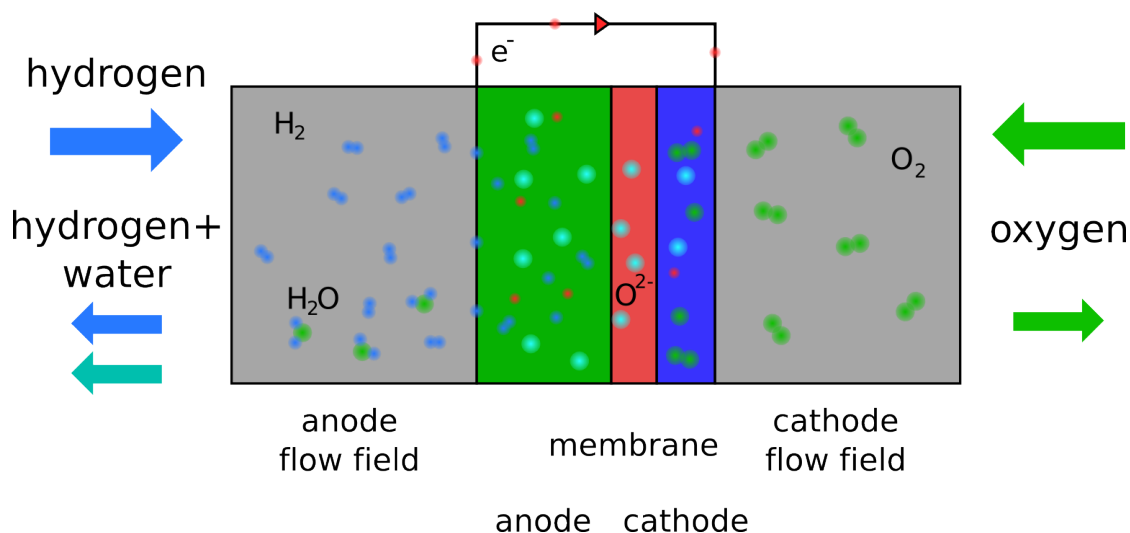
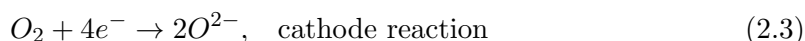


**Figure 2.1.:** Schematic view of a solid oxide fuel cell. The hydrogen is blown through the anode flowfield. On the surface of the catalyst inside of the porous anode, the hydrogen molecules react releasing four electrons with the oxygen ions from the electrode to water. On the cathode side the oxygen molecule dissociates and takes up the four electrons, which were led through some external load from the anode side. The  $O^{2-}$  ions permeate across the electronic isolating and gas blocking membrane following a concentration gradient.

In a SOFC the two partial reactions are:



Following the Hess's law<sup>4</sup>, the change in the reaction enthalpy in the fuel cell is equal to the one in the direct reaction. Since the direct detonation gas reaction needs thermal energy (the activation energy of an exothermic reaction) in form of a flame or a spark to start, the divided reaction in the fuel cell does not start under normal conditions as well. In low temperature fuel cells there is nearly no thermal energy added, but rather the activation energy of the reactions at the electrodes is lowered by a catalyst. Often the catalyst consists of platinum, because of its high catalytic activity and the high stability in oxidizing and in reducing environment. Since the thermal energy in a high temperature fuel cell is much higher, the catalyst can be less noble like nickel. The thermodynamic aspects of the fuel cell reactions are discussed in the following section in more detail.

As any galvanic element, a fuel cell consists of an electrolyte, a cathode and an anode. Additionally, there are flowfields on the surface of the electrodes to distribute the fuel

<sup>4</sup>The Hess's law has been formulated in 1840 by Germain Hess: *The change of reaction enthalpy is constant, no matter if it runs directly or via many sub-reactions.*[21]

over the anode surface, and the oxygen respectively over the cathode surface. Since the gases have to reach the electrolyte, the electrodes are porous. In fact the reactions listed in Eq. (2.2) and Eq. (2.3) take place only at Three Phase Boundaries (TPB), where gas phase, electric conducting catalyst and the ion conducting electrolyte are in contact. The reason is obvious: the oxygen molecules from the gas phase dissociate on the catalyst surface and then ionize taking up electrons from the electric conducting phase. The oxygen could also ionize at an arbitrary location on the catalyst surface, but since the ions cannot migrate to the cathode without contact to an ion conductor, they will eventually recombine. As the ions migrate through the membrane, and the electrons cannot, it is possible to bypass the electron current via a load. Further details of the fuel cell structure are shown in Fig. (2.1).

## 2.2. Thermodynamic aspects

**The second law of thermodynamics:** *The entropy in a closed adiabatic system tends to increase. Only in a reversible process the change of entropy is zero.*

$$\Delta S \geq 0 \quad (2.4)$$

Due to the second law of thermodynamics Eq. (2.4) only a part of the reaction enthalpy can be transferred into electrical energy. The convertible energy is called Gibbs free energy and is given by:

$$\Delta G = \Delta H - T\Delta S. \quad (2.5)$$

Here  $T$  denotes the absolute temperature of the system and  $T\Delta S$  the heat produced in the reaction due to the change of entropy. Hence, the generated electrical energy  $W_{\text{el}}$  is given by  $\Delta G$ , if no other losses occur<sup>5</sup>:

$$W_{\text{el}} = \Delta G. \quad (2.6)$$

The molar electric energy is given by the transferred charge  $-n \cdot F$  times the voltage  $U^0$ , where  $F = N_A \cdot e$  is the Faraday constant and  $N_A$  is the Avogadro number.  $F$  is the total charge of one mol electrons, and  $n$  is the number of transferred electrons in the reaction (c.f. Eq. (2.2) and Eq. (2.3)). In a galvanic element the Open Circuit Voltage (OCV)  $U^0$  is the voltage between the electrodes if no current is drawn from the device. Historically the open circuit voltage is also called *electromotive force*. But since  $U^0$  has the dimension of a voltage and not that of a force, this name is misleading and  $U^0$  is referred to as OCV. Thus, the Gibbs free energy of the reaction can be written as:

$$\Delta G = -n \cdot F \cdot U^0 \quad (2.7)$$

---

<sup>5</sup>Obviously, this is not the case. Due to other effects (e.g. Ohm losses) further energy is converted into heat. For further details see section 2.4.

Respectively the OCV as:

$$U^0 = -\frac{\Delta G}{n \cdot F}. \quad (2.8)$$

Under normal conditions<sup>6</sup> the Gibbs free energy for the creation of one mol of water molecules from one mol hydrogen molecules and half a mol of oxygen molecules is  $\Delta G^0 = -237 \text{ KJ} \cdot \text{mol}^{-1}$ , if water is produced in liquid form and  $\Delta G^0 = -228 \text{ KJ} \cdot \text{mol}^{-1}$ , if water is produced in gaseous form. Therefore the OCV under normal conditions (under which water would be produced in liquid form) is

$$U_0^0 = \frac{237 \text{ KJ} \cdot \text{mol}^{-1}}{2 \cdot 96485 \text{ C} \cdot \text{mol}^{-1}} = 1.23 \text{ V}. \quad (2.9)$$

In SOFCs the operating temperatures are much higher, therefore the OCV cannot be calculated in this way. To obtain the OCV for arbitrary temperatures, the temperature dependency of  $U^0$  has to be investigated:

$$\begin{aligned} \left( \frac{\partial U^0(T)}{\partial T} \right)_p &= -\frac{1}{n \cdot F} \cdot \frac{\partial}{\partial T} (\Delta H - T \Delta S) \\ &= \frac{\Delta S}{n \cdot F}. \end{aligned} \quad (2.10)$$

If the reaction entropy is constant over a temperature interval  $\Delta T$ , the temperature dependent OCV can be obtained by integration:

$$U^0(T) = \int_{T_0}^T \left( \frac{\partial U^0(T')}{\partial T'} \right)_p dT' = \frac{\Delta S}{n \cdot F} (T - T_0) + U_0^0, \quad (2.11)$$

which corresponds to calculating  $\Delta G$  at arbitrary temperatures by

$$\Delta G(T) = \sum_i^{\text{products}} G_{i0} + \Delta S_i(T - T_0) - \sum_i^{\text{reactants}} G_{i0} + \Delta S_i(T - T_0) \quad (2.12)$$

Compound	$G_0$ kJ/mol	$\Delta S$ J/K·mol
$H_2$	0	-130.57
$O_2$	0	-205.02
$H_2O _l$	-237.18	-69.91
$H_2O _g$	-228.6	-188.72

**Table 2.1.:** Formation energies  $G_0$  and entropies of the compounds relevant in a hydrogen fed fuel cell[22]

and insert into Eq. 2.8. The  $G_0$  are the formation energies of the reactant and product species at normal conditions, while  $\Delta S$  are the changes of entropy with increasing temperature of these species. For many compounds values for both  $G_0$  (also called chemical potential  $\mu$ ) and  $\Delta S$  are listed in tables (e.g. on the webpage of the Eduard-Job Foundation [22]). The here relevant values are given in Tab. 2.1. With these values the temperature depen-

<sup>6</sup>pressure  $p^0 = 1013 \text{ hPa}$ , temperature  $T^0 = 25^\circ \text{C}$

dent Gibbs free energy becomes

$$\Delta G(T) = -228.6 \text{ kJ}\cdot\text{mol}^{-1} + 44.36 \text{ J}(\text{mol}\cdot\text{K})^{-1}(T - T_0) \quad (2.13)$$

and the OCV becomes

$$U^0(T) = -\frac{\Delta G(T)}{n \cdot F} = 1.185 \text{ V} - 2.3 \cdot 10^{-4} \text{ V}\cdot\text{K}^{-1}(T - T_0) \quad (2.14)$$

leading to a SOFC OCV at an operation temperature of  $T = 1000 \text{ K}$  of  $U^0(T = 1000 \text{ K}) = 1.02 \text{ V}$ . This voltage is valid for perfect reactant conditions at the electrodes (partial pressures of all species is unity). For arbitrary conditions and under the assumption of ideal gases, the total electrode potentials  $\Phi$  can be calculated by the Nernst equation[23]

$$\Phi(T) = \Phi^0(T) + \frac{R \cdot T}{n \cdot F} \cdot \ln \left( \frac{\prod_i a_{i|\text{ox}}^{\nu_i}}{\prod_j a_{j|\text{red}}^{\nu_j}} \right) \quad (2.15)$$

where  $R$  denotes the gas constant,  $a_{i|\text{ox}}$  the chemical activity<sup>7</sup> of the oxidizing species,  $a_{j|\text{red}}$  the chemical activity of the reducing species and  $\nu_{i,j}$  the corresponding stoichiometric coefficient. In the case of the hydrogen fed SOFC the electrode potentials can be calculated by:

$$\Phi_{\text{anode}}(T) = \Phi_{\text{anode}}^0(T) + \frac{R \cdot T}{2 \cdot F} \cdot \ln \left( \frac{a_{H_2O}}{a_{H_2} \cdot a_{O_2^-}} \right) \quad (2.16)$$

$$\Phi_{\text{cathode}}(T) = \Phi_{\text{cathode}}^0(T) + \frac{R \cdot T}{2 \cdot F} \cdot \ln \left( \frac{\sqrt{a_{O_2}}}{a_{O_2^-}} \right) \quad (2.17)$$

Since the gases are ideal, the activities  $a_i$  at ambient pressure are equal to their partial pressures  $p_i$ . The OCV can be determined now by the difference of the two electrode voltages

$$U(T) = \Phi_{\text{cathode}}(T) - \Phi_{\text{anode}}(T). \quad (2.18)$$

With  $U^0(T) = \Phi_{\text{cathode}}^0(T) - \Phi_{\text{anode}}^0(T)$  the OCV of the fuel cell at arbitrary conditions can be determined by

$$U(T) = U^0(T) + \frac{R \cdot T}{2 \cdot F} \cdot \left( \frac{p_{H_2} \cdot \sqrt{p_{O_2}}}{p_{H_2O}} \right). \quad (2.19)$$

Since water steam is produced, the atmosphere on the anode side is a mixture of hydrogen and water steam, whose partial pressures depend on the hydrogen-gas flow-rate. If the  $H_2$  flow is set to keep hydrogen and water at balance ( $p_{H_2} = p_{H_2O} = 0.5$ ) and the

---

<sup>7</sup>By the activity coefficient  $f$  ( $0 \leq f \leq 1$ ) corrected mole fraction  $c$  to describe the deviation from the law of mass action. For higher mole fractions the activity coefficient deviates stronger from unity.

cathode side is air fed, the OCV of the SOFC at  $T = 1000\text{ K}$  is

$$U(T = 1000\text{ K}) = 1.02\text{ V} + \frac{8.314\text{ J} \cdot \text{mol}^{-1} \cdot \text{K}^{-1} \cdot 1000\text{ K}}{2 \cdot 96485\text{ C} \cdot \text{mol}^{-1}} \cdot \ln(\sqrt{0.21}) = 0.986\text{ V}. \quad (2.20)$$

This is lower than the OCV of a low temperature fuel cell being  $U(T = 273\text{ K}) = 1.219\text{ V}$ , since higher temperatures lead to a strong entropic reduction of the voltage. However, under load other effects reduce the voltage of a low temperature fuel cell stronger than of a SOFC.

### 2.3. Fuel cell polarization

Even though it is possible to calculate the theoretical open circuit voltage by Eq. (2.15), it can not be measured in a real fuel cell. Gas permeation across the membrane can occur by which the direct reaction takes place at the cathode. On the one hand the chemical energy stored in the permeated fuel is converted into heat and is thus lost. On the other hand the permeation leads to mixed potentials. Since there is a finite partial pressure of fuel at the cathode, the partial pressure of the oxidizing agent is reduced, and by that the OCV (c.f. Eq. (2.15)). As the permeation is independent of the current drawn from the fuel cell, it leads to a constant offset in the polarization curve  $U(j)$ .

Under load there are various effects decreasing the cell voltage. These effects are typically quantized as overpotentials<sup>8</sup>  $\eta$ , which is the deviation of the actual cell voltage  $U$  from the theoretical open circuit voltage:

$$\eta = U - U^0. \quad (2.21)$$

The most important overpotentials are:

- Activation overpotential  $\eta_A$
- Ohmic overpotential  $\eta_\Omega$
- Concentration overpotential  $\eta_C$

Ohmic losses occur in all fuel cell parts, the other two effects only at the electrodes. Thus they can be separately observed at the anode and at the cathode. The activation overpotential combined with the Ohmic losses across the electrolyte is shown in Fig. (2.2).

#### 2.3.1. Activation overpotential

Even if no current is drawn from the fuel cell, the reactants dissolve and ionize. Thus surface charges form at the electrode/electrolyte interface. The positive ions concentrate in the electrolyte and the electrons in the electrode. An electric field analogous to the one of a plate capacitor forms at the interfaces. This electric double layer is a further

<sup>8</sup>The overpotential is also called overvoltage or polarization.

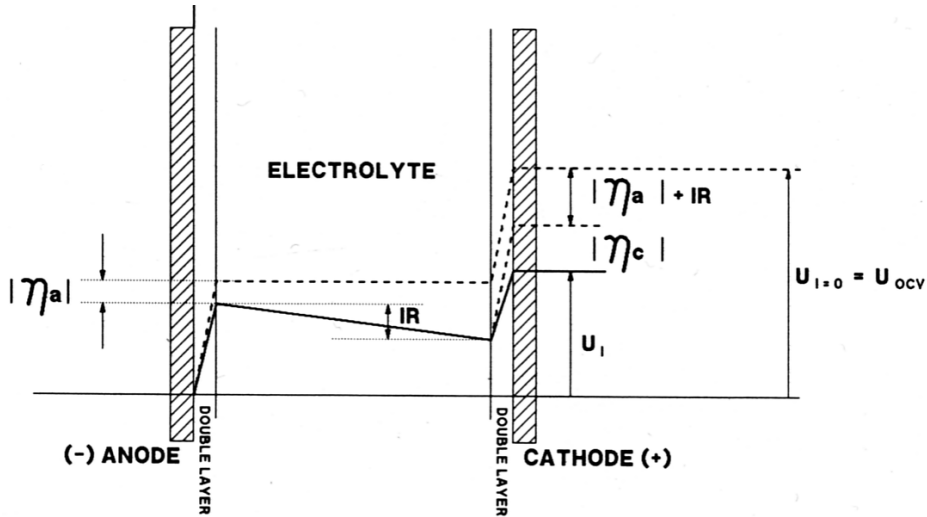


**Figure 2.2.:** The activation overpotential  $\eta_A$  is divided into anodic activation losses  $\eta_a$  and cathodic activation losses  $\eta_c$ . The Ohmic losses are identified by  $\eta_\Omega = IR$ . The dashed line indicates the voltage without any current drawn from the fuel cell. The continuous line indicates the situation under load.[24]

barrier for the ionized species to overcome. So the total potential barrier is given by the intrinsic activation energy of a reaction step plus the double layer potential. Even though the barrier has to be overcome in each reaction step including a material transition, the activation overpotential is given only by the **Rate Determining Step** (RDS)<sup>9</sup>. The current density limited by the activation overpotential is given by the Butler-Volmer Equation[23]:

$$j = j_0 \left[ \exp\left(\frac{\alpha \cdot \eta_A \cdot n \cdot F}{R \cdot T}\right) - \exp\left(-\frac{(1 - \alpha) \cdot \eta_A \cdot n \cdot F}{R \cdot T}\right) \right]. \quad (2.22)$$

Besides the known quantities, there is the transfer coefficient  $\alpha$  and the exchange current density  $j_0$  in the Butler-Volmer equation. The transfer coefficient  $\alpha$  denotes the fraction of the change in activation overpotential, which leads to a change in the reaction rate. For fuel cells this is typically  $\alpha = 0.5$ . If no current is drawn from the fuel cell, both exponential functions are equal, since the first one represents the anodic partial current density and the second one the cathodic partial current density. The exchange current density  $j_0$  is a function of the effective catalyst surface<sup>10</sup>  $a$ , the molar fractions of the

<sup>9</sup>A reaction can be divided into individual steps, like fuel adsorption on the catalyst or the ionization. Since the reaction rate of the overall reaction is determined by each step, there is always one step with the slowest kinetic. This, figuratively spoken, weakest link of the reaction chain is the rate determining step.

<sup>10</sup>The effective catalyst surface is the ratio of the active catalyst surface to the geometrical one.

catalyst	$j_0^0 \left[ \frac{\text{mA}}{\text{cm}^2} \right]$
lead	$2.5 \cdot 10^{-13}$
tin	$3.0 \cdot 10^{-11}$
silver	$4.0 \cdot 10^{-7}$
nickel	$6.0 \cdot 10^{-6}$
platinum	$5.0 \cdot 10^{-4}$
palladium	$4.0 \cdot 10^{-3}$

**Table 2.2.:** Typical reference exchange current densities at normal conditions for various metals.[25]

the Butler-Volmer equation simplifies to:

$$j = -j_0 \cdot \exp\left(-\frac{\alpha \cdot n \cdot F}{R \cdot T} \eta_{A,c}\right). \quad (2.24)$$

Thus the cathodic activation overpotential is given by:

$$\eta_{A,c} = -\frac{R \cdot T}{\alpha \cdot n \cdot F} \cdot \ln\left(\frac{|j|}{|j_0|}\right), \quad \text{with } j < 0, \quad (2.25)$$

which is equal to the empirical Tafel equation

$$|\eta_{A,c}| = b \cdot \ln\left(\frac{|j|}{|j_0|}\right) \quad (2.26)$$

with the Tafel slope  $b$ .

### 2.3.2. Ohmic overpotential

All electron conductors have finite electronic conductivity and all ion conductors have finite ionic conductivity. Since there are both kinds of conductors present in a fuel cell, Ohmic losses can be found in all parts of the fuel cells. Ionic resistances  $\rho_{\text{ion}}$  emerge in the electrolyte and in the electrode. Electronic resistances  $\rho_e$  can be found in the electrode and flowfield plates. Furthermore, there are contact resistances between different parts of the fuel cell. As these surface effects can be allocated to either electronic or ionic resistances, they are included in either  $\rho_e$  or  $\rho_{\text{ion}}$ . Altogether these resistances lead to the Ohmic overpotential

$$\eta_{\Omega} = j(\rho_{\text{ion}} + \rho_e) \quad (2.27)$$

with the specific resistances  $\rho_{\text{ion}}$  and  $\rho_e$ . Obviously the ionic resistivity is much higher than the electronic one and will dominate Eq. 2.27. The improvement of the ionic conductivity of the electrolyte material will have the highest benefit for this overpotential. Therefore, large parts of this thesis are dedicated to understand and improve the ionic conductivity in the electrolyte materials of the SOFC.

reactants at the electrode  $x$  and a reference exchange current density  $j_0^0$ :

$$j_0 = j_0^0 \cdot x \cdot a. \quad (2.23)$$

The reference exchange current density depends strongly on the catalyst material. Typical values are given in Tab. (2.2). For a hydrogen/oxygen fuel cell, the hydrogen oxidation is much faster than the oxygen reduction. Thus the oxygen reduction is the rate determining step. Under disregard of the anodic activation polarization

### 2.3.3. Concentration overpotential

As soon as current is drawn from the fuel cell, the reactants at the electrodes are consumed in the reactions. Therefore, the concentration of fuel in the direct vicinity of the anode and the concentration of oxygen respectively in the direct vicinity of the cathode drops immediately. The reactants diffuse from the flowfield to the TPB, where the reactions take place. At high current densities the fuel and the oxygen is consumed rapidly. Since the diffusion rates in the electrodes are finite, the reactants may not be transported fast enough across the electrode to compensate the consumption. Based on the Butler-Volmer equation, the concentration overpotential can be written as:

$$\eta_C = \frac{2 \cdot R \cdot T}{n \cdot F} \cdot \left[ \ln \left( \frac{c_{\text{red}}}{c_{\text{red}}^0} \right) - \ln \left( \frac{c_{\text{ox}}}{c_{\text{ox}}^0} \right) \right], \quad \text{with } \alpha = \frac{1}{2}. \quad (2.28)$$

Here,  $c_{\text{ox}}$  is the concentration of the oxidizing species at the cathode surface, and  $c_{\text{ox}}^0$  is the concentration of the oxidizing species in the current free case. The same holds for the concentrations of the reducing species  $c_{\text{red}}$  and  $c_{\text{red}}^0$  at the anode surface. The more current is drawn from the fuel cell, the lower the reactant concentration at the electrode surfaces. One can deduce, that there is a limiting current density, at which the concentration of one reactant at the respective electrode surface is zero. Due to the logarithmic dependency,  $\eta_C$  increases rapidly for low concentrations. In virtue of the larger molecule size of oxygen in comparison to hydrogen, the hydrogen diffusion is higher than the one of oxygen. On the other hand reduces the produced water steam at the anode surface the local concentration of hydrogen.

### 2.3.4. The fuel cell polarization curve

These three effects together lead to the typical fuel cell polarization curve. A schematic view of the curve is given in Fig. (2.3). It can be unambiguously divided into three domains. In the low current density domain the activation overpotential leads to a dip. As mentioned before, the activation overpotential is mostly given by the catalyst. Thus, if the catalytic active area is increased, or if palladium is used as the catalyst, the voltage loss in the low current density domain will be reduced. Since these voltage losses affect the cell voltage even at higher current densities, the improvement of the catalyst leads to a higher cell voltage at all current densities. As can be seen from Eq. 2.22, also higher temperatures reduce this effect, since it is a energy barrier for ions to overcome which is a thermally activated process. Due to this temperature dependence, the activation overpotential has an inferior impact on the performance of SOFC, while it diminishes the performance of a low temperature fuel cell strongly.

The polarization curve in the intermediate current density domain has a constant slope, as it is governed by Ohmic losses. To attenuate the voltage losses in the intermediate domain, the resistances of fuel cell components have to be reduced. This is often approached by diminishing the electrolyte thickness, but other approaches try to increase the conductivity of the electrolyte material.

At high current densities, the reactant diffusion to the electrodes becomes the RDS.

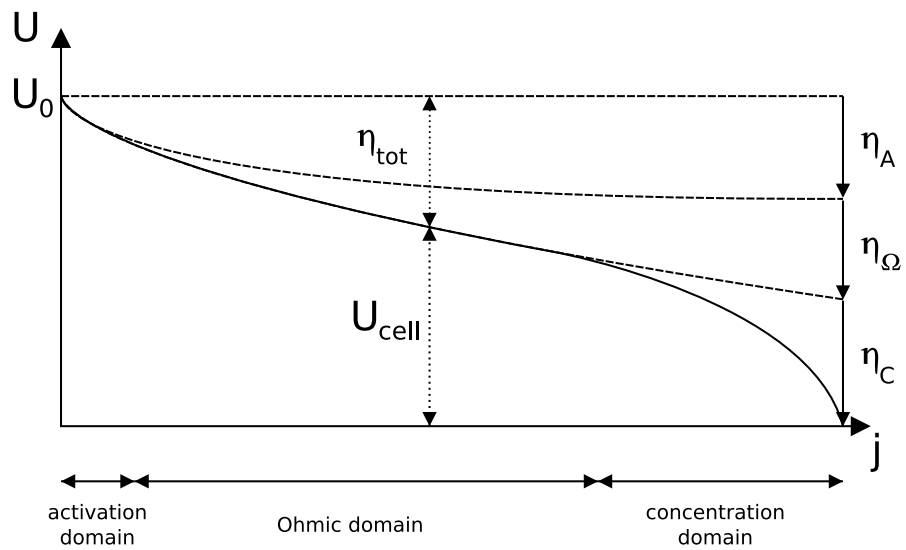


**Figure 2.3.:** A typical polarization curve is governed by the activation overpotential  $\eta_A$  in the low current density domain, by the Ohmic overpotential  $\eta_\Omega$  in the intermediate domain, and by the concentration overpotential  $\eta_C$  in the high current density domain. The relation of the losses due to the total overpotential  $\eta_{tot}$  to the remaining cell voltage  $U_{cell}$  is shown at a possible operating point.

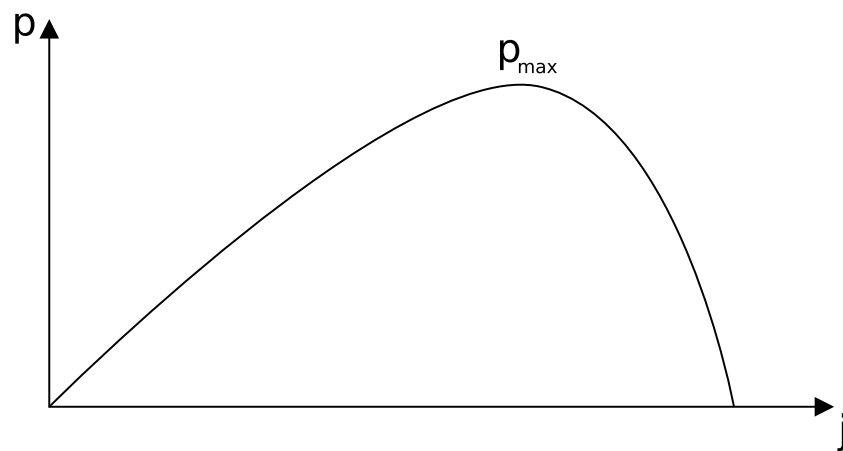


**Figure 2.4.:** Associated with the polarization curve demonstrated in Fig. (2.3) is a power density curve  $p(j)$ . Since the electric power density is given by  $p = j \cdot U$  and the cell voltage drops at high current densities, the fuel cells power density has a maximum  $p_{max}$ . It should be mentioned, that the maximal power density might not be the optimal operating point, since the cell voltage and by that the fuel cell efficiency (c.f. section 2.4 paragraph “Voltage efficiency”) could already be too low at this current density.

This effect cannot be lowered or even wiped out. However, it is possible to shift the limiting current density to higher values by improving the electrode porosity.

Usually, it is meaningful to estimate the fuel cell performance on basis of its maximal electrical power. Therefore, power density curves (c.f. Fig. (2.4)) are interesting evaluation tools.

## 2.4. Fuel cell efficiency

The greatest advantage of fuel cells in comparison to classical combustion engines is the maximal efficiency, since it is not limited by the Carnot efficiency

$$\eta_{\text{carnot}} = 1 - \frac{T_{\text{low}}}{T_{\text{high}}}. \quad (2.29)$$

Thus, it is possible to convert a much larger fraction of the chemical energy stored in the fuel into electrical energy than e.g. in a gas power plant. If fuel cells are used as electrical energy sources for electrotraction, they have to compete with the efficiency of diesel engines, which is less than 45% [26]. But even though the fuel cell efficiency is not bound to the Carnot efficiency, it is still far below 100%.

The overall fuel cell efficiency is limited by the following effects:

- thermodynamics
- internal voltage losses
- fuel permeation across the membrane

**Thermodynamic efficiency** The theoretical maximal efficiency of the fuel cell is given by thermodynamics. Due to the second law of thermodynamics (c.f. Eq. (2.4)) the entropy tends to increase. Thus a fraction of the reaction enthalpy  $\Delta H$  is always converted into heat. This fraction is given by the change of entropy and the absolute temperature  $T\Delta S$ . Therefore, the thermodynamic efficiency is given by:

$$\epsilon_{\text{th}} = \frac{\Delta G}{\Delta H} = 1 - \frac{T\Delta S}{\Delta H}. \quad (2.30)$$

The change of reaction enthalpy in Eq. (2.1) is  $\Delta H = -286 \text{ KJ} \cdot \text{mol}^{-1}$ . Under normal conditions with liquid water as the product, the Gibbs free energy is  $\Delta G = -237 \text{ KJ} \cdot \text{mol}^{-1}$ , in the SOFC at  $T = 1000 \text{ K}$   $\Delta G = -196.4 \text{ KJ} \cdot \text{mol}^{-1}$ . Thus the thermodynamic efficiency of the SOFC is:

$$\epsilon_{\text{th}} = \frac{196.4 \text{ KJ} \cdot \text{mol}^{-1}}{286 \text{ KJ} \cdot \text{mol}^{-1}} = 0.687. \quad (2.31)$$

This value strongly depends on the chemical reaction. For example the entropy change of the  $C + 1/2O_2 \rightarrow CO$  reaction is positive, which can also occur in high temperature

fuel cells. Therefore, the thermodynamic efficiency of this reaction is larger than one. Though all reactions being interesting for fuel cell applications come along with negative entropy changes.

**Voltage efficiency** In virtue of Ohmic losses a resistor in an electrical circuit heats up. The dissipated power is given by  $P = RI^2$ , with the resistance  $R$  of the resistor. This takes place in both, the electric and the ionic conducting materials of fuel cells. A further fraction of the cell voltage is used to run the chemical reaction, which is given by the activation loss. The voltage efficiency combines all losses due to electrode kinetics and Ohmic losses. It is defined by the measurable open circuit voltage  $U_0$  and the cell voltage  $U(j)$  at a certain current density  $j$ :

$$\epsilon_V = \frac{U(j)}{U_0}. \quad (2.32)$$

Increasing the current density will increase the power output of the fuel cell but will reduce the voltage (c.f. Figs. 2.3 and 2.4) and by that the efficiency of the cell. Therefore a trade-off between efficiency and power output has to be done leading to a typical voltage efficiency of about:

$$\epsilon_V \approx 0.7. \quad (2.33)$$

**Current efficiency** The current efficiency is a combination of the Faradaic efficiency  $\epsilon_F$  and the fuel utilization  $N$ . As it is hardly possible to distribute the fuel homogeneously throughout the electrode, more fuel is blown across the flowfield channels than necessary to run the reaction. The fraction of the fuel injected into the flowfield to the consumed fuel denotes the utilization. This modifiable factor is typically set to 0.85 [27]. The Faradaic efficiency includes fuel losses due to permeation or leakage. It is defined as the fraction of the cell current  $I$  to the theoretical current depending on the reaction speed<sup>11</sup>  $v$ .

$$\epsilon_F = \frac{I}{I_{theo}} = \frac{I}{F \cdot n \cdot v} \quad (2.34)$$

Thus the current efficiency is given by:

$$\epsilon_C = \epsilon_F \cdot N = \frac{I \cdot N}{F \cdot n \cdot v} \quad (2.35)$$

If pure hydrogen and pure oxygen is used and neither fuel permeation nor fuel leakage occurs, the Faradaic efficiency is one. In this case the current efficiency is equal to the fuel utilization:

$$\epsilon_C \approx 0.85 \quad (2.36)$$

---

<sup>11</sup>The reaction speed is defined as the fuel consumption in mol per second

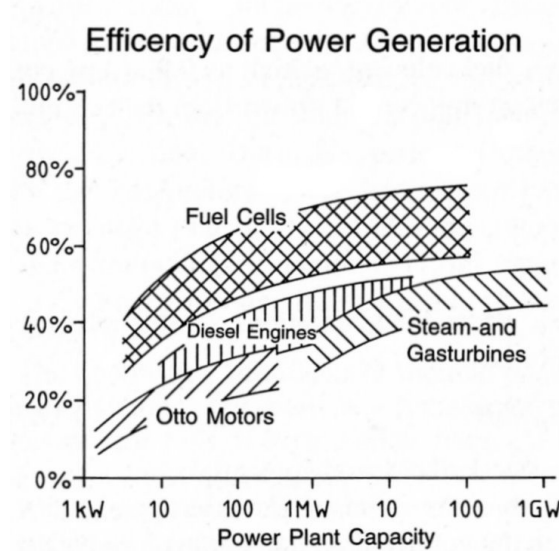


**Figure 2.5.:** The efficiency of power generators varies as a function of the scale. The efficiency domain of the fuel cell is very broad, which is due to the large spectrum of fuel cell systems.[29]

**Overall efficiency** The overall fuel cell efficiency is the product of all individual efficiencies:

$$\epsilon_{FC} = \epsilon_{th} \cdot \epsilon_V \cdot \epsilon_C = \frac{\Delta H - T\Delta S}{\Delta H} \cdot \frac{U}{U_0} \cdot \frac{I \cdot N}{F \cdot n \cdot v} \approx 0.41 \quad (2.37)$$

In this example the efficiency is very similar to the maximal diesel engine efficiency. But the spectrum of fuel cell systems is very broad and the efficiency of these differ strongly. By improving the electrode kinetics or running the fuel cell at lower current densities it is possible to increase the efficiency. Furthermore, if the fuel utilization is unity, which could be accomplished by fuel recirculation, the efficiency in this example would be about  $\epsilon_{FC} \approx 0.48$ . Moreover, in the SOFC the voltage efficiency could be higher due to the insignificant activation overpotential. In fact the efficiency of a long life (>40,000h) SOFC stack in Jülich is  $\epsilon_{FC} = 64\%$ [28]. The maximal diesel efficiency is obtained only under perfect conditions. For example, the diesel engine efficiency of a car in traffic congestion drops down to less than 10%. The efficiency of a possible fuel cell driven car would still be much higher. In Fig. (2.5) an efficiency comparison of different power generating systems is presented, which also shows the broad spectrum of fuel cell efficiencies.

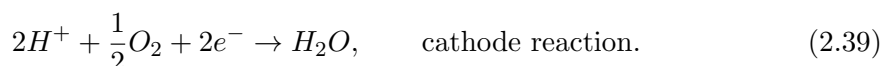
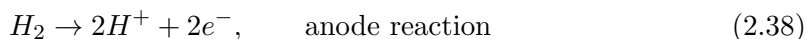
Eq. (2.37) represents the electric energy only. If thermal discharge is also used by power-heat coupling, an efficiency of about 85% is possible.

## 2.5. Fuel cell types

There are many different types of fuel cells. The division between fuel cell types is done by the electrolyte. The direct methanol fuel cell is an exception, since it is a special type of the proton exchange membrane fuel cell. This is meaningful, as the electrolyte determines which kind of ions are transported, which temperature range the fuel cell can be run in, and which catalyst can be used. Each type of fuel cells has its own advantages and drawbacks. However, one common reason why they are not produced in series yet is, that all fuel cell types are too expensive, and therefore cannot compete with state of the art power generators.

### 2.5.1. Proton exchange membrane fuel cell (PEMFC)

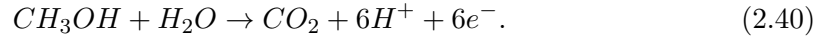
The heart of the PEMFC is the proton conducting polymer membrane. For the time being fuel cells with Nafion membranes have the highest power density among the PEMFCs. Similar to Teflon, the Nafion membrane consists of polymer chains. While the Teflon polymers are linear chains of  $CF_2$  monomers, the Nafion chain has additional sulphonal groups ( $SO_3H$ ). If water is added to the polymer, the sulphonal groups dispense hydrogen ions. Hence, the membrane becomes proton conductive when humidified. The electrodes are usually made of platinum-particle containing carbon-carriers. Either pure hydrogen or hydrogen from reformation processes is feed into the PEMFC. The cathode can be flooded by pure oxygen, or by air. Since the PEMFC is a hydrogen/oxygen fuel cell and the transported ion is the proton, the following reactions take place at the electrodes:



The PEMFC can produce high power densities of some hundred milliwatts per square centimeter. It has high mechanical stability and operating times of some ten thousand hours. As mentioned before, the electrochemical reaction only takes place at the three-phase boundaries, and in the direct vicinity. Therefore, all platinum particles are useless, which are not located at a three phase boundary. This leads to platinum usages being one order of magnitude higher than economically tolerable. Furthermore, the ion conductivity of the Nafion membrane depends on the humidification, which leads to a complicated water management. If the humidification is too low, the membrane dries out and the conductivity drops to zero. If the humidification is too high, the membrane erodes and the conductivity drops, too. In addition, the platinum catalyst is very sensible to carbon monoxide poisoning, as the  $CO$  molecule binds the active locations of the catalyst and occupies them for a long time.

### 2.5.2. Direct methanol fuel cell (DMFC)

As mentioned before, the DMFC is a modification of the PEMFC. The fuel cell design is equal to the design of the PEMFC, but the reactions are rather different. In contrast to the gaseous hydrogen in the PEMFC, the fuel in this type is feed in liquid form. It is a water-methanol mix. The methanol oxidation at the anode can be described by the following stoichiometric formula:



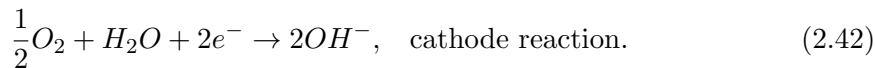
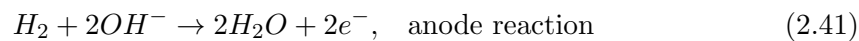
Since protons are transported across the membrane as well, the oxygen reduction is equal to Eq. (2.39).

Storing hydrogen is a major issue, since even under a pressure of 200 bar, the density is very low. Furthermore the hydrogen compression is a highly energy consuming process. But as the fuel is feed in liquid form into the DMFC, no gas tanks are required. Since methanol can be stored in liquid form under a pressure of 8 bar, only simple tanks are necessary. Therefore, the peripheral systems of the DMFC are less complex and less expensive. Thus, it is even possible to build very small fuel cell systems (e.g. as an energy source for cell phones). The water in the liquid fuel ensures the humidification of the membrane, thus, no membrane dehydration occurs.

In spite of the advantages of the DMFC there are a lot of drawbacks. The reaction kinetics at the anode are slower than in the PEMFC. This leads to lower power densities and higher platinum loads. In fact the required platinum is by a factor of twenty higher than in a PEMFC. Furthermore  $CO_2$  is produced in the electrochemical reaction, which needs to be removed from the anode to ensure high fuel concentration at the three-phase boundaries. Thus, a lower maximal current density due to concentration overpotential can be expected.

### 2.5.3. Alkaline fuel cell (AFC)

The electrolyte in the alkaline fuel cell is a liquid base. Mostly it is concentrated caustic potash ( $KOH$ ). For low temperature applications ( $60^\circ C - 90^\circ C$ ) the concentration is about 35-50 wt.-%. The AFC had been applied in the Apollo space shuttle program, using caustic potash concentrations of about 85 wt.-% at operating temperatures of about  $250^\circ C$ <sup>12</sup>. In contrast to the acid based fuel cells, no protons are transported in the AFC but hydroxide ions  $OH^-$ . This leads to a water production at the anode and a water consumption at the cathode. The respective reactions are:

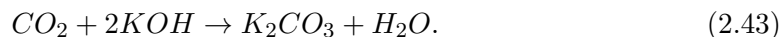


In virtue of the alkaline environment, the reaction kinetics are higher than in fuel cells with acidic electrolytes. Thus it is possible to achieve high current densities, and high

<sup>12</sup>The Apollo alkaline fuel cell had an operating pressure of 200 bar to prevent potash boiling.

efficiencies without the usage of platinum catalyst. Typical catalyst materials in the AFC are nickel and silver. Since these metals are much cheaper than platinum, it is more affordable than the PEMFC. The circulating electrolyte facilitates the water and heat management, as both can be removed via the electrolyte loop.

Nevertheless, the AFC has drawbacks, as well. If caustic potash and carbon dioxide has contact, potassium carbonate is formed:



In addition the following reaction takes place under carbon dioxide containing ambience:



First, this leads to a dilution of the caustic potash, as the  $KOH$  is consumed. Secondly, the hydroxide ions are lost, which carry the ionic current in the AFC. Thirdly, the carbonate molecules do not solve in water and thus deposit inter alia in the pores of the electrolyte confining membrane and clog them. Therefore the carbon dioxide needs to be removed from any participating gas flows. This can be accomplished by using pure oxygen or filtering carbon dioxide from air<sup>13</sup>.

A derivative of the AFC is the **Molten Carbonate Fuel Cell (MCFC)**. The electrolyte is a molten salt consisting of alkali carbonates, which is conducting for carbon oxide ions  $CO_3^{2-}$ . Since alkali carbonates melt at higher temperatures, the operating temperature is above 600°C. In the MCFC there are no problems regarding carbon dioxide. Of course the MCFC has its own problems concerning the high temperature and the molten salt electrolyte. This type of fuel cell will not be discussed here in detail.

#### 2.5.4. Solid oxide fuel cell (SOFC)

The operating temperature of the solid oxide fuel cell is the highest of all fuel cell types. It is above 700°C, in some assemblies even above 1000°C. The electrolyte of the SOFC is an oxygen ion  $O^{2-}$  conducting solid oxide, mostly **Yttrium Stabilized Zirconium oxide (YSZ)**. The anode is a composite consisting of nickel and YSZ to enlarge the overall three phase boundary, while the cathode consists of **Lanthanum Strontium Manganese (LSM)**. If hydrogen is feed into the SOFC the oxidizing of hydrogen at the anode and the oxygen reduction at the cathode are given by the reaction equations Eq. (2.2) and Eq. (2.3). Though other fuel types, like natural gas and ammonia, can directly be used in the SOFC.

Along with the high temperatures come advantages. As reaction kinetics are faster at higher temperatures, no noble catalyst is needed and the activation losses are minimal. Due to the solid oxide electrolyte neither poisoning nor pore clogging occurs and no water management is needed. Furthermore, the SOFC has a good tolerance to overload, underload and short-circuiting.

---

<sup>13</sup>Carbon dioxide can be removed from the air by a soda lime filter, or by leading the air through old caustic potash.

Due to the high temperatures there are on the one hand the mentioned advantages, on the other hand there are also many disadvantages. Since the entropic losses are linear in temperature (c.f. Eq. (2.5)), both the OCV and the thermodynamic efficiency is lower than in other fuel cell types. However, the higher entropic losses can be used to maintain the high operating temperature. Furthermore, expensive interconnector and casing materials are necessary. These are built of cermets (e.g.  $LaCrO_3$ ) or iron/chrome alloys. To use interconnectors built of standard stainless steel, temperatures of approximately  $550^\circ\text{C}$  should not be exceeded, since the hardness of stainless steel drops considerably above this temperature. The mechanical properties of the SOFC materials are crucial. The thermal expansion coefficient of all materials must be sufficiently low and as equal as possible among one another to prevent ruptures in the structure. Even SOFCs with thermal stable materials need about fifteen minutes to heat up, which makes the application of SOFCs in the automotive market very problematic for the time being.

By lowering the operating temperature under  $550^\circ\text{C}$  the interconnector material issue could be solved. Since the ion conductivity of YSZ at these temperatures is too low, it could no longer be used in such an intermediate temperature SOFC. Candidates for YSZ replacement are cerium oxide and gadolinium oxide. Although these materials have higher ionic conductivities at lower temperatures, they come with different problems. More details about electrolyte materials, their advantages and disadvantages are given in chapter 6.

This finishes the general overview over fuel cells. In the following chapter the Density Functional Theory used to calculate the ionic motion in electrolytes accurately, is described



# 3. Electronic Structure Calculations

## 3.1. Density Functional Theory

To understand and describe the physical and chemical properties of a material from a theoretical point of view it is necessary to treat the crystal structure (or the amorphous state) of the material quantum mechanically. [30] To do this exactly, the many-body problem of all electrons and nuclei with the Coulomb interactions between them has to be solved, i.e. solving the many-body Schrödinger equation

$$\mathcal{H}_{MB}\psi\left(\vec{r}_1, \dots, \vec{r}_N; \vec{R}_1, \dots, \vec{R}_N\right) = E\psi\left(\vec{r}_1, \dots, \vec{r}_n; \vec{R}_1, \dots, \vec{R}_{N_I}\right) \quad (3.1)$$

with the many-body Hamiltonian  $\mathcal{H}_{MB}$ , the energy eigenvalue  $E$ , the many-body wavefunction  $\psi$  and electronic and ionic coordinates  $r_i, R_i$ . The many-body Hamiltonian can be written as:

$$\mathcal{H}_{MB} = T_e + T_I + V_{II} + V_{ee} + V_{eI}. \quad (3.2)$$

The first two terms  $T_e, T_I$  are the kinetic energies of the electrons and ions,  $V_{ee}$  and  $V_{II}$  are the repulsive Coulomb pair potentials between the electrons and the ions respectively. The last term denotes the attractive interaction between ions and electrons. Due to the coulomb interactions between the electrons it is not possible to solve Eq. 3.1 exactly and a simple approach is strongly limited due to the exponential dependence of the computational demand on the particle number.

To simplify the many-body problem, the electronic and ionic degrees of freedom can be separated from each other

$$\psi\left(\vec{r}_1, \dots, \vec{r}_N; \vec{R}_1, \dots, \vec{R}_{N_I}\right) = \psi\left(\vec{r}_1, \dots, \vec{r}_N; \left\{\vec{R}_i\right\}\right) \chi\left(\vec{R}_1, \dots, \vec{R}_{N_I}\right). \quad (3.3)$$

This is possible, since the mass of the nuclei is three to four orders of magnitude larger than the one of the electrons. Therefore, the electrons can nearly instantaneous adapt to any movement of the nuclei. This is the Born-Oppenheimer approximation. This again permits to treat the ionic movement classically by integrating the Newtonian equations of motion while computing the electronic ground state including the position of the nuclei as external parameters

$$\mathcal{H}_{MB}\psi\left(\vec{r}_1, \dots, \vec{r}_N; \left\{\vec{R}_i\right\}\right) = E\left(\left\{\vec{R}_i\right\}\right) \psi\left(\vec{r}_1, \dots, \vec{r}_N; \left\{\vec{R}_i\right\}\right) \quad (3.4)$$

with

$$\mathcal{H}_{MB} = T_e + V_{ee} + V_{eI}. \quad (3.5)$$

$V_{eI}$  is typically expressed by  $V_{\text{ext}}$ , which additionally incorporate any potential due to external fields, like electric or magnetic fields. Although being a strong simplification, Eq. 3.4 is still neither analytically nor numerically solvable.

There are two noteworthy methods preceding the Density Functional Theory (DFT), the Hartree-Fock (HF) method and the Thomas-Fermi method. In 1927 Hartree [31] devised a wave-function method describing the many-body system with one single Slater determinant. He called it the “self-consistent field method”, since the wave-functions are iteratively approximated by considering the electrons in a mean field created from all other electrons in the system. This method is not based on empirical parameters, and leads in some cases to accurate results. The original Hartree method only included the exchange interaction of symmetric wave-functions but not of antisymmetric. This has been mended by the addition of the Fock-operator in the 1930s. However, the biggest caveat is the disregard of the correlation effects leading to strong deviations to the experiment in many systems.

Also in 1927, Thomas [32] and Fermi [33] proposed a method that determines the kinetic energy of a system of classically treated electrons with an external potential originating from ions in dependence of the charge density of a free electron gas without the explicit knowledge of the many-body wave-function. This approximation gives in most systems inaccurate results, especially the shell structure of atoms is not reproduced [34]. However, this approximation gave the idea for DFT, which was born in the 1960s.

### 3.1.1. Hohenberg-Kohn Theorem

In 1964 Hohenberg and Kohn [35] published an article that would revolutionize the computational material science. It connects the ground state charge density  $n_0$  with the many-body wave-function and thus with all physical and chemical quantities of the system. The basis for the DFT was given in two theorems:

**Theorem I:** *For any system of interacting electrons in the external potential  $V_{\text{ext}}(\vec{r})$ , originating from the ions in the system, the potential  $V_{\text{ext}}(\vec{r})$  is determined uniquely, up to a constant, by the ground state charge density  $n_0(\vec{r})$ .*

Following Eq. 3.4 the wave-functions of the N-electron system are functionals of the external potential  $\psi[V_{\text{ext}}(\vec{r})]$  and thus of the ground-state charge density  $\psi[V_{\text{ext}}[n_0(\vec{r})]]$ . Consequently the expectation values of all observables  $\langle \psi | \mathcal{O} | \psi \rangle$  are functionals of the ground state density.

**Theorem II:** *The total energy functional  $E[n]$  is minimized by the ground-state electron density  $n_0$  if the trial densities  $n(\vec{r})$  are restricted by the conditions  $n(\vec{r}) \geq 0$  and  $\int n(\vec{r})d^3r = N$*

$$\left. \frac{\delta}{\delta n} \left[ E[n] - \mu \left( \int n(\vec{r})d^3r - N \right) \right] \right|_{n=n_0} = 0, \quad (3.6)$$

where  $\mu$  is a Lagrange parameter ensuring the observation of the electron conservation constraint (chemical potential).

Following theorem I and II, the ground-state energy of the system can be determined by minimizing the energy functional  $E[n(\vec{r})]$  with respect to the density

$$E[n_0(\vec{r})] = \min_n E[n(\vec{r})]. \quad (3.7)$$

Following Levy [36] the unique energy functional can be defined as the minimum of the Hamiltonian over all wave-functions  $\psi$

$$E[n(\vec{r})] = \min_{\psi} \langle \psi | T_e + V_{ee} + V_{\text{ext}} | \psi \rangle. \quad (3.8)$$

If the minimization is already conducted over the whole Hilbert-space, the resulting energy and density corresponds to the ground state of the system  $\psi_0$ ,  $E_0$  and  $n_0$ , rendering Eq. 3.7 unnecessary. However, a minimization performed in the vast Hilbert-space is practically impossible. Alternatively, it is feasible to constrain the minimization by searching only for the minimizing wave-functions for a given density  $n(\vec{r})$

$$E[n(\vec{r})] = \min_{\psi} \{ \langle \psi | T_e + V_{ee} + V_{\text{ext}} | \psi \rangle, \quad \langle \psi | \hat{n}(\vec{r}) | \psi^* \rangle = n(\vec{r}) \}, \quad (3.9)$$

with the density operator  $\hat{n}(\vec{r}) = \sum_{i=1}^N \delta(\vec{r} - \vec{r}_i)$ . Eq. 3.9, when used in conjunction with Eq. 3.7, delivers the ground state of the system. This apparent complication leads in most cases to an immense reduction of the complexity. If a system independent functional (i.e. not depending on the external potential)

$$F[n(\vec{r})] = \min_{\psi} \langle \psi | T_e + V_{ee} | \psi \rangle \quad (3.10)$$

is introduced and the energy functional (Eq. 3.8) is written is the form

$$E[n(\vec{r})] = F[n(\vec{r})] + \int d^3r v_{\text{ext}}(\vec{r})n(\vec{r}), \quad (3.11)$$

it seems to be possible to execute the minimization only over  $n(\vec{r})$  and not over  $\psi$  at all. This, however, would require that  $F[n(\vec{r})]$  can be given independently of the many-body wave-function  $\psi$ , which is in general not the case.

With this, the ground state density is conceptually determined exactly, and by that all ground state observables of the system. However, the functional  $F[n(\vec{r})]$  is not known explicitly and the minimizations have to be performed in the vast Hilbert-space of the system. Luckily, one year later Kohn and Sham found a way to reduce the complexity further and find approximations for the universal functional  $F[n(\vec{r})]$ .

### 3.1.2. Kohn-Sham Equations

Kohn and Sham [37] had the idea to introduce a fictitious system of non interacting electrons with an effective external potential  $v_{\text{eff}}(\vec{r})$ . This potential is constructed in a way that the density of the not interacting system is equal to the density of the interacting system. In a not interacting system  $V_{ee}$  vanishes and  $F[n(\vec{r})]$  is reduced to the kinetic energy of the electrons  $T_e$  leading to a density functional

$$E[n(\vec{r})] = T_e[n(\vec{r})] + \int d^3r v_{\text{eff}}(\vec{r})n(\vec{r}). \quad (3.12)$$

Applying the second theorem of Hohenberg and Kohn to this equation leads to

$$\frac{\delta}{\delta n(\vec{r})} \left[ E[n(\vec{r})] - \mu \left( \int n(\vec{r})d^3r - N \right) \right] = \frac{\delta T_e[n(\vec{r})]}{\delta n(\vec{r})} + v_{\text{eff}}(\vec{r}) - \mu = 0. \quad (3.13)$$

The kinetic energy of the non-interacting electrons  $T_e[n(\vec{r})]$  can be constructed by the single-electron wave-functions  $\phi_i(\vec{r})$  leading to the first set of the Kohn-Sham equations

$$n(\vec{r}) = \sum_i^{\text{occ}} |\phi_i(\vec{r})|^2 \quad (3.14)$$

and

$$T_e[n(\vec{r})] = \sum_i^{\text{occ}} \int \phi_i^*(\vec{r}) \left( -\frac{\hbar^2}{2m} \nabla^2 \right) \phi_i(\vec{r}) d^3r. \quad (3.15)$$

Here the index  $i$  refers to both the spatial and the spin quantum numbers and the sum covers the  $N$  lowest eigenstates to observe the Pauli principle. The variation of Eq. 3.12 with respect to the one-particle wave-function yields the last Kohn-Sham equation, which is a one particle Schrödinger equation of the fictitious non interacting system

$$\left[ -\frac{\hbar^2}{2m} \nabla^2 + v_{\text{eff}}(\vec{r}) - \mu \right] \phi_i(\vec{r}) = \epsilon_i \phi_i(\vec{r}). \quad (3.16)$$

Solving Eq. 3.14 to 3.16 self-consistently leads to the correct many-body ground state, if  $v_{\text{eff}}$  would be known exactly. This is generally not possible, only approximations can be given. By writing the density functional in the form

$$E[n(\vec{r})] = T_e[n(\vec{r})] + \int d^3r v_{\text{ext}}(\vec{r})n(\vec{r}) + \frac{e^2}{2} \int \frac{n(\vec{r})n(\vec{r}')}{|\vec{r} - \vec{r}'|} d^3r d^3r' + E_{xc}[n(\vec{r})] \quad (3.17)$$

the necessary approximations can be reduced further. The third term accounts for the Coulomb interaction of the charge density distribution  $n(\vec{r})$ , the Hartree energy. The last term is the so called exchange-correlation energy functional defined as

$$E_{xc}[n(\vec{r})] = F[n(\vec{r})] - T[n(\vec{r})] - \frac{e^2}{2} \int \frac{n(\vec{r})n(\vec{r}')}{|\vec{r} - \vec{r}'|} d^3r d^3r'. \quad (3.18)$$

All many-body effects that are not included in the explicit part of Eq. 3.17 are moved into this functional. This quantity is typically much smaller than  $F[n(\vec{r})]$ , and finding a necessary approximation for it gives rise to a much smaller error. With

$$v_{xc}[n(\vec{r})](\vec{r}) = \frac{\delta E_{xc}[n(\vec{r})]}{\delta n(\vec{r})} \quad (3.19)$$

the effective potential is given by

$$v_{\text{eff}}(\vec{r}) = v_{\text{ext}}(\vec{r}) + e^2 \int \frac{n(\vec{r}')}{|\vec{r} - \vec{r}'|} d^3r' + v_{xc}[n(\vec{r})](\vec{r}). \quad (3.20)$$

With this formalism it is possible to calculate the electronic ground state in a much more efficient way, than it has been possible before. However, as can be seen from it, only the electronic ground state can be determined. Thus, for excited states at absolute temperatures different approaches are necessary. Furthermore, in the here presented method only equilibrium values can be determined, but time dependent DFT is an available extension. As pointed out before there are still approximations necessary for the exchange-correlation energy in Eq. 3.20. The two most basic ones, the Local Density Approximation (LDA) and the Generalized Gradient Approximations (GGA), will be introduced in the next subsection.

### 3.1.3. Exchange-Correlation Approximations

**Local Density Approximation (LDA)** The most basic approach to estimate  $E_{xc}$  is the local density approximation, which has already been introduced by Kohn and Sham. Despite its simplicity it is amazingly successful and has been used for many years, and is partly still used nowadays. In the LDA it is assumed that each electron in the inhomogeneous system has a local neighborhood of a completely homogeneous electron gas. Thus, the exchange-correlation energy  $E_{xc}$  can be written as

$$E_{xc}[n(\vec{r})] = \int d^3r n(\vec{r}) v_{xc}^{LDA}(n(\vec{r})), \quad (3.21)$$

where  $v_{xc}^{LDA}(n(\vec{r}))$  is the exchange-correlation potential of an homogeneous electron gas, which is a function not a functional of the density  $n(\vec{r})$ . In this case it can be written as a sum of the exchange contribution and the correlation contribution

$$v_{xc}^{LDA}(n(\vec{r})) = v_x(n(\vec{r})) + v_c(n(\vec{r})). \quad (3.22)$$

The exchange part of the  $v_{xc}^{LDA}(n(\vec{r}))$  can analytically be determined by the Hartree-Fock method

$$v_x(n(\vec{r})) = -2 \left( \frac{3}{\pi} \right)^{\frac{1}{3}} n^{\frac{1}{3}}. \quad (3.23)$$

The Hartree-Fock method, being a mean-field method, neglects the correlation of electrons with opposite spins. In general the correlation effects are harder to determine, and a quantum Monte-Carlo calculation of the homogeneous electron gas had to be employed to obtain this contribution. This has been done by Ceperley and Alder [38] and their numerical results have been interpolated to all densities by e.g. Perdew and Wang [39].

**Generalized Gradient Approximation (GGA)** In cases where the density locally varies too much and thus LDA becomes a too crude approximation, the GGA will yield better results. The generalized gradient approximation is less an exact instruction how to estimate  $E_{xc}$ , as LDA is, but rather a general scheme for more accurate approximations including the gradient of the density. The exchange-correlation energy is implicitly given by

$$E_{xc}[n(\vec{r})] = \int d^3r f(n(\vec{r}), \nabla n(\vec{r})) \quad (3.24)$$

where  $f(n(\vec{r}), \nabla n(\vec{r}))$  is chosen in each scheme differently. In the past there have been many different flavors of GGA, but the most modern one (and the one used in this thesis) is the variant of Perdew, Burke, Ernzerhof (PBE-GGA) [40] yielding the most accurate lattice constants of the GGA functionals.

In general it can be noted that the LDA functional tends to over-bind the ions in the system leading to too small lattice constants and GGA functionals tend to under-bind leading to too large lattice constants.

## 3.2. Vienna Ab Initio Package (VASP)

VASP is a commercial DFT planewave Code using pseudopotentials to calculate the electronic structure of ionic systems. Besides calculating the ground state energy of the system, it can be used to compute many other physical quantities like forces, stress, vibrational frequencies, magnetic moments etc. The forces acting on the ions can be used to find the ionic ground state of the system, or to be more exact the next local minimum of the ionic potential surface. Furthermore ab-initio molecular dynamics calculations can be executed.

### 3.2.1. Plane Wave Expansion and Brillouin zone sampling

#### 3.2.1.1. Plane wave basis set

When crystals are computed, it is very efficient to use a small computational cell and apply Periodic Boundary Conditions (PBC) since the crystal is translational invariant under a translation of a vector  $\vec{T} = n_1\vec{a}_1 + n_2\vec{a}_2 + n_3\vec{a}_3$ , where the  $\vec{a}_k$  are the lattice

vectors of the crystal and  $n_i$  are integers (the lattice vectors define the Wigner-Seitz cell of the crystal). From these direct lattice vectors one can obtain the reciprocal lattice vectors  $\vec{b}_l$  with  $\vec{a}_k \cdot \vec{b}_l = 2\pi\delta_{kl}$ . The periodicity of the lattice obviously also carries over to the reciprocal space and the reciprocal lattice is invariant under a translation of the reciprocal lattice vector

$$\vec{G}(m_1, m_2, m_3) = \vec{G}_{m_l} = m_1\vec{b}_1 + m_2\vec{b}_2 + m_3\vec{b}_3, \quad (3.25)$$

with  $m_l$  being integers. The three vectors  $\vec{b}_l$  define the boundaries of the Brillouin-zone (BZ) – the analogue of the Wigner-Seitz cell in the reciprocal space. Following the Bloch theorem the wave-functions of a periodic potential can be described by plane waves:

**Bloch Theorem:** *The eigenfunctions of the wave equation for a periodic potential can be written as the product of plane waves  $\exp(i\vec{k}\vec{r})$  and a function  $u_{\vec{k}}(\vec{r})$  with the periodicity of the lattice*

$$\Psi_{\vec{k}}(\vec{r}) = u_{\vec{k}}(\vec{r}) \cdot e^{i\vec{k}\vec{r}}, \quad (3.26)$$

where  $\vec{r}$  is a point in real space and  $\vec{k}$  a point in the reciprocal space.

The Kohn-Sham orbitals can be represented in Bloch waves

$$\phi_{i,\vec{k}}(\vec{r}) = u_{i,\vec{k}}(\vec{r}) \cdot e^{i\vec{k}\vec{r}}, \quad (3.27)$$

where  $\vec{k}$  is in the first BZ and the periodic function can be expanded in a Fourier series

$$u_{i,\vec{k}} = \frac{1}{\sqrt{\Omega}} \sum_{m_l} c_{i,m_l}(\vec{k}) \cdot e^{i\vec{G}_{m_l}\vec{r}}. \quad (3.28)$$

The  $c_{i,m_l}$  are the expansion coefficients for the band  $i$  at k-point  $\vec{k}$  and the sum goes in principle over all  $\vec{G}_{m_l}$  for  $m_l = 0 \dots \infty$  independently for all three integers  $m_l$ . The normalization constant  $1/\sqrt{\Omega}$  corresponds to the volume of the BZ  $\Omega$ . Consequently, the Kohn-Sham orbitals expanded in plane waves are given by

$$\phi_{i,\vec{k}}(\vec{r}) = \frac{1}{\sqrt{\Omega}} \sum_{m_l} c_{i,m_l}(\vec{k}) \cdot e^{i(\vec{G}_{m_l} + \vec{k})\vec{r}} \equiv \sum_{\vec{q}} c_{i,\vec{q}}(\vec{k}) \cdot e^{i\vec{q}\vec{r}}, \quad \vec{q} = \vec{k} + \vec{G}_{m_l}. \quad (3.29)$$

The computational problem is shifted now from the determination of the wave-functions to the calculations of the  $c_{i,m_l}$ . Obviously, it is not possible to expand the plane waves to  $m_l = \infty$ , therefore, a cutoff criterion is introduced. The kinetic energy in the plane-wave representation is given by

$$T_{PW} = \frac{1}{2} \left| \vec{G}_{m_l} + \vec{k} \right|^2. \quad (3.30)$$

Since the coefficients  $c_{i,\vec{k}}(\vec{r})$  decrease exponentially with increasing kinetic energy, an energy cutoff for the plane wave expansion is a reasonable choice. Only plane waves

fulfilling

$$\frac{1}{2} \left| \vec{G}_{m_l} + \vec{k} \right|^2 < E_{\text{cut}} \quad (3.31)$$

are determined in the calculation. The accuracy and efficiency of the calculation is sensibly affected by the choice of  $E_{\text{cut}}$ . Too small values give imprecise results and too large values result in unnecessary high computational costs.

The advantages of using plane wave as a basis to calculate the electronic structure of a periodic crystal are as follows:

- The basis set is independent from atomic configuration and atomic species, which means the basis set does not need to be adapted when the positions of the ions change.
- The forces acting on the ions are given by the Hellmann-Feynman forces (c.f. subsection 3.2.3) and no basis set corrections are needed (no Pulay forces<sup>1</sup>)
- FFTs can quickly convert from real space mesh to the reciprocal space mesh and back
- It is possible by increasing  $E_{\text{cut}}$  to systematically enhance the accuracy of the calculations

### 3.2.1.2. Charge density in the plane wave expansion and Brillouin zone sampling

In the plane-wave basis the density is computed by a sum over all occupied orbitals and the average over the Brillouin zone [41]

$$n(\vec{r}) = \sum_{i_{\text{occ}}} \frac{1}{\Omega} \int_{\Omega} n_{i,\vec{k}}(\vec{r}) d^3k. \quad (3.32)$$

The density arising from each orbital  $i$  at a position  $\vec{k}$  is given in reference to Eq. 3.14 by

$$n_{i,\vec{k}}(\vec{r}) = \left| \phi_{i,\vec{k}}(\vec{r}) \right|^2 = \frac{1}{\Omega} \sum_{m_l, m'_l} c_{i,m_l}^*(\vec{k}) c_{i,m'_l}(\vec{k}) e^{i(\vec{G}_{m'_l} - \vec{G}_{m_l}) \cdot \vec{r}}. \quad (3.33)$$

With the substitution  $\vec{G}_{m'_l} = \vec{G}_{m_l} + \vec{G}$  the Fourier transform is given by

$$n_{i,\vec{k}}(\vec{G}) = \frac{1}{\Omega} \sum_{m_l} c_{i,m_l}^*(\vec{k}) c_{i,m_l}(\vec{k}). \quad (3.34)$$

---

<sup>1</sup>The Pulay force is an additional force-term, arising from the variation of the basis set.

To numerically approach Eq. 3.32 the integral is replaced by a sum over a limited number of k-points  $N_k$  sampling the BZ

$$n(\vec{r}) = \sum_{i_{\text{occ}}} \frac{1}{N_k} \sum_{\alpha=1}^{N_k} n_{i, \vec{k}_\alpha}(\vec{r}). \quad (3.35)$$

A typical choice to sample the k-points is a uniform grid generated in the Monkhorst-Pack procedure

$$\vec{k}_\alpha = m_{\alpha'l} \vec{b}_l \quad (3.36)$$

with

$$m_{\alpha'l} = \frac{2p_{\alpha'l} - N_l - 1}{2N_l}, \quad \text{with} \quad p_{\alpha'l} = 1 \dots 2N_l, \quad (3.37)$$

where  $N_l$  denotes the number of k-points in the direction of  $\vec{b}_l$  and the index  $\alpha'$  is the index of k-point planes in this direction. This mesh samples the BZ equally, which is not necessary in most cases since symmetry operations can map equivalent k-points onto each other. Thus, a sampling of the irreducible BZ is sufficient for computations of the density.

### 3.2.2. Determining the electronic ground state

There are basically two distinct ways to compute the electronic ground state of a system, the direct minimization of the DFT functional and the iterative self-consistent update of charge densities and wave-functions [42, 43]:

1. The direct minimization of the DFT functional Eq. 3.17 is either based on the Car-Parinello approach (pseudo-Newton dynamics for the electronic degrees of freedom) or the conjugate gradient method. Although being very elegant this method has some caveats. It is computationally not easy to keep the wave-functions orthogonal and in metallic systems a linear slow-down occurs, which is proportional to the largest extent of the computational cell.
2. The iterative self-consistency cycle sequentially updating the occupied and some unoccupied states together with an update of the charge density (i.e. solving the Kohn-Sham equations Eq. 3.14 to 3.16): The computation starts with a trial density  $n(\vec{r})$  and trial wave-functions  $\phi_i$  with the band index  $i$  (usually the superposition of atomic wave-functions yields the fastest convergence, from which the initial charge density is derived)
  - a) The effective potential is constructed from the charge density  $n(\vec{r})$  using Eq. 3.20.
  - b) The one particle Schrödinger equation (Eq. 3.16) is solved yielding the wave-function  $\phi_i$  and the one-particle energy eigenvalues  $\epsilon_i$ . Either the “blocked Davidson algorithm” (DAV), the “residual minimization scheme, direct inversion in the iterative subspace” (RMM-DIIS) or a combination of both methods is used to solve this equation (DAV and RMM-DIIS are described in

the appendix A.1). Since the RMM-DIIS scheme always optimizes the wave-functions to the nearest minimum, initialization has to be done carefully. To get out of this plight, a sub-space rotation is employed that diagonalizes the Hamiltonian in the subspace spanned by all eigenvalues included in the iteration scheme. The DAV algorithm is slower than the RMM-DIIS method and performs less well when executed in parallel. It is, however, always stable. A good trade-off between speed and stability is the combination of DAV and RMM-DIIS by first executing a specific number of DAV steps to pre-converge the charge density and then switching to the residual minimization scheme.

- c) With the updated wave-functions and the occupation numbers  $f_i$  one obtains the new real charge density of the system:

$$n(\vec{r}) = \sum_i f_i \langle \phi_i(\vec{r}) | \phi_i(\vec{r}) \rangle \quad (3.38)$$

- d) The new charge density is mixed with the previous one. The correct mixing method and strength influences the convergence of the self-consistency cycle strongly. In VASP the Broyden mixing [44] with an initial Kerker mixing [45] is used (the mixing schemes are described in appendix A.2). If no convergence is achieved the self-consistency cycle is continued by going back to a).

For insulators and molecules both approaches, the direct minimization of the functional and the iterative self-consistency cycle, work equally well. However, for metals the latter approach is significantly better, therefore, only the self-consistent cycle is applied in VASP.

### 3.2.3. Ionic relaxation

**Hellmann-Feynman (HF) Theorem** The Hellmann-Feynman Theorem directly follows from the Rayleigh-Ritz variational principle. Considering the variation of the wave-function

$$\langle \delta\psi | H | \psi \rangle + \langle \psi | H | \delta\psi \rangle, \quad (3.39)$$

and  $\psi$  is the ground-state wave-function, then the Hamiltonian is equal to its eigenvalue, the energy  $E$ . This follows from the Rayleigh-Ritz variational principle

$$E = \min_{\Psi} \langle \Psi | H | \Psi \rangle \quad (3.40)$$

where  $\Psi$  are trial wave-functions<sup>2</sup>. From these two equations follows

$$E[\langle \delta\psi | \psi \rangle + \langle \psi | \delta\psi \rangle]. \quad (3.41)$$

---

<sup>2</sup>In fact, from Eq. 3.40 it directly follows, that  $\delta\Psi$  vanishes, since it is the ground state wave-function of the system.

Since the wave-functions are normalized ( $\langle \psi | \psi \rangle = 1$ ) follows

$$E[\delta \langle \psi | \psi \rangle] = 0. \quad (3.42)$$

Thus the variations  $\delta\psi$  vanish for the ground-state.

In the Kohn-Sham formalism this relates to

$$E_0 = \min_n E[n(\vec{r})], \quad (3.43)$$

where  $E[n(\vec{r})]$  is the density functional (Eq. 3.17). Hence, the variations of the ground-state density  $\delta n$  vanish. Due to Eq. 3.14, also the variations of the one particle wave-functions  $\delta\phi = 0$  vanish. The analogy can be shown even more clearly: Start from the one particle Schrödinger equation (Eq. 3.16)

$$H_{\text{eff}}\phi_i = \epsilon_i\phi_i \quad (3.44)$$

and let  $\psi$  be the Slater determinant of all KS orbitals  $\phi_i$  and let  $H'_{\text{eff}}$  be an effective Hamiltonian of all particles, then the variation of the wave-function can be written as

$$\langle \delta\psi | H'_{\text{eff}} | \psi \rangle + \langle \psi | H'_{\text{eff}} | \delta\psi \rangle, \quad (3.45)$$

which looks exactly like Eq. 3.39, just  $H$  does not include the pair potentials and  $\psi$  is a Slater determinant of all non-interacting electrons in the system. In fact, this analogy expands to the complete context of wave-functions and the HF theorem. As an example, it can be deduced without further inspection that Pulay forces also appear in the Kohn-Sham formalism. However, in non-local basis sets, as in plane-waves, no Pulay forces are present when ions are displaced, since the basis set is independent of the ionic positions. When changing the shape of the computational cell, they still appear, since the plane-wave basis set depends on the cell shape and size.

Applying the HF theorem in the Kohn-Sham formalism to the variation of ionic positions, the HF forces follow:

$$\vec{F} = -\frac{\partial E}{\partial \vec{R}} = -\left\langle \phi \left| \frac{\partial}{\partial \vec{R}} H \right| \phi \right\rangle. \quad (3.46)$$

Computationally it only requires a small effort to calculate the HF-forces after the ground state wave-functions and occupation numbers have been determined.

**Algorithms for ionic motion** In VASP there are three different structural optimizer implemented and a molecular dynamics engine. In the ab-initio MD simulations a Velocity-Verlet algorithm is employed to integrate the equations of motion. At each step the electronic ground state is newly determined and the HF-forces updated. In the structural minimization the available optimizers are: (1) a pseudo-Newton algorithm, (2) a Conjugate Gradient (CG) algorithm, and (3) a damped molecular dynamics algorithm. Due to the Transition State Theory (TST) extension from the Henkelman-Group (Uni-

versity of Texas, Austin) three new optimizers are available: (4) a memory saving pseudo Newton method, Limited-memory Broyden-Fletcher-Goldfarb-Shanno (LM-BFGS), (5) a force based CG, (6) the Fast Inertial Relaxation Engine (FIRE), being a variation of (3) but tends to be faster. Since FIRE seems to be a very good trade-off between speed and stability, it has mainly been used throughout this work and is described now in detail.

**Fast Inertial Relaxation Engine (FIRE)** As stated before FIRE is a variant of the damped molecular dynamics including a reset of the velocities if the system goes uphill. The difference to the quick-min scheme (damped MD with reset of velocities) lies in the mixing of the velocity vectors and the force vectors. Bitzek et al. [46] described this method in a very intuitive way:

*“Consider a blind skier searching for the fastest way to the bottom of a valley in an unknown mountain range described by the potential energy landscape  $E(\vec{x})$  with  $\vec{x} = (x_1, x_2)$ . Assuming that the skier is able to retard and steer we would recommend him to use the following equation of motion*

$$\dot{\vec{v}}(t) = \frac{\vec{F}(t)}{m} - \gamma(t) |\vec{v}(t)| [\hat{v}(t) - \hat{F}(t)], \quad (3.47)$$

*with the mass  $m$ , the velocity  $v = \dot{\vec{x}}$ , the force  $\vec{F} = -\nabla E(\vec{x})$ , and hat denoting a unit vector. We recommend the strategy that the skier introduces acceleration in a direction that is “steeper” than the current direction of motion via the function  $\gamma(t)$  if the power  $P(t) = \vec{F}(t) \cdot \vec{v}(t)$  is positive, and in order to avoid uphill motion he simply stops as soon as the power becomes negative. On the other hand,  $\gamma(t)$  should not be too large, because the current velocities carry information about the reasonable “average” descent direction and energy scale.”[46]*

If initial values for the time step  $\delta t$ , the mixing parameter  $\alpha_{\text{start}} = \gamma \cdot \delta t$ ,  $\vec{x}$  and  $\vec{v} = \vec{0}$  are given, the explicit steps of the algorithm are as follows:

1. Do a MD step using any MD integrator like the Velocity-Verlet algorithm connected to a code delivering the forces in the system. Check for convergence. Obtain  $\vec{x}$ ,  $\vec{F}$  and  $\vec{v}$  in this step.
2. Calculate the power  $P(t) = \vec{F}(t) \cdot \vec{v}(t)$ .
3. Adapt the velocities by mixing in the forces  $\vec{v} \rightarrow (1 - \alpha)\vec{v} + \alpha\vec{F}/|\vec{v}|$ .
4. If  $P > 0$  and  $P$  has not been negative for more than  $N_{\text{min}}$  steps, increase  $\delta t \rightarrow \min(\delta t_{\text{inc}}, \delta t_{\text{max}})$  and decrease  $\alpha \rightarrow \alpha f_{\alpha}$ .
5. If  $P \leq 0$ , decrease  $\delta t \rightarrow \delta t_{\text{dec}}$ , reset all velocities in the system  $\vec{v} \rightarrow \vec{0}$  and reset  $\alpha \rightarrow \alpha_{\text{start}}$ .
6. Return to 1.

This method has in total seven parameters, the initial time step  $\delta t_{\text{start}}$ , the initial mixing parameter  $\alpha_{\text{start}}$ , the delay  $N_{\text{min}}$  before adapting  $\delta t$  and  $\alpha$ , the time step increasing parameter  $f_{\text{inc}}$ , the time step decreasing parameter  $f_{\text{dec}}$ , and the parameter decreasing the mixing  $f_{\alpha}$ . If those are chosen carefully, this method can keep up in speed with complicated schemes like pseudo Newton methods, but is much more stable and requires very little memory to be executed (*“Memory requirements are roughly 3M, 4M, and 14M, for FIRE, CG, and LM-BFGS, respectively, where M is the number of variables”* [46]). In the presentation of the method the authors already gave optimal values for most of these parameters, since they seem to be independent of the system at hand:  $N_{\text{min}} = 5$ ,  $F_{\text{inc}} = 1.1$ ,  $f_{\text{dec}} = 0.5$ ,  $\alpha_{\text{start}} = 0.1$ , and  $f_{\alpha} = 0.99$ .

### 3.2.4. Projector Augmented Wave Method (PAW)

In this method by Blöchl [47] the all-electron (AE) wave-function  $\phi_{\text{AE}}$  is not calculated, but rather a pseudo wave-function  $\phi_{\text{PS}}$ . This is done in a frozen-core approximation, which means that the nucleus near electrons are considered frozen since they are located in full orbitals and do not participate in bonds. This approximation is the basis for all pseudo-potentials but the PAW differs to the other methods by, in principle, providing AE wave-functions. For this purpose a transformation  $\mathcal{T}$  is introduced mapping the pseudo wave-functions  $\phi_{\text{PS}}$  of the valence electrons to the all-electron wave-functions  $\phi_{\text{AE}}$

$$\phi_{\text{AE}} = \mathcal{T}\phi_{\text{PS}}. \quad (3.48)$$

The space is partitioned into nucleus near areas (spherical augmentation regions) and nucleus far areas (interstitials). In the augmentation region the wave-functions are expanded into products of a radial function and spherical harmonics. In the interstitials the wave-functions can be described by plane-waves. The transformation is defined as

$$\mathcal{T} = 1 + \sum_i (|\varphi_i \rangle - |\tilde{\varphi}_i \rangle) \langle p_i|. \quad (3.49)$$

$\varphi_i$  denote the AE partial waves, being the solution of an AE radial Schrödinger equation in the spherical augmentation region.  $\tilde{\varphi}_i$  are the PS partial waves, being the solution of a PS radial Schrödinger equation in the augmentation region.  $p_i$  are the projectors. The index  $i$  refers here to the angular momentum quantum-number  $l$ , the magnetic quantum-number  $m$ , the site index as well as to a reference energy  $\epsilon$  (at those energies the partial waves has been constructed). This transformation can be understood as a subtraction of the wrong pseudo wave-character and adding the correct all electron wave-character in the augmentation region. The character of a wave-function is defined by  $c_i = \langle p_i | \phi_{\text{PS}} \rangle$ . In the interstitial  $\phi_{\text{AE}}$  is equal to  $\phi_{\text{PS}}$ .

Most observables  $\mathcal{O}$  can directly be determined from the pseudo wave-functions. In such cases there are always three contributions:

$$\mathcal{O} = \tilde{\mathcal{O}} + \mathcal{O}^1 - \tilde{\mathcal{O}}^1 \quad (3.50)$$

The first term is the global pseudo contribution, the second one the AE contribution inside of the augmentation region, and last one the PS contribution inside the augmentation region. This is also true for the charge density  $n = \tilde{n} + n^1 - \tilde{n}^1$ . However,  $\phi_{\text{AE}}$  and  $\phi_{\text{PS}}$  do not have the same norm in the augmentation region. Therefore, a compensation charge  $\hat{n}$  is introduced being not spherical and adapting constantly to the environment such that the multi-pole moments are identical to the AE solutions. The electron charge density inside the augmentation region is thus

$$n^1 + Z - \tilde{n}^1 - \hat{n}, \quad (3.51)$$

$Z$  is the charge-density in the frozen core.

It has to be noted that the PAW transformation is in principle exact, but due to numerical reasons approximations has to be done, like the summation of a limited number of bands.

This ends the description of the electronic structure calculations. It has been shown how the electronic ground state of condensed matter systems can be computed efficiently. The energy of the electrolyte structure and the forces on the ions can be determined. In the following chapter the theories and methods, necessary to determine the migration barriers of the oxygen ion transport in the electrolyte is presented.

## 4. Transition States and their determination

### 4.1. Transition State Theory

The Transition State Theory (TST) describes the reaction rates of rare events like elemental chemical reactions (e.g. catalytic reaction of hydrogen and oxygen on the surface of fuel cell electrodes) and diffusion processes in solid states (e.g. oxygen ion diffusion in YSZ). It describes these processes on basis of a quasi-equilibrium between the reactant species and the transition-state species by assuming that the density of the

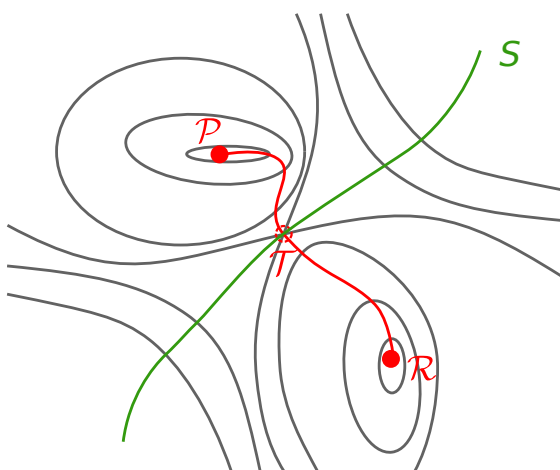


**Figure 4.1.:** Schematic view of the  $3N$  dimensional phase space showing equipotential surfaces (solid grey lines) the Minimum Energy Pathway (MEP) connecting reactant  $\mathcal{R}$  and product  $\mathcal{P}$  configurations in red and the dividing surface  $S$  (green line) crossing the MEP at the transition state  $\mathcal{T}$ .

transition-state species is proportional to the reaction rate  $\Gamma$ . Thus, it deduces the dynamical quantity  $\Gamma$  from a statistical one. Of paramount importance for this procedure is the determination of the dividing surface  $S$ <sup>1</sup> separating the reactant side  $\mathcal{R}$  (initial state) from the product site  $\mathcal{P}$  (final state) (c.f. Fig. 4.1 and 4.2). This hyperplane, or more precisely the energy-minimum of this plane, is typically referred to as the *transition state*  $\mathcal{T}$ . If the system is exactly located at the transition point, it will either return to the reactant state, or move forward to the product state with the probability of  $1/2$  each. The average lifetime of the transition state is very short in comparison to the average lifetime of the product or reactant state but it sensibly determines the character of the system in the time after the residence at  $\mathcal{T}$ . The transition state theory is also called “activated-complex theory”, “absolute-rate theory” or “theory of absolute reaction rates”.

<sup>1</sup> $S$  is typically a  $3N - 1$  dimensional hyperplane, with  $N$  being the number of atoms in the system.

Two central assumptions underly the TST

1. The reactant species is Boltzmann distributed in energy in each degree of freedom and the transition rate  $\Gamma$  is low enough to maintain this distribution (i.e. the atoms in the system are thermalized before they pass  $S$  and will be fully thermalized before they pass  $S$  or another dividing surface leading to another product state again).
2. The system crosses the dividing surface  $S$  only once when going from the reactant to the product state.

The first assumption implies that the species at the transition state are also Boltzmann distributed even if they do not exchange energy with the surroundings when approaching  $\mathcal{T}$ . Due to the high-energy difference between  $\mathcal{R}$  and  $\mathcal{T}$  most trajectories will return to the initial state leading to a low population at the transition state. The few trajectories approaching the dividing surface have momenta and spatial distribution in accordance to a Boltzmann distribution at the temperature of the reactants. One important beauty of this theory is, that to determine the reaction rate no details about the formation of the transition state is necessary. This means that only the initial state and the transition state are required to obtain the diffusion rate of the process at hand. A consequence from the second assumption is a systematic overestimation of the reaction rate  $\Gamma$ . Each trajectory crossing  $S$  is counted as one process, independent whether it is a reactive process or a returning process. As an example, an oxygen ion in YSZ is thermalized at the initial position  $\vec{r}_1$  and jumps to a neighboring vacancy  $\vec{r}_2$  leaving a vacancy behind at  $\vec{r}_1$  and the system thermalizes again in the new state. After the average lifetime  $\tau$ , the ion jumps again if there is a vacancy nearby. If no other ion jumped to  $\vec{r}_1$  the considered oxygen ion can jump back to  $\vec{r}_1$  passing  $S$  again. Obviously this back-jump does not give rise to any diffusion but TST treats these processes as two diffusive jumps. Likewise, the reaction kinetics is not enhanced if a hydrogen molecule dissolves and recombines on the catalyst-surface for many times – only if the product state prevails, it contributes to the kinetic of the reaction.

#### 4.1.1. The diffusion rate

In a system in thermal equilibrium there is a specific number of points on the reactant side of the dividing surface  $S$  (c.f. Fig. 4.1) given by the partition function  $Z_R$  and a specific current of trajectories  $I$  crossing  $S$ . Then the average lifetime  $\tau$  is determined by the quotient of crossing current and the partition function

$$\Gamma = \frac{1}{\tau} = \frac{I}{Z_R}. \quad (4.1)$$

Due to the assumption that reactant species are Boltzmann distributed and, thus, position and momentum of points in phase-space are uniformly distributed over the atomic degrees of freedom, the phase-space point density is given by

$$\rho_R = \rho_0 e^{-\beta E(\vec{r})}, \quad (4.2)$$

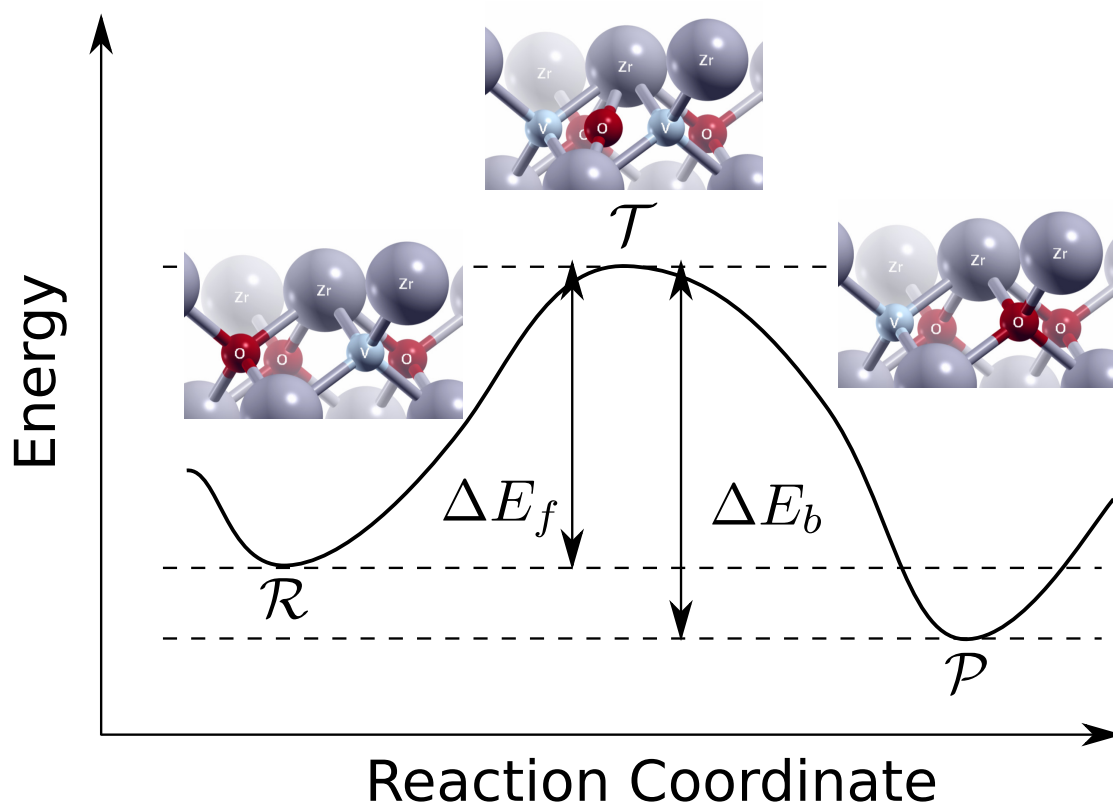


**Figure 4.2.:** Potential energy along the minimum energy pathway (parametrized by the reaction coordinate) from the reaction state  $\mathcal{R}$  over the transition state  $\mathcal{T}$  to the product state  $\mathcal{P}$ . The energy differences  $\Delta E_f$  and  $\Delta E_b$  are the migration barriers respectively for the forward and backward jump. The depicted atomic configurations show a typical jump process of oxygen in zirconia where the  $V$  denotes a vacancy. The pictures correspond to the three states  $\mathcal{R}$ ,  $\mathcal{T}$  and  $\mathcal{P}$ . [48]

where  $\rho_0 = (h^{3N} N!)^{-1}$  is a normalization constant,  $E(\vec{r})$  is the potential at the spatial coordinate  $\vec{r}$  (the potential depends only on the spatial coordinate, not on the momentum) and  $\beta = (k_B T)^{-1}$  is the inverse temperature. The partition function for the reactant site of the dividing surface  $\Omega_R$  is then given by

$$Z_R = \rho_0 \int_{\Omega_R} d^{3N} r e^{-\beta E(\vec{r})}. \quad (4.3)$$

Note that it is only integrated over the volume since  $\rho$  is independent of the momentum.

To calculate the current  $I$  the density of phase-space trajectories on the dividing surface  $S$  with the hyper-momentum  $\vec{V} = \{\sqrt{m_i} \dot{\vec{r}}_i, i = 1 \dots N\}$  within the range  $d\vec{V} = \{\sqrt{m_i} d\dot{\vec{r}}_i, i = 1 \dots N\}$  has to be determined:

$$\rho_S d\vec{V} = \rho_1 e^{-\beta E(\vec{r}_S)} e^{-0.5 \cdot \beta \vec{V}^2} d\vec{V}, \quad (4.4)$$

where  $\vec{r}_S$  is a point on  $S$  and the normalizing constant is

$$\rho_1 = \rho_0 \left( \frac{2\pi}{\beta} \right)^{-N/2}. \quad (4.5)$$

To determine the current of trajectories passing the infinitesimal line-element  $d\vec{S}$  to the other side, the density of these trajectories (Eq. 4.4) has to be multiplied by the line element times the hyper momenta

$$d\vec{I} = d\vec{S} \cdot \int \vec{V} \cdot \rho_S d\vec{V}, \quad \text{with} \quad d\vec{S} \cdot \vec{V} > 0. \quad (4.6)$$

Only those trajectories are included, which have a momentum leading to a crossing from  $\mathcal{R}$  to  $\mathcal{P}$ , i.e.  $d\vec{S} \cdot \vec{V} > 0$ . Assuming  $p_1 = \sqrt{m_1} \cdot \dot{r}_1$  is perpendicular to  $d\vec{S}$ , then the differential current can be determined by

$$d\vec{I} = \rho_1 e^{-\beta E(\vec{r}_S)} d\vec{S} \cdot \int_0^\infty p_1 e^{-0.5 \cdot \beta p_1^2} dp_1 \cdot \prod_{j=2}^{3N} \int_{-\infty}^\infty e^{-0.5 \cdot \beta p_j^2} dp_j. \quad (4.7)$$

The first part is the line integral along  $S$  of the spatial dependent part, the second part is the integration over the momentum coordinate perpendicular to  $d\vec{S}$  and is therefore only done for positive momenta to include only trajectories crossing  $S$ , and the last part is the product over all other momentum coordinates being parallel to  $S$ . The execution of the integration over the momentum space yields

$$d\vec{I} = \rho_0 (2\pi\beta)^{-1/2} e^{-\beta E(\vec{r}_S)} d\vec{S}, \quad (4.8)$$

and the total current crossing  $S$  is given by

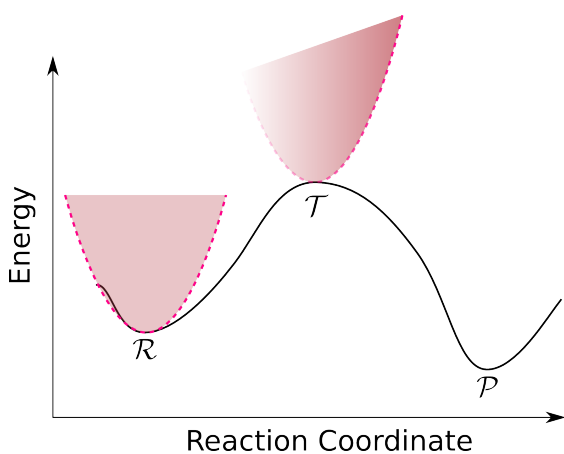
$$I = \int_S d\vec{I} = \rho_0 (2\pi\beta)^{-1/2} \int_S e^{-\beta E(\vec{r}_S)} d\vec{S}. \quad (4.9)$$

The total diffusion rate is given by using Eq. 4.3 and 4.9 in 4.1

$$\Gamma = \frac{1}{\sqrt{2\pi\beta}} \cdot \frac{\int_S e^{-\beta E(\vec{r}_S)} d\vec{S}}{\int_{\Omega_R} r e^{-\beta E(\vec{r})} d^{3N}r}. \quad (4.10)$$

This is a familiar expression: the quotient of two partition functions, where the partition function in the numerator has one dimension less than the one in the denominator.

**Harmonic approximation** The movement of the ions near a minimum can be described by  $3N$  independent harmonic oscillators, due to the equipartition theorem in the thermal equilibrium. Near the initial state  $\mathcal{R}$  this is a good approximation and the potential can be expanded in a Taylor series (cf. Fig. 4.3)



$$E \approx E_{\mathcal{R}} + \sum_{i=1}^{3N} \frac{1}{2} (2\pi\nu_{\mathcal{R}|i})^2 q_{\mathcal{R}|i}^2 \quad (4.11)$$

with the normal coordinates  $q_{\mathcal{R}|i}$ , the vibrational frequencies  $\nu_{\mathcal{R}|i}$  at point  $\mathcal{R}$ , and the potential at the minimum  $E_{\mathcal{R}}$ . For the numerator in Eq. 4.10 it can be assumed that most trajectories cross  $S$  at  $\mathcal{T}$  since the energy is lowest at this point in  $S$ . The potential near  $\mathcal{T}$  in  $S$  can also be approximated harmonically, since  $\mathcal{T}$  is a minimum in all but one coordinate. The potential at  $\mathcal{T}$  is given by

$$E \approx E_{\mathcal{T}} + \sum_{j=1}^{3N-1} \frac{1}{2} (2\pi\nu_{\mathcal{T}|j})^2 q_{\mathcal{T}|j}^2 \quad (4.12)$$

with the normal coordinates  $q_{\mathcal{T}|i}$ , the vibrational frequencies  $\nu_{\mathcal{T}|i}$  at point  $\mathcal{T}$ , and the potential at the saddle point  $E_{\mathcal{T}}$ . The

**Figure 4.3.:** Harmonic approximation of the potential around  $\mathcal{R}$  and  $\mathcal{T}$ . At the initial position the expansion is done in all  $3N$  directions, while at the transition state the expansion is executed in all  $3N-1$  directions of  $S$  (i.e. not into the direction of the MEP, in which the frequencies are imaginary since  $\mathcal{T}$  is a maximum in this dimension)

sum goes only over the coordinates in  $S$ . Obviously a harmonic approximation in the connection of  $\mathcal{R}$  and  $\mathcal{T}$  is not applicable, but since the TST does not need to describe this domain of the phase space correctly it does not matter when looking for diffusion rates. These approximations yield changed partition functions in Eq. 4.10 being

$$\prod_{i=1}^{3N} \frac{1}{2\pi\nu_{\mathcal{R}|i} \sqrt{2\pi\beta}} e^{-\beta E_{\mathcal{R}}}, \quad (4.13)$$

and

$$\prod_{j=1}^{3N-1} \frac{1}{2\pi\nu_{\mathcal{T}|j}\sqrt{2\pi\beta}} e^{-\beta E_{\mathcal{T}}}. \quad (4.14)$$

Finally, the diffusion rate is expressed by

$$\Gamma = \left( \frac{\prod_{i=1}^{3N} \nu_{\mathcal{R}|i}}{\prod_{j=1}^{3N-1} \nu_{\mathcal{T}|j}} \right) e^{-\beta(E_{\mathcal{T}}-E_{\mathcal{R}})} = \nu_{\text{v}} \cdot e^{-\beta\Delta E}, \quad (4.15)$$

with the Vineyard coefficient

$$\nu_{\text{v}} = \frac{\prod_{i=1}^{3N} \nu_{\mathcal{R}|i}}{\prod_{j=1}^{3N-1} \nu_{\mathcal{T}|j}}, \quad (4.16)$$

and the energy barrier

$$\Delta E = E_{\mathcal{T}} - E_{\mathcal{R}}. \quad (4.17)$$

The result in Eq. 4.15 is qualitatively the same as the Arrhenius equation with a prescription how to calculate the frequency pre-exponential factor. It is obvious now which quantities are important when determining the diffusion rate. Although it is possible to determine the Vineyard coefficient by calculation of the normal-frequencies at  $\mathcal{R}$  and  $\mathcal{T}$ , in many cases it can be assumed to have a fixed value of about 5THz. This is the order of magnitude in which the frequencies of vibrations in solid states can be found. Additionally, the diffusion rate depends only linearly on this quantity, and an accurate determination of the energy barrier  $\Delta E$  is much more important. The initial configuration can typically be determined without big problems. The determination of the transition state is, however, much more demanding since it is a saddle point problem. One approach to find such a saddle point in a given phase space is the Nudged Elastic Band (NEB) method described in the last section of the chapter. In the following chapter, the ionic motion is described using the TST.

## 4.2. Ionic Conductivity

### 4.2.1. Crystal defects

In a perfect lattice of a solid-state body no net ionic movement is possible. When all atoms or ions are located at their lattice sites, there are only thermal vibrations around the ground state position possible. In this case the Mean Squared Displacement (MSD)

$$\langle r^2 \rangle = \langle |\vec{r} - \vec{r}_0|^2 \rangle \quad (4.18)$$

is finite – due to vibrations – but does not increase with time. Only when there are defects in the lattice, there is a possibility for the ions to move through the lattice. There are various types of defects possible in condensed matter, which can be distinguished by their dimensionality:

- 0d: Point defects, like vacancies, impurities, Frenkel defects, Schottky defects etc. are defects being limited to one particle or a pair of particles
- 1d: line defects, like edge dislocations or screw dislocations are one dimensional defects including a few to many ions along a, possibly curved, line through the lattice
- 2d: plane defects, like grain boundaries or stack faults
- 3d: bulk defects, like voids or impurity clusters

The mobility of defects decrease with the number of lattice sites they consist of. Thus, the mobility is highest for a single point defect indicating that only the zero dimensional defects are relevant for the ionic conduction. This, however, is only partly true since the mobility of point defects along extended defect, like grain boundaries, could be higher than through the bulk. Nevertheless, the existence of point defects in a lattice is the requirement for any ionic movement. Typical zero dimensional defect are:

- Frenkel defects: In some crystals there are local minima in the potential energy surface, even if the crystal is perfect. Ions can jump to those interstitial positions from neighboring lattice sites and stay there for a specific time. The interstitial positions are energetically higher than the lattice sites, but are metastable and are populated at finite temperatures. The number  $n_F$  of these defects is given by a Boltzmann distribution

$$n_F \propto e^{-\frac{E_F}{k_B T}} \quad (4.19)$$

with  $E_F$  being the formation energy of a Frenkel defect. In addition to the interstitial, a vacancy is generated with each Frenkel defect further contributing to the ionic mobility.

- Schottky defects: Ions near to the surface of the crystal can leave the lattice. Due to the charge neutrality this happens pair-wise leaving two vacancies behind, which can move freely through the crystal. Schottky defect pairs are also thermally activated, leading to a Boltzmann distributed number  $n_S$  of Schottky vacancies in the lattice

$$n_S \propto e^{-\frac{E_{SP}}{2k_B T}}$$

with  $E_{SP}$  being the formation energy of a Schottky pair.

- Doping induced defects: The number of vacancies can be increased by selectively doping the crystal. In zirconium oxide this can be done by doping with yttrium oxide. These vacancies are part of the lattice and exist at all temperatures.

In zirconia the lattice is too dense leaving no space for interstitials making Frenkel defects impossible. Furthermore, the formation energy of thermally induced Schottky pairs  $E_{SP}$  is too high to contribute to the conductivity in the temperature domain of SOFC applications. Leaving only the oxygen vacancies induced by yttrium doping contributing to the conductivity.

### 4.2.2. Phenomenological description of the ionic conductivity

As mentioned before, in zirconium oxide only doping induced vacancies are relevant for the conductivity. Thus, the number of vacancies (charge carriers) is only changed by the dopant concentration but not by temperature. To jump from one crystal site to an empty one, the oxygen ion needs to overcome a potential wall. The energy needed to change the crystal site is called the migration barrier  $\Delta E$ . This barrier depends sensibly on the environment of the vacancy. Nearby vacancies or dopant ions can affect the energy at the initial position of the vacancy and the energy at the barrier position. More unlocalized effects like external pressure can also affect the height of the barrier. As described by the transition state theory, the diffusion rate depends exponentially on this barrier height (cf. Eq. 4.15). The MSD increases linearly with time (asymptotic behavior for  $t \rightarrow \infty$ ) and relates with the diffusion rate by the Einstein relation

$$\langle r^2 \rangle (t) = 2 \cdot d \cdot t \cdot D \quad (4.20)$$

where  $d$  denotes the dimensionality of the observed diffusion process. Using the Nernst-Einstein relation

$$\frac{\mu}{D} = q \cdot \beta \quad (4.21)$$

with the mobility of oxygen ions  $\mu$  and the charge of the ions  $q = -2e$ , the conductivity<sup>2</sup>

$$\varsigma = \mu \cdot q \cdot n \quad (4.22)$$

of the oxygen ionic conductor can be determined, where  $n$  denotes the charge carrier density. The connection of conductivity and diffusion rate is thus

$$\varsigma = 4e^2 \cdot n \cdot \beta \cdot D \quad (4.23)$$

If the MSD is known, Eq. 4.22 becomes

$$\varsigma = 4e^2 \cdot n \cdot \beta \cdot \frac{1}{2 \cdot d} \cdot \frac{\langle r^2 \rangle (t)}{t}. \quad (4.24)$$

Using the results of the TST, the expression for  $\varsigma$  is

$$\varsigma = 4e^2 \cdot n \cdot \beta \cdot \nu_0 \cdot d_{\text{eff}}^2 \cdot e^{-\beta \cdot \Delta E}. \quad (4.25)$$

The hopping rate  $\Gamma$  from the TST is related to the diffusion rate  $D$  by a geometric factor  $d_{\text{eff}}^2$  being the square of the effective jump distance. The conductivity is a quantity mainly for comparison to experiments, since current measurements are relatively easy to execute and by using the Ohmic law

$$j = \varsigma \cdot E \quad (4.26)$$

---

<sup>2</sup>In this thesis the lattice strain of a crystal is denoted by  $\sigma$ , therefore, it will be deviated from the typical convention to represent the electrical conductivity by  $\sigma$ , and the letter  $\varsigma$  will be used for the conductivity.

the conductivity can be obtained. However, in the fuel cell the electric field due to the cell voltage hampers the required ionic diffusion. Due to the electric field  $E$  there is a current of electric charges (carried by oxygen ions)  $j$  from the anode to the cathode, and due to a concentration gradient  $\nabla c$  of oxygen ions there is a diffusive flux  $J$  from the cathode to the anode described by the first Fick's law (stationary concentration gradient)

$$J = -D \cdot \nabla c. \quad (4.27)$$

This makes clear that in fact the diffusion rate  $D$  is the more important quantity, but as seen by 4.23 these two quantities are directly related.

By investigating Eq. 4.25 it becomes clear to which quantities the conductivity is sensitive and which are less important. The charge density  $n$  is, as stated before, only given by the doping, is independent of the temperature and has an upper bound. The Vineyard coefficient  $\nu_0$  and the effective jump distance  $d_{\text{eff}}$  are structure sensitive and temperature independent. The Vineyard coefficient does not change strongly and is typically approximated with  $\nu_0 = 5 \cdot 10^{12}$  Hz. The effective jump distance is given by the lattice structure and cannot change too much as well. The temperature being an external parameter enters both reciprocal and exponential leading to an exponential increase of the conductivity with it. Last, the migration barrier  $\Delta E$  is also structure sensitive and temperature independent, but enters the expression exponentially. Although  $\Delta E$  cannot change too strongly as well, the exponential dependence makes it a crucial quantity when trying to improve the performance of an electrolyte.

### 4.3. Determination of the Transition State

As described in the first section of this chapter, it is necessary to know the energy barrier of a diffusion pathway to describe the transition rate of the rare event. In this section the NEB method will be described, which makes it possible to obtain the whole MEP in a discrete way. An advanced version of this method, called climbing image nudged elastic band (cINEB), can determine the exact transition state similarly to the relaxation of an atomic system.

#### 4.3.1. Finding the minimum energy pathway

If both the initial and the final state of a system is known, the first and easiest idea would be to connect both phase space points by an arbitrary line. However, as can be seen in Fig 4.4 the first trail pathway leads to a very high barrier and the maximum of the path is in no way a saddle point. To obtain the saddle point, the following scheme can be used:

1. Connect initial and final state with a direct line.
2. Calculate energies and forces at each position of this line.
3. Neglect the forces along the band  $\vec{F}_{\parallel}$ , as they do not change the shape of the band.

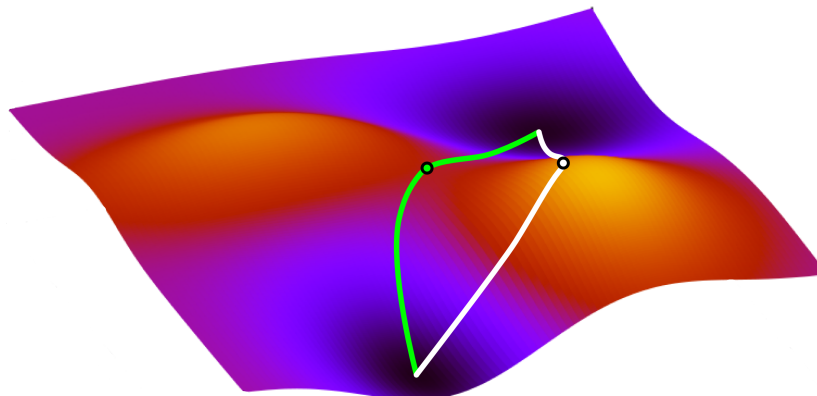


**Figure 4.4.:** This example of a simple potential surface (2D superposition of Gaussians) shows an initial guess for the MEP (white) and the relaxed MEP (green). The dots indicate the maximum of each band. It is obvious, that the white dot is located on a potential slope transverse to the band, while the green dot is located in a saddle point.

4. If the forces normal to the band  $\vec{F}_\perp$  converge to zero the MEP is found, otherwise move the band infinitesimal along  $\vec{F}_\perp$  down the hill and return to point 2.

When all normal forces vanish, each point of the band is situated in a minimum regarding all but one dimension, which is the direction of the band. This, in turn, means that the maximum of the band is a saddle point and therefore a transition state.

For an easy example as given in Fig. 4.4 being a two dimensional superposition of Gaussians, this scheme can be applied in this direct way. However, computational costs restrict the application of this scheme to ab-initio calculations. Still, it is possible to use a modified version of this scheme to calculate the MEP of a high-dimensional atomistic system. This method is the Nudged Elastic Band Method and will be described in the following.

### 4.3.2. Nudged Elastic Band Method

The previously discussed band is discretized at a finite number of phase space points, at so called images (e.g. 5). These images of the system are connected by straight lines starting from a first image  $i = 1$  up to the last image  $i = N$  using a linear interpolation

$$\vec{R}_i = \vec{R}_1 + \xi_i (\vec{R}_N - \vec{R}_1), \quad (4.28)$$

$\vec{R}_i$  being the atomic positions of the image  $i$  and  $\xi_i < 1$  being a linear factor leading to the configuration of the image  $i$ . If previous knowledge about the transition state is available, it could help strongly to find the correct (lowest) transition state, since it is not possible to determine whether the saddle point obtained from this method is the lowest one. As in any minimization process intuition and previous knowledge can mislead when the energetically lowest saddle point has an unforeseeable shape. The band constructed

in this way moves through the phase space, while three kinds of forces act [15] upon each image ( $1 < i < N$ ) at position  $\vec{R}_i$

$$\begin{aligned}\vec{F}_i &= \vec{F}_{i1} + \vec{F}_{i2} + \vec{F}_{i3} \\ &= -\nabla E(\vec{R}_i) + \hat{\tau}_i \hat{\tau}_i \cdot \nabla E(\vec{R}_i) + \hat{\tau}_i \alpha_i.\end{aligned}\quad (4.29)$$

$E_i$  is the energy of image  $i$  and  $\vec{F}_{i1}$  is the force acting on each image due to the local potential.  $\vec{F}_{i1}$  is also used in the *drag method* [17],  $\vec{F}_{i2}$  and  $\vec{F}_{i3}$  are, however, special to the NEB method and are quite important.  $\vec{F}_{i2}$  cancels the force  $\vec{F}_{i1}$  along the direction of the normalized ‘tangent’ vector

$$\hat{\tau}_i = \frac{\vec{\tau}_i}{|\vec{\tau}_i|} \quad (4.30)$$

of the band and replaces it by  $\vec{F}_{i3}$ , an artificial spring force in the same direction, obtained from

$$\alpha_i = \kappa \left( \left| \vec{R}_{i+1} - \vec{R}_i \right| - \left| \vec{R}_i - \vec{R}_{i-1} \right| \right), \quad (4.31)$$

with the spring constant  $\kappa$ . One way to obtain the local tangent of the band  $\vec{\tau}_i$  is from requiring that the additional terms  $\vec{F}_{i2}$  and  $\vec{F}_{i3}$  must not change the length of the band, yielding [16]

$$\vec{\tau}_i = \frac{\vec{R}_i - \vec{R}_{i-1}}{\left| \vec{R}_i - \vec{R}_{i-1} \right|} + \frac{\vec{R}_{i+1} - \vec{R}_i}{\left| \vec{R}_{i+1} - \vec{R}_i \right|}. \quad (4.32)$$

Another way [16] to define the local tangent leading to a more stable convergence of the band when searching for a saddle point is to choose the tangent at image  $i$  as the connecting vector to the neighboring image higher in energy. Then the tangent vector at an image  $i$  is defined as

$$\vec{\tau}_i = \begin{cases} \vec{\tau}_i^+ & \text{if } E_{i+1} > E_i > E_{i-1} \\ \vec{\tau}_i^- & \text{if } E_{i+1} < E_i < E_{i-1} \end{cases} \quad (4.33)$$

with

$$\vec{\tau}_i^+ = \vec{R}_{i+1} - \vec{R}_i \quad \text{and} \quad \vec{\tau}_i^- = \vec{R}_i - \vec{R}_{i-1}. \quad (4.34)$$

If the image  $i$  is located near to an extremum, i.e. images  $(i-1)$  and  $(i+1)$  are both higher or both lower in energy, the tangent is a weighted average according to:

$$\vec{\tau}_i = \begin{cases} \vec{\tau}_i^+ \Delta E_i^{\max} + \vec{\tau}_i^- \Delta E_i^{\min} & \text{if } E_{i+1} > E_{i-1} \\ \vec{\tau}_i^+ \Delta E_i^{\min} + \vec{\tau}_i^- \Delta E_i^{\max} & \text{if } E_{i+1} < E_{i-1} \end{cases} \quad (4.35)$$

with

$$\begin{aligned}\Delta E_i^{\max} &= \max(|E_{i+1} - E_i|, |E_{i-1} - E_i|) \\ \Delta E_i^{\min} &= \min(|E_{i+1} - E_i|, |E_{i-1} - E_i|)\end{aligned} \quad (4.36)$$

From Eq. 4.31 results that the spring forces only depend on the distance between two successive images. This distance  $\delta s_i$  is defined as the sum over all atomic displacements from image  $i$  to  $i + 1$

$$\delta s_i = \sum_{n=1}^{N_{\text{atom}}} |\vec{r}_{n,i} - \vec{r}_{n,i+1}|,$$

with the atomic coordinates  $\vec{r}$ . The sum over all distances  $\delta s_i$  determines the reaction coordinate in the NEB method

$$s = \beta \sum_{i=1}^{N-1} \delta s_i, \quad \text{with} \quad \beta \in [0, 1]$$

parametrizing the  $3N_{\text{atom}}$  dimensional phase space along the one dimensional band.

If the spring-constant  $\kappa$  is negative (a typical value is  $\kappa = -5 \text{ eV}/\text{\AA}^2$ ) the images are nudged by each other and will keep an equal distance along the band, while still being able to relax perpendicular to the local tangent following the real potential. In this way each image moves down the potential while being pushed by adjacent images to keep an equal distance. Then, the energies and forces are computed again, the new tangent vectors of the band are determined, and the images moved according to Eq. 4.29. This is repeated until the normal forces are smaller than a given convergence criterion. At the end of the relaxation the MEP is found, which includes the transition state as the maximum. The beauty of this scheme is that a saddle-point search is transformed into a minimum search for which many efficient solvers are known. However, this simplification is paid by increasing the size of the system by a factor equal to the number of images in the band. For simple pathways three images might suffice to sample the MEP satisfactorily. Though, for complicated systems<sup>3</sup> with many degrees of freedom up to twenty images might be necessary to describe the MEP sufficiently.

**Climbing image nudged elastic band (ci-NEB)** A major drawback of the NEB method is that in the general case the transition state itself is not covered by an image. Therefore, it was necessary to obtain the barrier energy by interpolating between the two highest images (e.g. by using cubic splines), by using a higher number of images or by using the DIMER Method to climb from the highest image to the saddle point. However, interpolations are very inaccurate, since the potential energy surface around the transition state can have different curvatures than at the nearest images. Increasing the number of images to obtain a more accurate MEP is not always desirable for the increased numerical cost, especially when only the barrier height itself is searched and the exact shape of the MEP is unimportant (which is basically always when the diffusion rate is sought). The DIMER<sup>4</sup> method is a saddle point search algorithm, which does

<sup>3</sup>E.g. the rotation of a molecule over a surface.

<sup>4</sup>In the DIMER method the initial state is reproduced and displaced by a vector of small magnitude. These two images can be considered as a dimer, which can be rotated in the  $3N_{\text{atom}}$  dimensional phase space until the lowest mode is found. This is possibly the beginning of a MEP and following it will hopefully lead to the saddle point.

not require the knowledge of the final state. Although it can determine the exact saddle point, it is slow and too demanding for this job. An efficient alternative can be obtained from the NEB itself. In the CI-NEB the highest image is not exposed to the artificial spring force, but to the real negative tangential forces:

$$\vec{F}_{i_{\max}} = -\nabla E(\vec{R}_i) + 2 \cdot \hat{\tau}_i \hat{\tau}_i \cdot \nabla E(\vec{R}_i) \quad (4.37)$$

In this way the highest image will relax down the normal forces and up the tangential ones. Obviously, if  $\vec{F}_{\perp}$  is minimum and  $\vec{F}_{\parallel}$  is maximum, a saddle point is reached.

**Concluding remarks** Now all theoretical and methodological requirements are obtained to calculate the diffusion in electrolyte materials like YSZ, to determine the response of the system to changes of external parameters like strain. To determine the diffusivity of the system, the diffusion rate needs to be known, which is given by Eq. 4.15. This again requires the knowledge of the lowest saddle-point between initial and final state, the transition state. This can be determined by the NEB method described in this section. The calculation of the transition state on basis of NEB itself needs an underlying framework describing the energies and forces in atomic systems. The framework of choice in this thesis is the highly accurate DFT using the efficient plane-wave code VASP. This has been described in detail in chapter 3. In the next chapter the nudged elastic band method is harnessed with an intelligent placement of images to form a new global optimization scheme, the MsNEB, being complementary to simulated annealing. In the chapters following thereafter, the assortment of methods, theories and approximations, presented until here, are used to describe, understand and predict the movement of oxygen ions in SOFC electrolyte materials.



## 5. A new NEB based optimization scheme

While using the NEB scheme extensively for finding the migration barriers in the SOFC electrolyte materials, it was mandatory to gain a fundamental understanding of the principles behind this method. To obtain such insights, the NEB method has been applied to many different systems. Based on the comprehension acquired in this process an idea was born to modify the NEB method to fulfill a different purpose. Due to the peculiar characteristics of the NEB method, it seemed to be possible to alter it to overcome local minima. The artificial spring-forces being an essential part in NEB enables the images of the band to move freely along the band, unhindered by the real potential. If it would be possible to steer this mechanism accordingly, it seemed to be feasible to escape local minima and let the band itself relax towards a global minimum. The Minimum search Nudged Elastic Band (MsNEB) was born [49]. In fact, it turns out that this method was able to detect an hitherto unknown most stable isomer in the test-system  $P_8$ , which already amazingly shows the power of this method.

This is a immense broadening of the understanding of the NEB methods, but at the same time it contributes significantly to the field of global optimization, which has a very wide field of application. Finding new stable configurations is important for the fundamental understanding of material properties, for developing new stable materials with novel properties and, in general, whenever optimization is necessary, e.g. in engineering and economics. However, the optimization problem can become very complex due to many local minima in a high dimensional phase space. Simple minimum search procedures often fail, and sophisticated optimization schemes are required. Many of these rest on *simulated annealing* [18] and the *genetic algorithm* [19].

In simulated annealing, the annealing process of condensed matter is imitated to find stable configurations. This is achieved by introducing a temperature parameter  $T$  controlling *thermal fluctuations*. At high  $T$  the fluctuations are large and it is possible to overcome large energy barriers between local minima. By decreasing  $T$  the fluctuations are diminished and lead to a more stable minimum than can be found with simple search methods. The extent of application possibilities are immense for simulated annealing. Some of many applications are: finding stable isomers of phosphorus clusters [50], designing heterogeneous catalytic reactors [51], three dimensional face recognition [52], the optimization of electric discharge machining [53], the inverse calculation of experimental scattering data [54] or a search algorithm for structures and substructures of proteins in a database [55]. A similar method is the simulated quenching, which has been applied for example to the design of optical elements [56].

In the genetic algorithm a set (population) of different configurations is considered. In addition to small random variations of the configurations (mutations), the properties of the most successful states are melded to find even more stable ones, thus imitating

inheritance in genetics. Also the genetic algorithm has been used for many different applications: finding of Sb clusters [57], finding stable alloys based on DFT out of 19016 possible combinations [58] or finding crystal structures in constrained systems [59]. Although simulated annealing and the genetic algorithm address the problem of local minima, there can be no guarantee that the configuration obtained by these methods is the global minimum. Therefore, there is a need for other, complementary methods. In fact, it turns out, that MsNEB is not just another optimization scheme among many, it is actually such a complementary method. The MsNEB differs on the way it escapes local minima, which is the heart of any scheme aiming at global optimization leading to a fundamental difference to the energy based schemes.

In the first section of this chapter the emphasize lies on the features of the NEB method that make it useful for optimization purposes i.e. avoiding irrelevant local minima. In section 5.2 the algorithm of the MsNEB is presented and in section 5.3 it is shown that (i) the new band based optimizer reproduces well-known minima of the  $P_4$  cluster [60], (ii) by applying it to the  $P_8$  cluster [61, 62, 63] the method finds a new most stable isomer. The new method is also applied to find the most stable configuration of chemically similar compounds in the same main group i.e.  $As_n$ ,  $Sb_n$ ,  $Bi_n$ , ( $n = 4, 8$ ). As a by-product, an upper bound for the energy barriers between these configurations is obtained. All calculations are done in the framework of DFT (cf. Chap. 3).

## 5.1. NEB in the neighborhood of a minimum

Any scheme searching for global minima can succeed only if it (i) can overcome local minima, (ii) can find the low-lying minima. It is shown now that appropriate use of the NEB method can do both, although it was not developed for this purpose. Based on the introduction of the NEB method in section 4.3, the optimizing character of this method is now shown. As pointed out before, the band moves through the phase space, while the three kinds of forces given in Eq. 4.29 act upon each image. The tangent, determining the direction of the artificial spring-forces, is for this purpose best described by the requirement that  $\vec{F}_{i2}$  and  $\vec{F}_{i3}$  must not change the length of the band (cf. Eq. 4.32). The “improved” tangent given by Eq. 4.33 is optimized for finding a transition state, but for the purpose of finding minima it is disadvantageous. This construction of  $\mathbf{F}_i$  has distinct consequences for images within the range of a minimum, which depend on the choice of the force constant  $k$  and the distance between two successive images. Using the total length of the band  $L_{\text{Band}}$ , the average distance  $S$  is obtained by:

$$S = \frac{L_{\text{Band}}}{N - 1}. \quad (5.1)$$

Let us first turn to the parameter  $k$ . As shown in Fig. 5.1 an image  $i$  can pass an equipotential surface around an attracting minimum only if

$$|\vec{F}_{i1}| \cdot \sin^2(\gamma) < |\vec{F}_{i3}| \cdot \cos(\gamma). \quad (5.2)$$

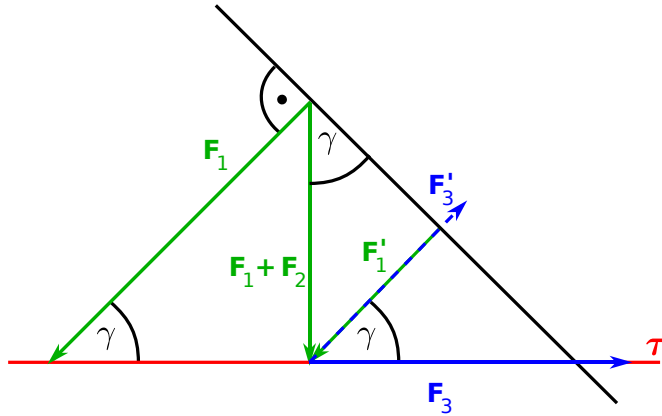


**Figure 5.1.:** Passing of an equipotential surface: The force  $\vec{F}_1$  is perpendicular to the equipotential surface (black).  $\gamma$  is the angle between  $\vec{F}_1$  and the tangent  $\vec{\tau}$ .  $\vec{F}'_1$  is the resulting force component pulling the image towards the minimum.  $\vec{F}'_3$  is the component of the artificial spring force pushing the image out of the attractor. If  $|\vec{F}'_1| < |\vec{F}'_3|$ , the image will pass the equipotential surface, i.e. depart from the minimum.

Here  $\gamma$  is the angle between the normal of the equipotential surface and the tangent vector  $\hat{\tau}_i$ .  $\gamma$  can assume any value in the interval  $] -90^\circ, +90^\circ[$ , and  $\sin^2(\gamma) < 0.1$  for  $|\gamma| \lesssim 20^\circ$ . If  $k$  is not small, the probability of a trapped image escaping from a local minimum is not small. On the other hand, the probability vanishes for  $k \rightarrow 0$ , and thus the band cannot escape the range of attraction  $R_a$  of the minimum.

If  $k$  is not too small, the motion of the images can easily be understood, since the distances between all images are approximately equal and given by  $S$ . Fig. 5.2 shows a snapshot where image  $i$  is in the range of attraction  $R_a$  of a local minimum. If the image  $(i+2)$  is nudged to the right, for example, all the images  $m < (i+2)$  will move along their tangent vectors  $\hat{\tau}_m$ , and the image  $i$  can escape easily from the local minimum. At the same time, however, image  $(i-1)$  has moved closer to the local minimum. If  $S \gtrsim R_a$ , image  $(i-1)$  will not enter the range of attraction, and the band has escaped from the local minimum. For  $S \lesssim R_a$ , image  $(i-1)$  has a high probability of entering the range of attraction. The net result is that the image  $i$  has escaped from the local minimum, whereas the band has not.

As  $S$  decreases, the probability increases that the band, once in the range of a local minimum, does not escape. For  $S \rightarrow 0$ , this is true for all  $k$ , as the following argument shows: For  $S \rightarrow 0$  the band becomes a smooth curve, the vectors  $\hat{\tau}_i$  become the genuine tangent vectors of the curve, and  $\vec{F}_{i3}$  cannot change the shape of the band. If the band now enters the range of attraction of a local minimum,  $\vec{F}_{i1} + \vec{F}_{i2}$ , being orthogonal to the curve, will pull the band in the direction of the minimum (Fig. 5.3). The only effect of  $\vec{F}_{i3}$  is to move images along the band, so that some images may escape from the local minimum. But this is irrelevant because the band remains captured.

To summarize: The escape of the band from a minimum depends on (i) the value of the

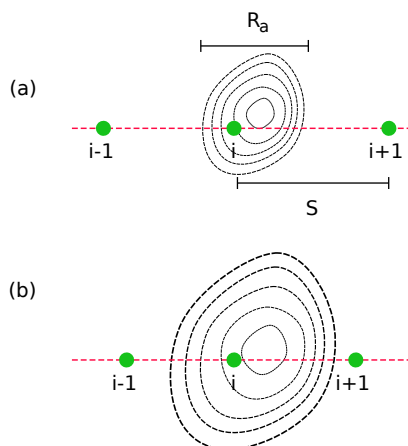


**Figure 5.2.:** Sketch of the band in the neighborhood of a minimum. In (a)  $S > R_a$ , in (b)  $S < R_a$ . In both cases image  $i$  can escape from the range of attraction if e.g. image  $(i+2)$  nudges sufficiently to the right. In (a) the band will then escape from the minimum, in (b) it will not.

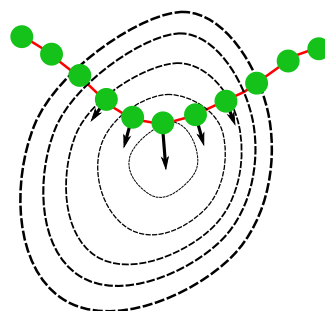


**Figure 5.3.:** If  $S \rightarrow 0$ ,  $\vec{F}_{i3}$  can only move the images along the band but cannot change its shape, and the band cannot escape from the minimum.

parameter  $k$ , (ii) the value of the length  $S$ , (iii) the nudging process. The corresponding algorithm will now be described.

## 5.2. The MsNEB Algorithm

The NEB method, introduced to change saddle-point problems into minimum-finding problems, is used here to find the stable configurations of molecules, which requires modification. In the original method, the first and the last image of the band are usually relaxed to ensure that the bottom of the potential well is reached. In this case, however, it is not necessary to start or end in a minimum, and the first and last image of the band can be chosen (i) as random configurations (ii) from known stable or metastable configurations of this or related compounds (iii) exploiting knowledge from previous calculations. However, the first and the last image of the band should be distinctly different. This can be achieved by choosing at least one configuration randomly, or by starting with two states with quite different symmetries, as in a molecule. Known configurations can be included as the first or last image of the band. After specifying these images the band is created by  $(N-2)$  additional images.  $N$  determines  $S$  (see Eq. 5.1), the mean distance between the images, and hence the minima that can be overcome, because their range of attraction  $R_a \lesssim S$ . Assuming that  $R_a$  of the stable state in question is of the same order of magnitude as that of known stable states of this or similar systems, one can choose  $N$  correspondingly or start with a small value.

The motion of the band occurs in cycles, in each of which the band is first relaxed as in a typical NEB for  $N_I$  ionic relaxation steps following Eq. 4.29. Eq. 4.31 implies that the images do not relax independently, but ‘nudge’ each other and begin to scan an area around the initial band. Nudging is crucial in this method and is implemented by moving, removing or adding images after the  $N_I$  relaxation steps: Either the image with highest energy is removed and a new one is set to the position with lowest energy in the band (even cycles), or a new image is set at the lowest point of the band, increasing the number of images in the band (odd cycles). A different situation arises if neighboring images relax to degenerate minima that transform into each other by translations or rotations of the system. If there are images located in such a minimum, they usually cannot escape and even attract more images into it, which makes them inactive for the optimization process. All but one of these degenerate images are discarded, and a new image is generated at the position of the band with lowest energy. These manipulations (adding, moving and removing images) end a cycle and may lead to a new  $N$ . In Fig. 5.4 the algorithm is summarized in a floating chart.

The nudging dynamics is retained from cycle to cycle, enabling the images to overcome local minima along the tangential direction  $\hat{\tau}_i$  independent of the barrier height, and to relax perpendicular to  $\hat{\tau}_i$  toward the global minimum (cf. Fig. 5.2).

$S$  is by no means a constant in an optimization run, even for constant  $N$ . In fact, due to the relaxation of the band perpendicular to  $\hat{\tau}_i$  the length of the band varies and fluctuates. At the beginning of an optimization run,  $S$  can increase even if the number of images increases. This effect is certain to occur if a straight line connects the first with the last image at the beginning of an optimization run, and relaxation can only prolong the band. When the band approaches more relaxed states, the addition of images will reduce  $S$ , but fluctuations of  $S$  remain part of the nudging process. This does not matter, at least as long as  $S$  does not change by an order of magnitude. Moreover, the reduction of  $S$  below a threshold  $S_{\text{conv}}$  appears to be unnecessary as long as one can estimate  $R_a$  of the stable state.

An alternative way to reduce the chance to escape local minima is given by decreasing  $k$  throughout the optimization process (Eq. 5.2). Inspired by simulated annealing, this reduction could follow an exponential law, e.g. for the  $k$  value of the  $j^{\text{th}}$  cycle

$$k_j = k_{\text{init}} \cdot e^{-A \cdot (j-1)} \quad (5.3)$$

with a scaling factor  $A$ . In this way  $k$  goes to zero as  $j$  increases. Such procedures are necessary if there are limits on the number of images. It is important to point out that the reduction of  $k$  can be achieved in different manners and the choice of exponential decay implies by no means that  $k$  corresponds to the temperature parameter of simulated annealing. In systems of modest size, it was more efficient to increase the numbers of images. It may be desirable to stabilize or destabilize parts of the band, and this can be achieved by locally decreasing or increasing the  $k$  values.

In simulated annealing the probability that a point in phase space escapes from a minimum depends on its depth and the temperature  $T$ . In the MsNEB scheme the probability for the band to escape from a minimum depends on its range of attraction

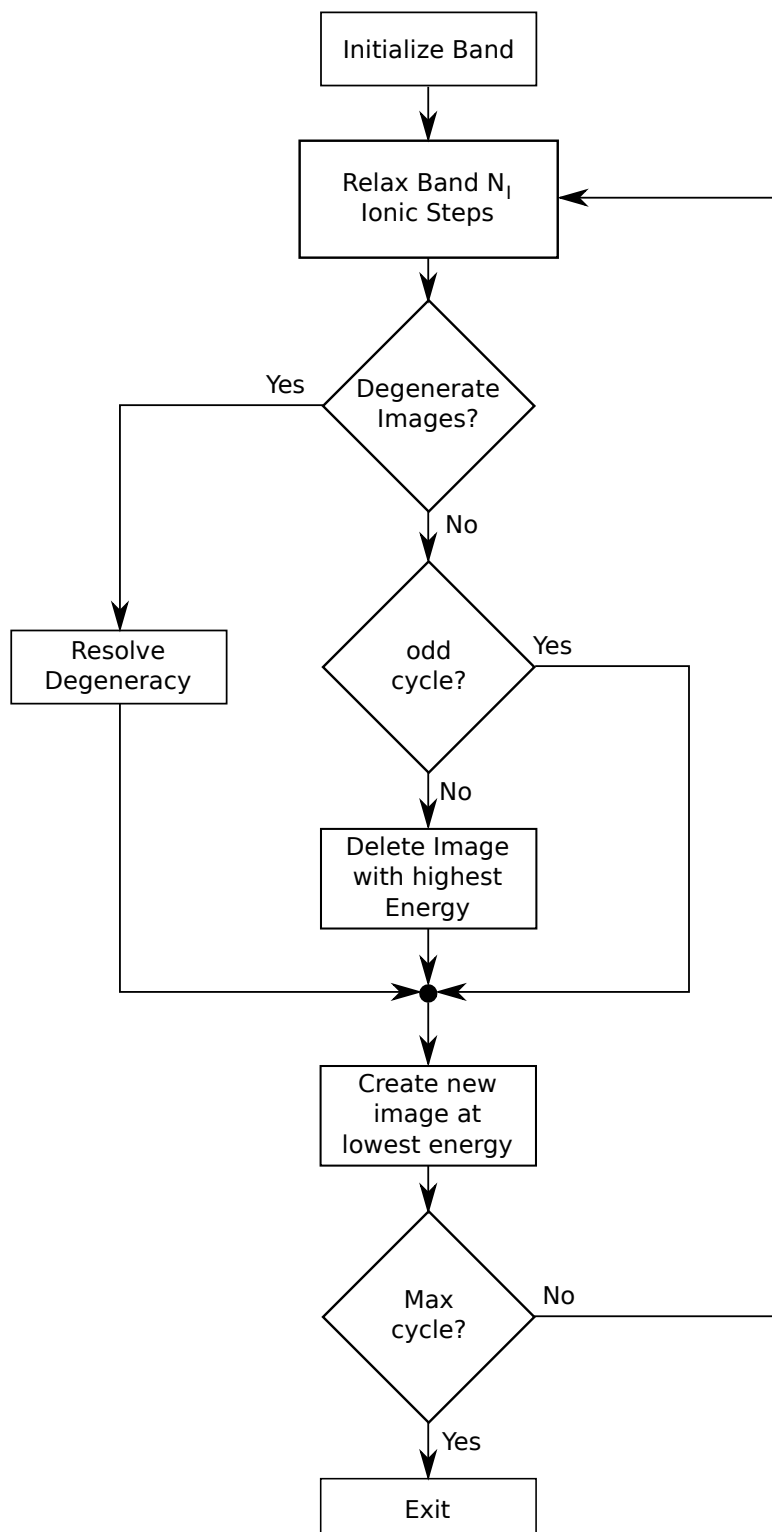


**Figure 5.4.:** Floating chart of the NEB-based optimization algorithm in the image-number changing variant

$R_a$ ,  $k$  and  $S$ . The consequences of this difference become clear when examining how the methods behave in the vicinity of various types of minima (Fig. 5.5). In simulated annealing the chance to escape the basin of attraction of the minimum in the dashed (red) lined potential is lower than in the black one, while there is little difference between the minima in the solid (black) lined and the dash-dotted (green) potential.

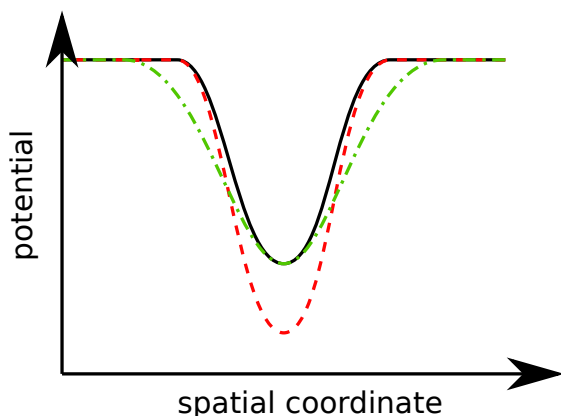


**Figure 5.5.:** Different types of minima have distinct consequences in simulated annealing and in the MsNEB method.

With this method it is also possible to obtain metastable configurations of high energy but the optimization must be executed slightly differently: The newly added images are not set to the lowest energy of the band but are randomly distributed over the band.

The following discussion is restrict to molecular applications and examples are presented to show the effectiveness and power of the algorithm, but it has to be emphasized that the MsNEB scheme can be applied to quite different optimization problems.

### 5.3. Applications

The algorithm has been tested for simple molecules e.g.  $H_2O$  starting from an oxygen atom and a hydrogen molecule, where it is easy to find the minimum. Further tests have been carried out with more complex molecules: the  $P_4$  and  $P_8$  clusters and the corresponding molecules of arsenic, antimony and bismuth. The  $P_4$  and the  $P_8$  molecules have been investigated by simulated annealing [50] and are satisfactory benchmark systems. The NEB method is used as implemented in the Vienna Ab Initio Simulation Package (VASP) without any modifications to the code. Except for the final relaxation to the minimum, intermediate precision has been used to achieve a high efficiency of the method. Increasing the precision further does not yield more information and only decreases the efficiency of the method.

The larger attractor size means that the opposite is true for the band-based optimizer. The minimum in the dash-dotted (green) potential is harder to escape from than from the one in the solid lined (black) potential, while the chances to escape from the minimum in the deeper (red) potential is equal to the one of the solid lined (black) potential. This distinction shows that the new scheme complements other procedures. It should be mentioned that - as in any NEB procedure - the method provides an upper bound for the stability of the obtained minimum by providing the barrier along the final band.

### 5.3.1. Finding the most stable isomer of the $P_4$ cluster

The  $P_4$  cluster minimum has a steep basin of attraction, and it is not easy to find in simulated annealing. Typically a “roof” or “butterfly” (see Fig. 5.10) structure is obtained by these methods. In the MsNEB method the minimum can be found in a few cycles beginning from only one pair of starting configurations.

At the start, the four phosphorus atoms are randomly placed in a  $10\text{\AA} \times 10\text{\AA} \times 10\text{\AA}$  cell and the last image  $i = N$  is initialized accordingly, noting that the images  $i = 1$  and  $i = N$  need to be quite different. The initial band is obtained by a linear interpolation connecting the initial images by a straight line in phase space. A Monkhorst-Pack K-point mesh of  $6 \times 6 \times 6$  and an energy cut-off of 270 eV has been used in LDA. The electronic structure is calculated by including five valence electrons ( $3s^23p^3$ ). The ions are described by the projector augmented wave (PAW) method by Blöchel.

The initial band had a total length of  $L_{\text{Band}} = 8.5 \text{\AA}$  and at the start  $N = 4$  images were present leading to an initial  $S_{\text{init}}$  value of  $1.7 \text{\AA}$ . Although  $S_{\text{init}}$  was small in comparison to the expected range of attraction of the stable state  $R_a \approx 2.4 \text{\AA}$ , the initial strong increase in  $S$  was accounted for in this way (after the first cycle,  $S = 2.2 \text{\AA}$ ). The images  $i = 1$  and  $i = N$  for this optimization run are shown in Fig. 5.6. One can see that they are significantly different and are not too similar to the final structure. Connecting these two images by a linearly interpolated band and letting it relax for  $N_I = 40$  steps, the energy distribution along the band shown in Fig. 5.7 is obtained. The mobile images have very similar energy after the first cycle. With the convergence parameters  $N_I = 40$  and a constant  $k = -5 \text{ eV/\AA}^2$ , the most stable isomer of the  $P_4$  was found after 11 cycles (cf. Fig. 5.9). The energy along the final band is depicted in Fig. 5.8 showing a deep minimum and a higher plateau (ca.  $-1.4 \text{ eV}$ ) in the vicinity of it corresponding to the “roof” structure mentioned before (cf. Fig. 5.10).

### 5.3.2. Finding the most stable isomer of the $P_8$ cluster

In 1990 Jones and Hohl found a new most stable wedge like ( $C_{2v}$  symmetry, Fig. 5.13) isomer of the  $P_8$  cluster [50]. Previously it had been assumed that the high symmetry of the cubic structure would be favored.

Again the initial images are set up with different random positions of all eight  $P$  atoms in both a  $10\text{\AA} \times 10\text{\AA} \times 10\text{\AA}$  computational cell using a  $6 \times 6 \times 6$  K-point mesh and a  $12\text{\AA} \times 12\text{\AA} \times 12\text{\AA}$  computational cell using a  $3 \times 3 \times 3$  K-point mesh with the same computational parameters as in the  $P_4$  calculation. A linear interpolation of the atomic positions was used to obtain the initial band. With  $S_{\text{init}} = 1.8 \text{\AA}$  the starting value was again smaller than the expected range of attraction,  $R_a \approx 3.5 - 5 \text{\AA}$  to compensate the initial rise in  $S$  (cf. Fig. 5.11). In the small unit cell the structure of Jones and Hohl was obtained, showing that the new scheme can quickly reproduce well-known stable structures without including any assumptions. In the larger unit cell, however, a configuration that is more stable than the previous one has been obtained (cf. Fig. 5.13), namely a dimer of two  $P_4$  clusters.

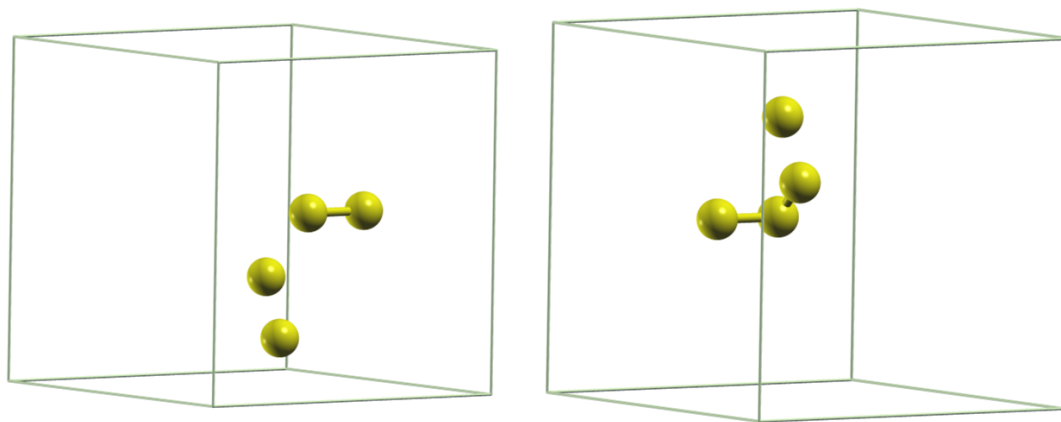


**Figure 5.6.:** The first and last image of the initial band in the  $P_4$  optimization. [48]

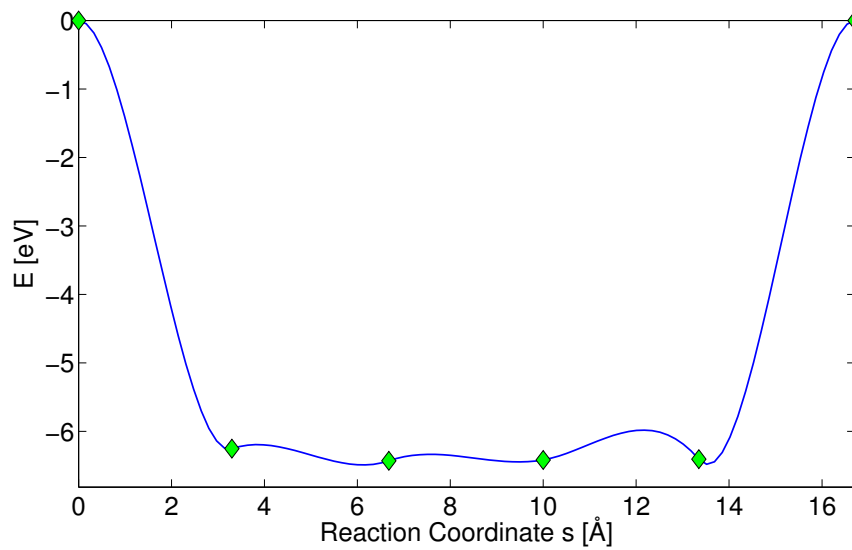


**Figure 5.7.:** Energy along the initial Band in the  $P_4$  optimization.

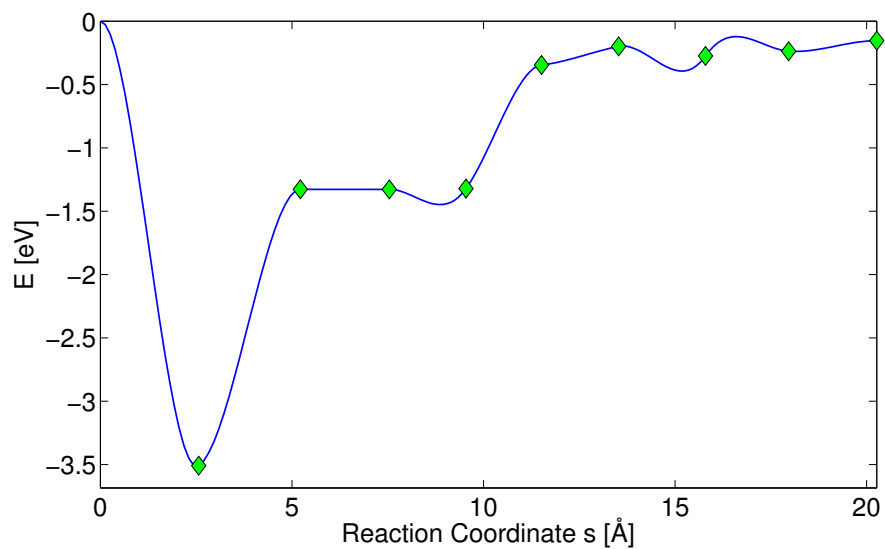


**Figure 5.8.:** Energy along the final Band in the  $P_4$  optimization. The second image corresponds to the most stable  $P_4$  isomer.

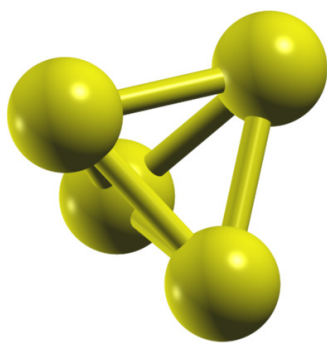


**Figure 5.9.:** The optimized  $P_4$  cluster is a tetrahedron. [48]

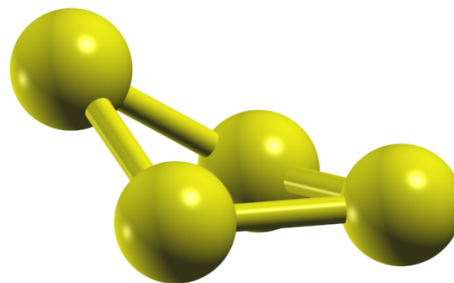


**Figure 5.10.:** “Butterfly” or “roof” structure of the  $P_4$  molecule. [48]

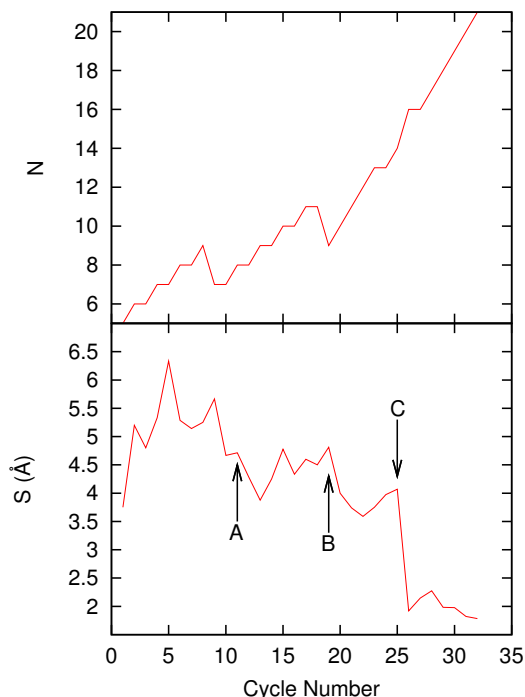


**Figure 5.11.:** The development of  $S$  throughout the optimization of the  $P_8$  cluster as a function of the cycle number  $j$  (bottom panel) and the number of images in the band (top panel). At point *A* the dimer structure is observed for the first time and persists as the lowest energy state through the following optimization. At point *B* and *C* the procedure was changed to reduce  $S$  further.

The size of the computational cell affects the path of the optimization process and can affect the final structure. In the unit cell with a side length of  $10 \text{ \AA}$  only the wedge-like structure was found. It is very hard to find the dimer structure in this cell, while in the  $12 \text{ \AA}$  cell it was found quickly. The reason is the spatial extent of the structures. In the small cell the available phase space is too limited for the dimer structure to develop, while the more compact wedge-like structure can develop. Although the dimer structure is also more stable than the wedge-like configuration in the small cell, it cannot be found easily by the optimization scheme. A cell that is too large is also not ideal, since it is computationally more demanding and one or more atoms can be pushed away from the others by the artificial spring forces. Such atoms are unlikely to be incorporated into the molecule, but appropriate periodic

This structure was relaxed with higher accuracy ( $900 \text{ eV}$  energy cut-off in a  $20 \text{ \AA} \times 20 \text{ \AA} \times 20 \text{ \AA}$  computational cell), and the energies in LDA and in GGA-PBE are given in Tab. 5.1.

In Fig. 5.11, the development of  $S$  throughout the optimization of  $P_8$  in the  $12 \text{ \AA} \times 12 \text{ \AA} \times 12 \text{ \AA}$  unit cell is shown. Up to cycle 18, the algorithm led first to a strong increase of  $S$  and then to a decrease, until it oscillates around a value of about  $4.5 \text{ \AA}$ . After the strong initial rise of  $S$ , the increase of  $L_{\text{Band}}$  slows down and  $S$  is then decreased by the increase of images. To systematically decrease  $S$  further  $N_I$  is reduced to 10 and a new image added after every cycle. Since parts of the band always enlarge further in the phase space, this procedure will also approach its limit. If  $S$  has to be decreased further, another very efficient way is to remove unimportant high-energy parts of the band, while redistributing the number of images removed over the remainder. This has been done at cycle 26 (cf. Fig. 5.11 point *C*) decreasing  $S$  from  $4.0 \text{ \AA}$  to  $1.9 \text{ \AA}$ , after which  $S$  does not change considerably. Although one has the option to decrease  $S$  systematically in this way, it was unnecessary in the cases at hand, since the most stable isomer was typically found much faster (the lowest energy was found here after only 11 cycles).

The size of the computational cell affects

	LDA	$E - 2 \cdot E_{P_4}$	PBE	$E - 2 \cdot E_{P_4}$
$2 \cdot E_{P_4}$	-44.6964	0	-41.9968	0
$E_{Dim}$	-44.9726	-0.2762	-42.0295	-0.0327
$E_{wedge}$	-44.8755	-0.1791	-41.5674	0.4294

**Table 5.1.:** Energies (in eV) of the  $P_8$  cluster in different configurations

boundary conditions can prevent this. The cell size (phase-space) has to be experimented with in practice to discover new structures.

Due to the chemical similarity of the elements in the group 15 (except nitrogen) the new optimization algorithm has also been applied to the four and eight atom clusters of *As*, *Sb* and *Bi*. In these systems either the wedge-like configuration or the dimer configuration was found, as well. Also in these cases the cell-size dependence arises: The dimer structure was found only in large cells, while in the smaller cells only the wedge-like structure occurred. Comparing the energies of the two stable isomers in all cases (cf. Tab. 5.2) one finds that  $As_8$  is also more stable in the dimer structure,  $Sb_8$  is more stable in the wedge-like structure and in  $Bi_8$  both structures have nearly the same energy. In LDA, however, the wedge like structure is always more stable in these compounds (cf. Tab. 5.3).

Although both structures are very similar in energy in all systems, the transition from one structure to the other is very unlikely. In fact, due to the different symmetries the energy barrier between the structures is very high. Following the direct process proposed by Chen et al. [61], the pathway passes an intermediate state leading to a two barrier transition (Fig. 5.12). The two tetrahedra approach each other with one of their bonds elongating until it breaks. When each  $P_4$  molecule has one bond broken, the first transition state is reached having a height of  $\Delta E_1 = 2.97$  eV. The two phosphorus atoms of the broken bond approach the analog atom from the other  $P_4$  cluster forming the intermediate stable isomer (cf. Fig. 5.12). This structure is higher in energy than the other two, but due to the high barriers, it also has a long lifetime once formed. In the transformation to the wedge structure, one side of the intermediate structure rotates clockwise and the other side rotates anti-clockwise until one of the previously formed bonds breaks again, while the two atoms align along the short axis of the cluster. The maximum is reached when the bond just breaks and has a height of about  $\Delta E_2 = 1.29$  eV in reference to the intermediate state. When three parallel atom pairs alignments form, the wedge structure is reached.

The work of Janoschek [64] in 1992 corroborates these findings. He showed that in MP2+ZPE no  $P_8$  cluster is more stable than two separated  $P_4$  clusters. If two  $P_4$  tetrahedron approach each other, the energy of the two-cluster system will drop slightly indicating that the dimer structure is in fact lower in energy than any other  $P_8$  cluster. In 1993 Kumar et. al reported [65, 66] a new most stable isomer in the  $Sb_8$  system. They found the same dimer cluster the MsNEB optimizer discovered for the  $P_8$  cluster. However, in the computations of the  $Sb_8$  cluster presented here, it was not possible to reproduce the dimer configuration as the most stable isomer neither in LDA nor in PBE.

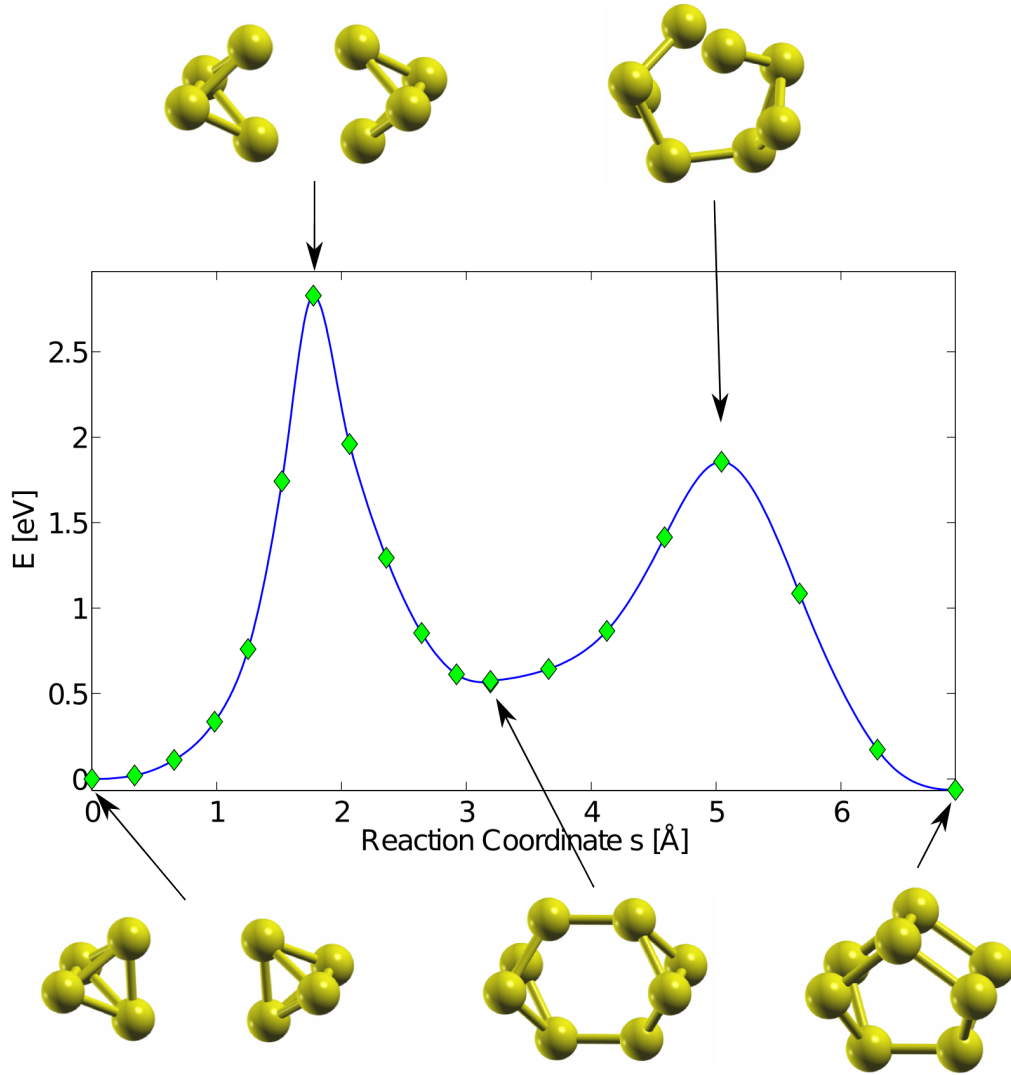


**Figure 5.12.:** MEP from the dimer structure to the wedge structure. Note that the dimer structure is rotated to have a better starting position for the transition, which is about 0.14 eV higher in energy than the dimer ground-state. [48]

	$As_8$	$Sb_8$	$Bi_8$
$E_{Dim}$	-35.878	-30.681	-29.829
$E_{wedge}$	-35.703	-30.734	-29.827
$E_{Dim} - E_{wedge}$	-0.175	0.053	-0.002

**Table 5.2.:** Energies (in eV) of the  $Sb_8$ ,  $As_8$  and  $Bi_8$  clusters in wedge and dimer configurations. All calculations are done in GGA-PBE with 600eV energy cut off and a k-point mesh of  $3 \times 3 \times 3$  in a cubic computational cell with the side length of  $13 \text{ \AA}$  ( $As_8$ ),  $14 \text{ \AA}$  ( $Sb_8$ ) or  $20 \text{ \AA}$  ( $Bi_8$ ).

	$As_8$	$Sb_8$	$Bi_8$
$E_{Dim}$	-39.362	-33.961	-31.883
$E_{wedge}$	-39.453	-34.961	-31.977
$E_{Dim} - E_{wedge}$	0.091	0.219	0.095

**Table 5.3.:** Energies (in eV) of the  $Sb_8$ ,  $As_8$  and  $Bi_8$  clusters in wedge and dimer configurations. All calculations are done in LDA, other parameters are as stated in Tab. 5.2.

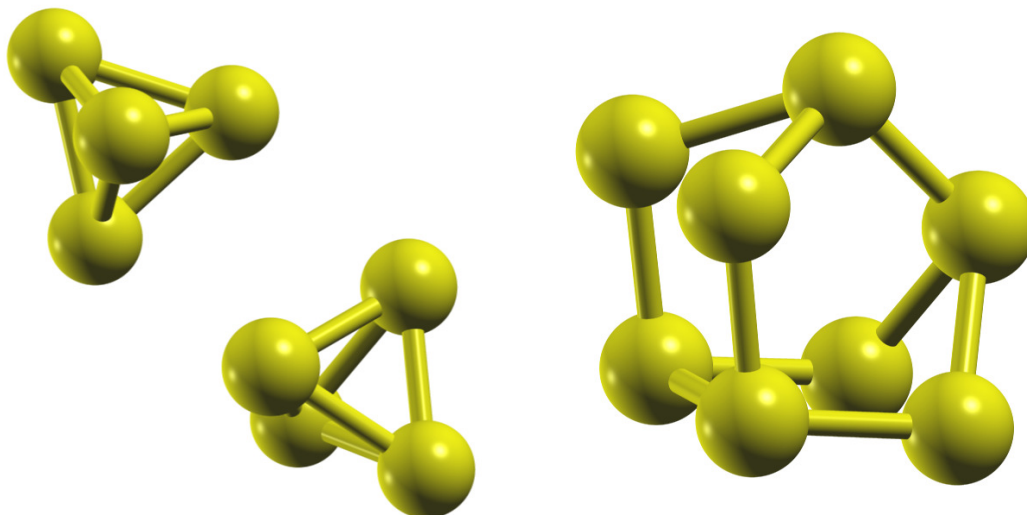


**Figure 5.13.:** The low energy states of the  $P_8$  cluster as found by the MsNEB optimization scheme in DFT. Left: new dimer structure, Right: wedge-like structure found by Jones and Hohl. [48]

Although the long bond between two  $P_4$  clusters may not be described well in DFT, it is clear that this structure is more stable than all previously found structures in DFT, showing that the new optimization method can quickly discover new minima in a given phase space.

In this chapter a new optimization scheme being based on the NEB method has been introduced. It differs to the energy-based methods, like simulated annealing and the genetic algorithm, by the way it escapes local minima. While the probability to escape in SA and GA depends on the depth of the minimum, it depends on the width of the minimum in the MsNEB scheme, making it a complementary one. Its power has been shown by applying it to some test cases, where it was even able to find a new most stable isomer in  $P_8$ . In the following chapters, the NEB method is applied in its original purpose to the oxygen motion in zirconia to find appropriate MEPs. In the next chapter, the various types of electrolyte materials are discussed and a deeper look into the doped zirconia is taken.

## 6. Electrolyte materials

### 6.1. SOFC electrolytes

#### 6.1.1. Requirements to SOFC electrolyte materials

A high ionic conductivity and a negligible electronic one are the two main requirements any fuel-cell electrolyte material has to fulfill. However, these are by far not the only requirements. For SOFC electrolyte materials Goodenough [67] gave a list of such requirements:

1. The material has to be easily fabricable into very thin, mechanically stable, layers and possibly into complex shapes.
2. The oxide-ion conductivity of the material has to be larger than  $10^{-2}$  S/cm at the operating temperature of the cell. If the ionic conductivity is low, a high operating temperature is required.
3. The barriers for the oxygen ions inclusion into the electrolyte at the cathode interface and for the oxygen ion extraction at the anode interface must be low. A mechanical and chemical compatibility to the electrode materials is, therefore, required.
4. The electronic conductivity through the electrolyte layer must be insignificant at the operating temperature.
5. The material has to be chemically stable in an environment being oxidizing at the anode and reducing at the cathode. To achieve a thermodynamic stability with the reactants, the highest occupied molecular orbital (HOMO) of the reductant and the lowest unoccupied molecular orbital (LUMO) of the oxidant must both lie in the band gap of the electrolyte (with the HOMO of the reductant being higher than the LUMO of the oxidant)
6. Mechanical stability against thermal cycling between ambient temperature and operating temperature has to be achieved by matching thermal expansion coefficients of electrolyte and electrode material. Compressive strain enhances the mechanical stability of the electrolyte. Thus, the cell design of modern SOFCs typically results in such a compression (pressures in the range of a few hundred MPa compress the electrolyte [68]).
7. The material and fabrication cost should match the operating life of the fuel cell and be as low as possible.

These requirements show impressively the complexity of finding superior materials. While in the past, many new compounds have been found showing very high ionic conductivity at low temperatures, many of them do not fulfill all of the given requirements. Either the problems are prohibitively large, so that they are basically not qualified for SOFC applications, or further development has to be executed to show that such an application is feasible.

### 6.1.2. Yttrium Stabilized Zirconia (YSZ) and Scandium Stabilized Zirconia (SSZ)

Yttrium stabilized zirconia is clearly the most common solid state oxygen ion conductor. One application of YSZ is the usage in lambda probes for the analyze of exhaust gas conditions of combustion engines in cars. Due to the high oxygen ion conductivity and the high thermal stability, it can be used to determine the oxygen concentration in the exhaust gas, which is an indicator whether the fuel/air mixture in the combustion engine is fuel rich or fuel lean.

Furthermore, YSZ is used as a coating of turbine blades due to the high thermal stability and the low thermal conductivity, thus protecting the thermal sensitive parts of the turbine from overheating. However, in this thesis this material is solely of interest for its application as an ionic conductor in the SOFC.

Doping zirconium oxide  $ZrO_2$  (zirconia) with yttrium oxide  $Y_2O_3$  both generates oxygen vacancies and stabilizes the high temperature cubic fluorite phase of the zirconium oxide. These are two crucial requirements to make zirconia a distinguished ionic conductor. YSZ shows excellent chemical and mechanical stability [69] and operation times in stationary SOFC applications of over 40,000 hours [28].

Scandium has the same number of valence electrons as yttrium, and is, therefore, chemically very similar to it. Scandium oxide  $Sc_2O_3$  crystallizes in the same structure as yttrium oxide. When used as a dopant in zirconia, it equally provides vacancies and stabilization of the cubic phase. While yttrium ions are larger (180 pm) than zirconium ions (159 pm), scandium differs only little to zirconium on this aspect (162 pm). In comparison to YSZ, SSZ exhibits a higher ionic conductivity. Additionally, under external pressure, the conductivity of SSZ drops slower than the one of YSZ (c.f. chapter 7). The reason why YSZ is the commonly used electrolyte and not SSZ is the abundance and the price of the raw materials. While the production of yttrium reached a value of 600 tons per year in 2001 [70], scandium is only found in traces and has a worldwide production of only 2 ton per year [71], resulting in yttrium prices of about 170 US\$ per kilogram [72] and in scandium prices of about 10,000 to 13,000 US\$ per kilogram<sup>1</sup>. These current prices are under the condition of the low demand. If SSZ would be used in fuel cell products for the actual customer market, the demand would exceed the supply by many times, raising the price much higher than the current value. The current prices alone would already prevent the application of scandium in fuel cell products, not to mention the price reactions the increased demand would induce.

---

<sup>1</sup>The scandium prices are based on a short online survey of scandium offers, since no official data can be found.

### 6.1.3. Other electrolyte materials under development

**CGO** Gadolinium doped cerium oxide  $CeO_2$  (CGO) is besides the zirconia based materials the most promising and most used electrolyte material for SOFCs. CGO also crystallizes in the fluorite structure, and has a higher ionic conductivity than YSZ, especially at low temperatures  $\varsigma_{YSZ}(T = 1000^\circ C) \approx 11 \text{ S/m}$ ,  $\varsigma_{CGO}(T = 1000^\circ C) \approx 12 \text{ S/m}$ ,  $\varsigma_{YSZ}(T = 750^\circ C) \approx 0.8 \text{ S/m}$  and  $\varsigma_{CGO}(T = 750^\circ C) \approx 2 \text{ S/m}$  [69]. Although CGO has a capability to be a good intermediate temperature SOFC electrolyte, it suffers from electronic conductivities at low oxygen partial pressures and a mechanical stability being weaker than the one of YSZ.

**LSGM** Strontium and magnesium doped lanthanum gallium oxide ( $LaGaO_3$ ) is a perovskite exhibiting even higher oxygen ion conductivities at low temperatures than CGO  $\varsigma_{LSGM}(T = 750^\circ C) = 3 \text{ S/m}$ . However, along with this high conductivity come severe caveats: the gallium evaporates at low oxygen partial pressures, it is not compatible with nickel oxide being the standard catalyst of SOFCs, and has a low mechanical stability [69].

**BIMEVOX** Bismuth oxide  $\delta - Bi_2O_3$  has the highest known oxygen ion conductivity of about  $\varsigma_{BiO}(T = 800^\circ C) = 230 \text{ S/m}$ , but is only stable between  $730^\circ C$  and  $804^\circ C$  preventing a direct application in SOFCs [67]. Bismuth vanadium oxide  $Bi_4V_2O_{11}$  (BIMEVOX) is a new type of oxygen ion conductor being based in the cubic  $\delta - Bi_2O_3$  structure. It is stabilized down to room temperature, but the conductivity suffered severely under the stabilization. Nevertheless, it still has an extremely high ionic conductivity of about  $\varsigma_{BIMEVOX}(T = 600^\circ C) = 10 \text{ S/cm}$  [73]. The tendency to increase the number of technical problems with higher ionic conductivity progresses: BIMEVOX materials suffer from very high thermal expansion coefficients, substantial electronic transport, low thermodynamic stability in operating environment, evaporation of bismuth oxide and very high chemical reactivity [74].

Considering the complexity to find new materials for SOFC utilization, it is a reasonable approach to investigate the well-known and well-performing materials in more detail from a different perspective, and improve them. The newly gained knowledge will most likely be transferable to the materials under intense development. Based on the advantages and disadvantages of the available materials, one can conclude that the most suitable electrolyte material for SOFC applications is SSZ, being very stable, having an ionic conductivity comparable to the one of LSGM at about  $1000^\circ C$  and to CGO at about  $500^\circ C$ . However, the scarcity and the cost inhibit a large scale application of this material. Following this argumentation, YSZ seems to be the best choice to take a further look at.

Phase	$E_0$ [eV/atom]	$V_0$ [ $\text{\AA}^3$ /atom]	$B_0$ [GPa]	$B'_0$
monoclinic	-9.514	12.3	198.51	4.276
tetragonal	-9.469	11.8	144.2	6.364
cubic	-9.439	11.4	232.36	4.258

**Table 6.1.:** BM-eos parameters obtained from fitting the equation of state to the calculation results (cf. left panel of Fig. 6.2)

## 6.2. Zirconium-dioxide $ZrO_2$

### 6.2.1. Zirconia Phases

Pure zirconia has three different phases occurring under normal pressure. At low temperatures (0 K - 1173 K) zirconia is in the monoclinic phase, at intermediate temperatures (1173 K - 2370 K) in the tetragonal phase and between 2370 K and the melting point at 2680 K in the cubic fluorite phase [75]. The structures are presented in Fig. 6.1. The tetragonal phase is a deformed version of the cubic fluorite phase, which is very well visible in direct comparison. Fig. 6.1(c) shows the tetragonal phase in the pseudo fluorite cell illustrating the difference being only in the oxygen sub-lattice. Indicated by missing bonds, the oxygen ions are shifted from the cubic positions, e.g. the lower-outer ions are shifted inwards and the upper ones shift outwards leading to a pattern of alternating oxygen ion shifts. In Fig. 6.2 the cohesive energies of the three natural zirconia phases are plotted over the cell volume showing the correct ordering at zero temperature. These computations are done with a high energy cut off  $E_{\text{cut}} = 1000$  eV and with k-point meshes showing convergence for each compound -  $5 \times 5 \times 5$  (monoclinic),  $7 \times 7 \times 7$  (tetragonal and cubic). The exchange and correlation effects have been accounted for in the GGA-PBE scheme. The energies obtained from VASP are fitted to a Birch-Murnaghan equation of state (BM-eos) [76]

$$E(V) = E_0 + \frac{9B_0V_0}{16} \left\{ \left[ \left( \frac{V_0}{V} \right)^{2/3} - 1 \right]^3 B'_0 + \left[ \left( \frac{V_0}{V} \right)^{2/3} - 1 \right]^2 \left[ 6 - 4 \left( \frac{V_0}{V} \right)^{2/3} \right] \right\} \quad (6.1)$$

with the minimum energy  $E_0$ , the minimum volume  $V_0$ , the bulk modulus at the minimum volume  $B_0$  and the change of the bulk modulus with the pressure  $B'_0 = (\partial B / \partial P)_T$ . The values obtained from fitting the BM-eos to the calculated cohesive energies are given in Tab. 6.1. At volumes larger than  $10.5 \text{\AA}^3$  the cubic phase is metastable, therefore both in the fixed configuration and the relaxed configuration the difference between cubic and tetragonal phase is visible. However, the tetragonal ordering of oxygen ions is unstable under sufficient compression of the lattice and the tetragonal phase will relax to the cubic fluorite configuration as depicted in the left panel of Fig. 6.2.

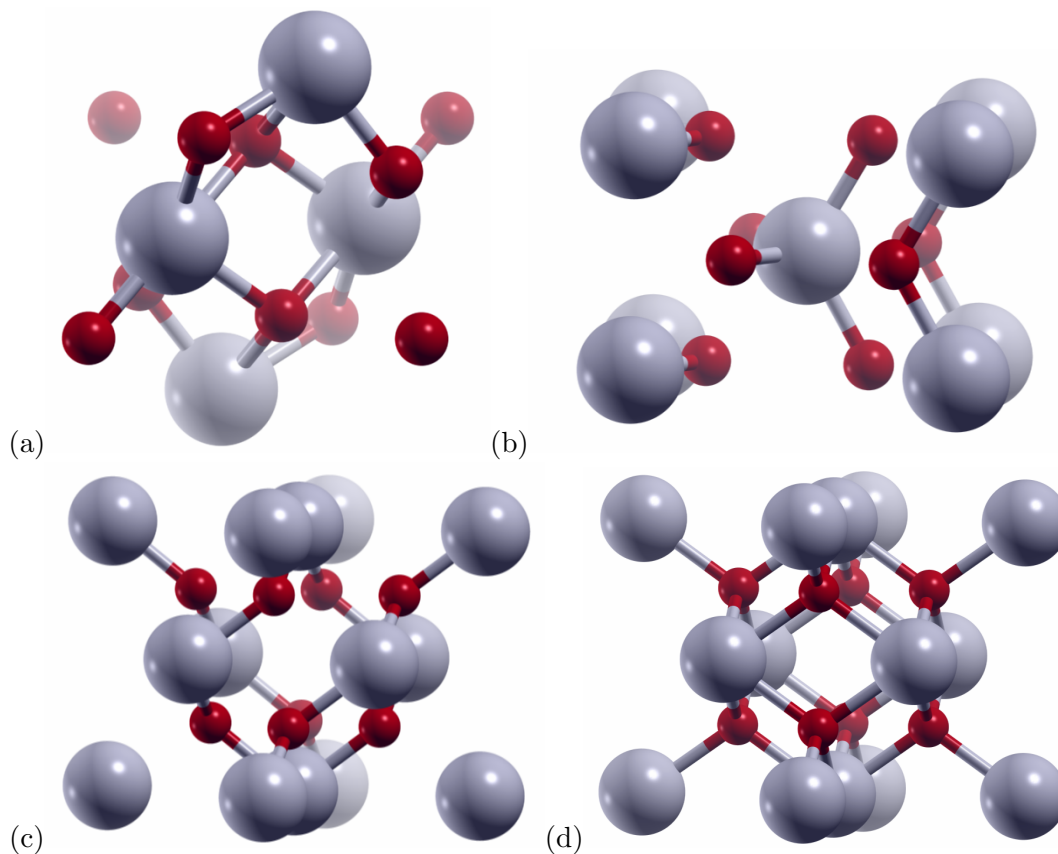


**Figure 6.1.:** The  $ZrO_2$  phases at zero pressure. The monoclinic phase (a), the tetragonal phase in its unit cell (b), the tetragonal phase in the pseudo-fluorite cell (c), and the cubic fluorite phase (d). (grey: zirconium, red: oxygen)[48]

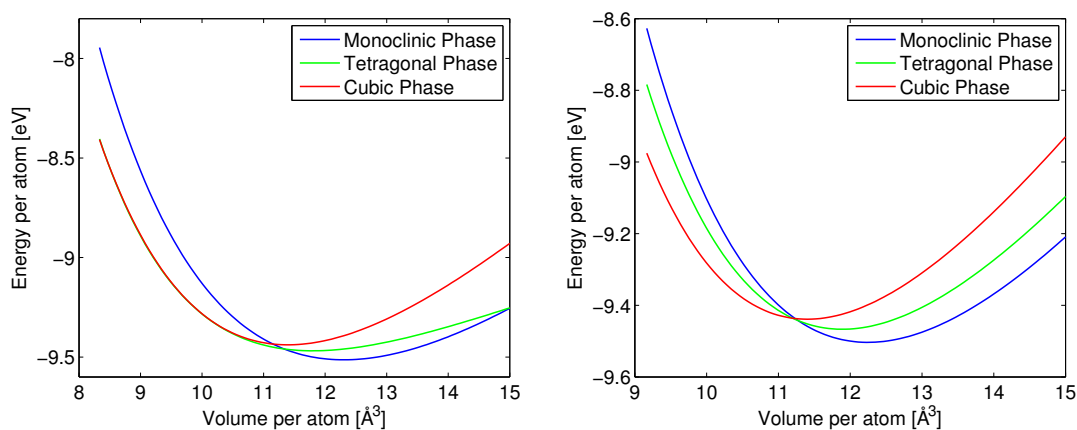


**Figure 6.2.:** Cohesive energies of the three zirconia phases (BM-eos). Left panel with relaxation of ions at each volume and right panel with fixed ionic configuration.

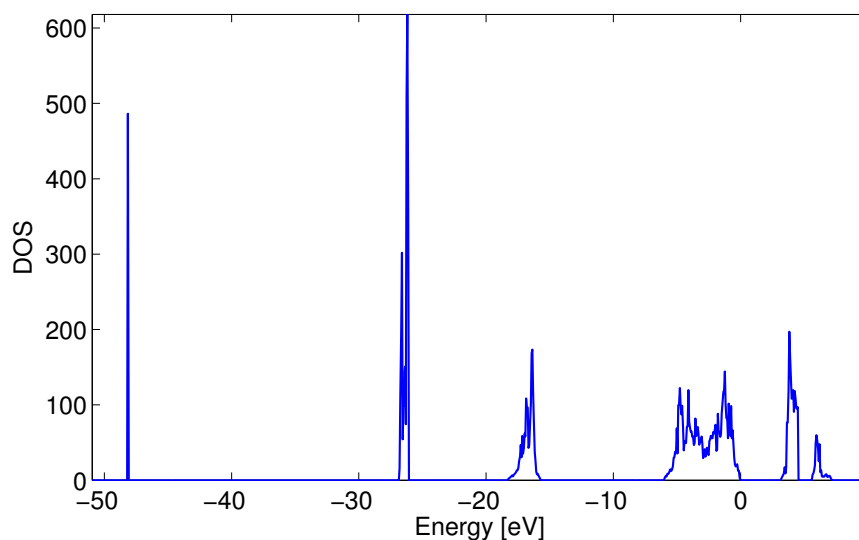


**Figure 6.3.:** Density of states of cubic zirconia. The energy is given in reference to the Fermi energy ( $E - E_F$ ).

### 6.2.2. Electronic properties of zirconia

Zirconia is a wide band-gap insulator, therefore the electronic conductivity will be negligible. In Fig. 6.3 the density of states of the cubic phase is depicted from which a band gap of 3.1 eV can be extracted. Although, this is already a large band gap, it is by a factor of 2 smaller than typical values from experiments. This difference can be accounted for by the systematical underestimation of band gaps by standard DFT. Experiments determined band gaps of 5.7 eV to 7.08 eV [77, 78, 79]. This large band-gap, and by that the very low electronic conductivity, is a crucial property for the application as an electrolyte in the SOFC to prevent the direct electronic current from the anode to the cathode. This low electronic conductivity has to be complemented by a high ionic conductivity, which is maximum in the cubic fluorite phase [75]. The temperature stabilizing this phase is greater than 2370 K, which is not feasible for SOFC applications. Since the electrolyte should not undertake a phase transition when cooled down, the cubic phase has to be stable even at room temperature, which is achievable by doping zirconia with aliovalent elements like yttrium or scandium. Including  $Y_2O_3$  or  $Sc_2O_3$  into the  $ZrO_2$  lattice gives rise to oxygen vacancies  $V_O$  – one vacancy per unit  $Y_2O_3$  or  $Sc_2O_3$ . In literature the stabilization process has been discussed widely [80, 81, 82] and findings are not consistent. Some report that the dopants are more relevant in the stabilization process [77] others claim that vacancies alone can stabilize the cubic phase [83, 84]. Despite the lack of knowledge about the exact stabilization mechanism, the experimental observation that doping zirconia with yttria stabilizes the phase with highest ionic conductivity and introduces oxygen vacancies to the lattice is irrefutable. Both are essential requirements for ionic conductivity to take place. In zirconia no metastable

interstitial positions exist, which could enable ionic motion, nor is there a significant amount of thermally generated oxygen vacancies (due to the high formation energy of vacancies in zirconia [85]). Therefore, oxygen sites have to be cleared in order for oxygen ions to migrate through the lattice. The number of vacancies is much smaller than the number of oxygen ions. Therefore, the vacancies can be considered as the charge carriers and the ionic diffusion is a vacancy conduction (similar to the hole conduction in semiconductors). More details about the ionic conductivity have been given in subsection 4.2.2.

One could assume that YSZ exhibits higher ionic conductivity when more vacancies are introduced. Although it is true that more vacancies give rise to a higher charge carrier concentration, there are effects prohibiting the conductivity:

1. **Vacancy-vacancy interactions.** Vacancies in the YSZ lattice interact with each other, typically leading to vacancy-pairs along the [111] direction and a repulsion for vacancies approaching closer than this distance. At low vacancy concentrations this effect is negligible, but could be a reason for electrolyte aging (vacancy pairs once formed have a low probability to break apart and participate in diffusion again). Vacancy pairs reduce the number of charge carriers and block the diffusion path for other vacancies.
2. **Migration blockages due to Yttrium defects.** The migration barrier for passing an yttrium ion is higher than passing a zirconium ion. Yttrium ions are larger (180 pm) than zirconium ions (160 pm) and have an ionic charge of +3 in YSZ (zirconia: +4). At minor yttrium concentration the number of high barriers along a migration pathway is low having a negligible impact on the activation energy  $E_A$  of the diffusion. With higher concentration of yttrium, also the number of insuperable barriers rises and the probability for an oxygen ion to find a pathway through the electrolyte having only small barriers decreases.

Due to these two effects the highest ionic conductivity in YSZ is achieved at 8mol% of yttria doping in zirconia. In Fig. 6.4 the kinetic monte-carlo (KMC) calculations of Pornpasertsuk et al. are shown comparing to experimental results from Ioffe et al. [86]. In their calculations they only included the barrier change due to rising yttrium content, no vacancy correlations, indicating that the maximal conductivity can already be explained by yttrium induced barrier change. The experimental results from Ioffe et al. also show that the migration barrier does not change up to a  $Y_2O_3$  content of 6mol% and rises linearly with larger yttria contents.

### 6.2.3. Charged vacancies in zirconia

Yttrium and Scandium have one valence electron less than zirconium. Therefore, when substitution one unit of  $Zr_2O_4$  with  $Y_2O_3$  or  $Sc_2O_3$ , not only an oxygen vacancy is introduced, but also two electrons removed from the system. This doping process can also be considered as the removal of an  $O^{2-}$  ion leaving a charged vacancy behind [88, 89]. If pure zirconia is used to simulate YSZ, the charge state of the vacancies

has to be considered. As will be shown, having the wrong charge type of vacancy in the system leads to wrong migration barriers and trajectories. To obtain these types of vacancies in VASP, it is possible to reduce the total number of electrons in the system. The excess charges are compensated by a homogeneous background to ensure a neutral computational cell. Although it is not possible to manually localize charges in VASP, the following argumentation should be considered: Zirconia is a wide gap insulator. As soon

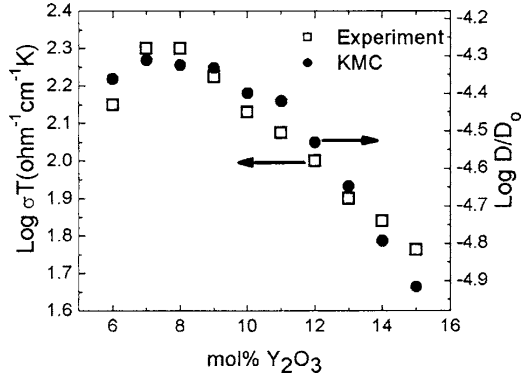


**Figure 6.4.:** Ionic diffusivity in dependence of yttrium content in cubic zirconia, showing the maximal conductivity at about 8mol%  $Y_2O_3$  content. The experiments show the same result for the conductivity. (picture taken from [90] – experimental data from [86])

As soon as oxygen atoms are removed, the metallic character increases and the vacancies will interact. This leads to filled impurity states in the gap. As soon as electrons are removed from the system, the energetically highest states will be depopulated, which are obviously the states in the gap. After an ionic relaxation it is possible, that these states vanish. An argumentation like this is necessary for both the DFT calculation and the experiment, since by doping zirconia one cannot uniquely determine, how the charges are distributed. This hypothesis is supported by the results presented in the following and by the ones in [88, 89]. Using SIESTA, a DFT code with a local basis set, Kasamatsu et al. [88] were able to show that the gap state is actually located in the vacancy. In [89] the authors pointed out that the nearest neighbor zirconium ions of the vacancy relax strongly, and therefore produce a Madelung-field, which prevents the existence of deep states in the gap.

Similar to [88] the density of states of zirconia in different electronic and ionic configurations is presented in Fig. 6.5. The computations have been executed in a  $3 \times 3 \times 3$  supercell with a total of 27 Zr ions and 54 O ions (53 O ions in the cases of a vacancy is present in the cell). For the relaxations an energy cut-off of  $E_{\text{cut}} = 400$  eV and a k-point mesh of  $3 \times 3 \times 3$  has been used to converge the residual forces acting on the ions to  $|\vec{F}_{\text{res}}| < 10^{-4}$  eV/Å. The computation of the DOS is done with a dense  $7 \times 7 \times 7$  k-point mesh and 1000 eV cut-off. In these plots only the domain around the fermi energy is shown to visualize the states arising in the gap. As a reference, the DOS of pure zirconia is depicted again in (a). In (b) and (c) one oxygen ion has been removed from the system leaving in one case a neutral vacancy  $V_O^0$  (b) and in the other case a charged vacancy  $V_O^{2+}$  behind (c). In both cases the mentioned gap state arises, either populated (b), or empty (c). In (d) and (e) these systems have undergone an ionic relaxation. The system with the neutral vacancy exhibits no big difference, however, in the system with the charged vacancy, the gap state vanished as stated in [89, 88]. In the last two panels (f)

and (e) the system was compressed to a lattice constant of  $a = 4.93 \text{ \AA}$  amounting to a compressive strain value of  $\sigma = 0.967$  (isotropic lattice compression of 3.3%).

The fact, that only in the case of charged vacancies the gap state vanishes after relaxation, implies a difference in the detailed ionic configuration between  $V_O^0$  (b) and  $V_O^{2+}$ . This in turn should also affect the barrier height of an oxygen ion jump to such a vacancy. In fact, Kasamatsu et al. [88] reported a higher barrier when jumping to  $V_O^0$  than when jumping to  $V_O^{2+}$ , and found a significant difference between the DOS at the initial state and the transition state in the neutral system. Eichler [87] reasoned that the barrier is higher since the negatively charged oxygen ion has to overcome an additional electrostatic barrier due to the electrons trapped in the neutral vacancy. However, a direct comparison of the trajectories in the two cases is not known.

In Fig. 6.6 such trajectories are shown, once with a charged vacancy and once with a neutral one. On first sight the difference is small, but the movement of the zirconium ions passed by the oxygen ion differs in detail. The transition state is identical in both cases, but the initial position of the neutral case is quite distinct from the charged case. The trajectory of the Zr ions looks like an “awareness ribbon”. First the ion moves towards the ground-state position of the charged system. Then it marches along the trajectory of the charged system, passing the barrier, and after reaching the final position of the charged system it moves towards the direction of the new vacancy position. Also the position of the jumping oxygen ion at point 2 and 4 corresponds to the positions in the charged case. Obviously, the system gains energy when moving from 1 to 2 and loses the same amount, when moving from 4 to 5, which is the motion of the system it takes in addition to the trajectory of the charged system. In Fig. 6.7 the trajectory of the zirconium ion depicted in the inlet of Fig. 6.6 is shown for the strained case. Differing to the unstrained system only in shape, exhibiting the same relation between charged and uncharged vacancies. The overall change of ionic positions between the ground state of the neutral system to the ground state of the charged system is depicted in Fig. 6.8. All oxygen ions move towards the vacancy, and all zirconium ions move away from the vacancy. Effectively, these are the responding trajectories of the system as if two positive elemental charges are added to the vacancy resulting in a repulsion of positively charged ( $Zr^{4+}$ ) ions and an attraction of negatively charged ( $O^{2-}$ ) ions. However, in the hopping process the neutral system has to move along these trajectories without the positive charge at the vacancy, requiring the overcoming of additional potential energy due to the electrostatic repulsion.

The total energies between systems of different charge states cannot uniquely be compared in DFT, but energy differences in one system can be compared to energy differences in a system of different charge state. Since the barrier configuration is identical in both cases, it can be used as a reference point, and identified in terms of energy and reaction coordinate. The in this way compared minimum energy pathways are shown in Fig. 6.9 for both the unstrained and the strained system. Also on the aspect of the potential along the pathway, the charged system correspond to the  $2 \rightarrow 4$  part of the neutral system pathway. The potential slope of the charged system is slightly more steep than in the neutral one. Peculiar are the side maxima in the neutral MEP, which make the points 2 and 4 local minima corresponding to the

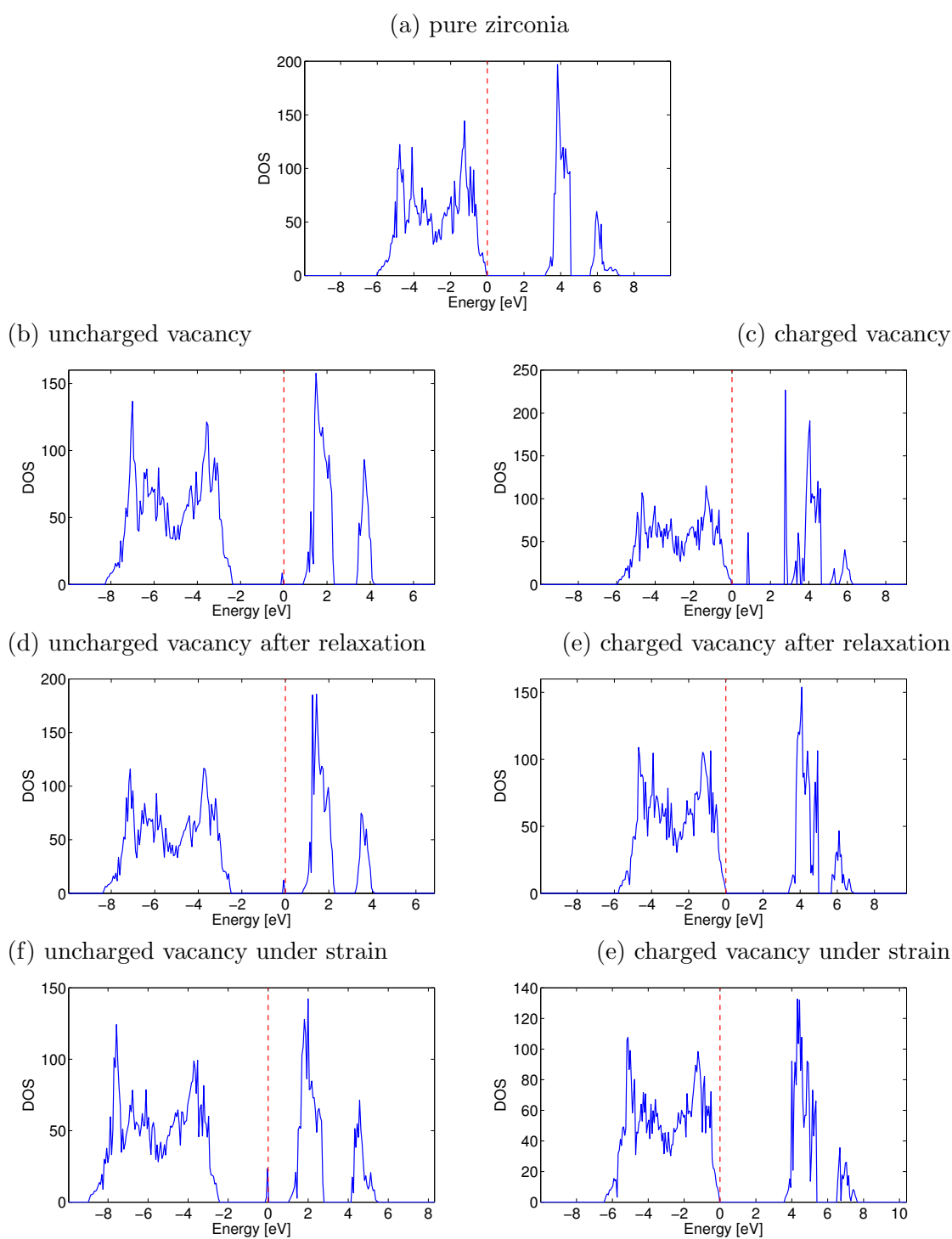


**Figure 6.5.:** Density of States in zirconia in the domain  $\pm 10$  eV around  $E_F$ . The red bar denotes the Fermi-energy.

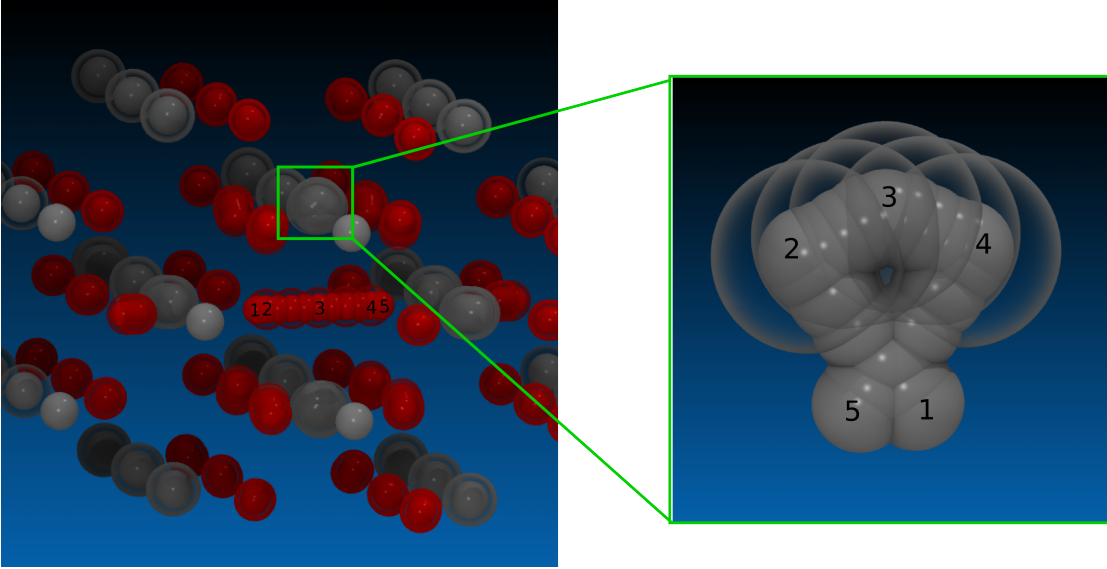


**Figure 6.6.:** Trajectories of an 1NN oxygen ion jump. Full spheres show the trajectories in a system with a neutral vacancy  $V_O^0$  and the 'glass' spheres show the corresponding trajectory in a system with a charged vacancy  $V_O^{2+}$ . The zoomed-in frame depicts the movement of the zirconium ion which is passed by the oxygen ion in the jump. (grey: zirconium, red: oxygen)

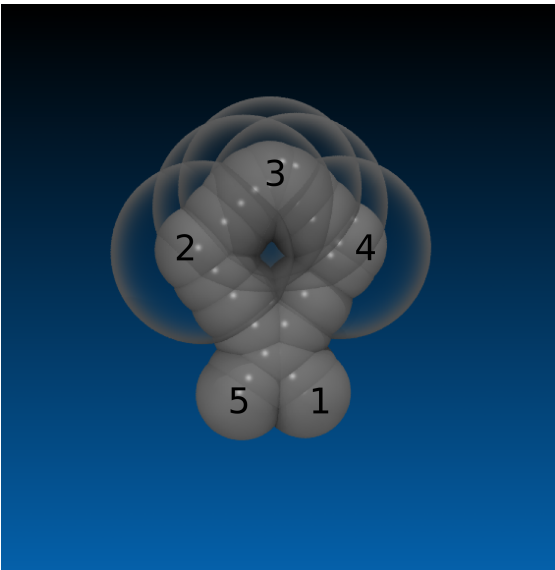


**Figure 6.7.:** The same as the inset in Fig. 6.6, but with the system being exposed to external pressure.

ground state of the charged system. In the strained case qualitatively the same result is obtained. However, the side maxima are much smaller and the difference between the two curves diminishes. The energy difference at point 2 (4) between the charged and the neutral pathway in the unstrained system is  $E_{\text{diff}} = 0.05 \text{ eV}$  and the height of the side maximum in relation to the local minimum at 2 (4) is  $E_{\text{SM}} = 0.184 \text{ eV}$ . Under strain, these values are  $E_{\text{diff}} = 0.059 \text{ eV}$  and  $E_{\text{SM}} = 0.028 \text{ eV}$ . While the absolute value of the energy difference at 2 (4) seems to change only little under variation of the strain, the side maximum height drops immensely under strain. In dependence of the systems' charge state, the upper barrier – the part of the band corresponding to the charged vacancy MEP – rises ( $E_{\text{diff}} > 0$ ) linearly with the charge number (cf. Fig.

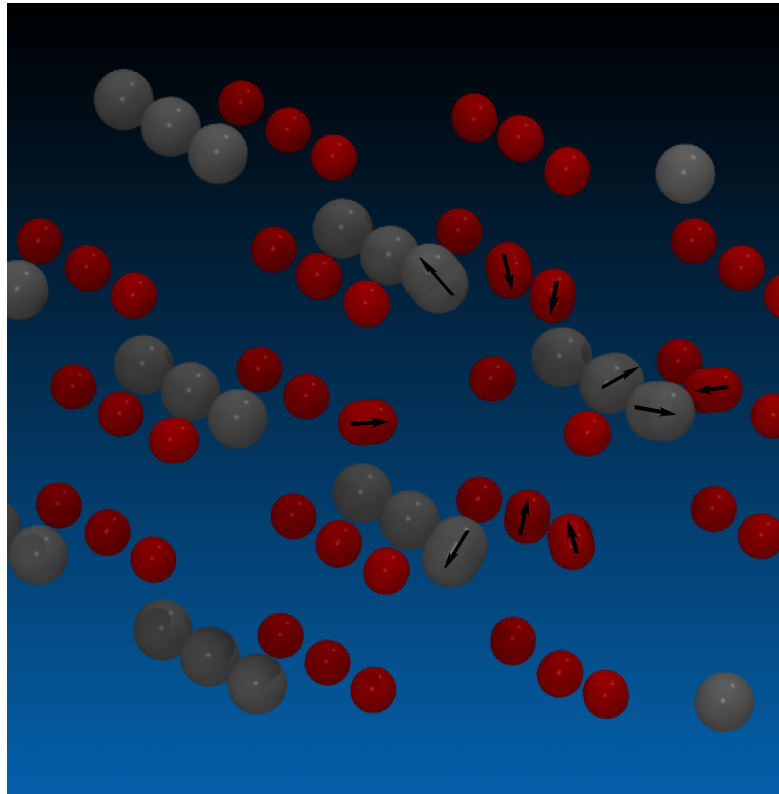


**Figure 6.8.:** Difference between the ionic ground-state with a charged and with a neutral vacancy. The arrow denote the motion from the neutral system to the charged system. The vacancy is located between the two central oxygen ions (slightly to the right), to where all oxygen ion arrows point to. (grey: zirconium, red: oxygen)

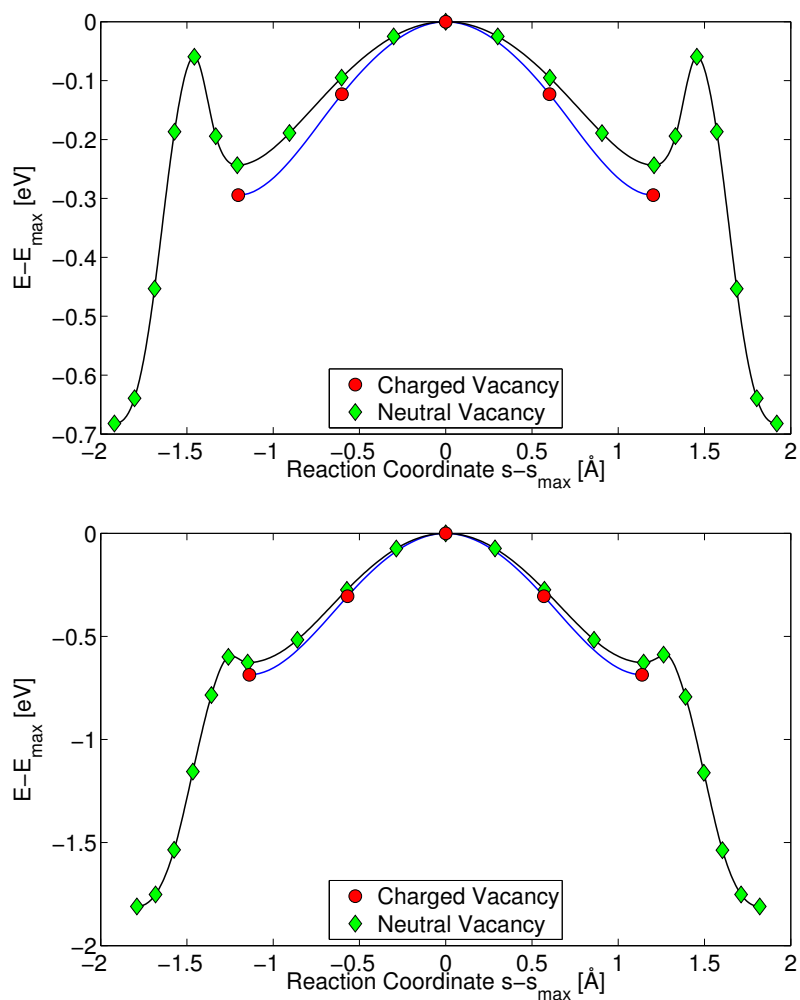


**Figure 6.9.:** The MEPs of the charged and neutral system plotted each in reference to the maximum along the band. Top at no external pressure and bottom at a strain of  $\sigma = 0.967$ . Black and blue lines are spline interpolation.

6.10). However, it has to be stated that these calculations are done in a system with only one vacancy, and Kasamatsu et al. [88] pointed out that two singly charged vacancies are unstable, and the two charges will localize in only one of the two vacancies. Additionally, in a system with only one vacancy and more than two positive charges, the Fermi energy moves into the valance band introducing a metallic character in the system. Therefore, the results from Fig. 6.10 can only be considered as a tendency.

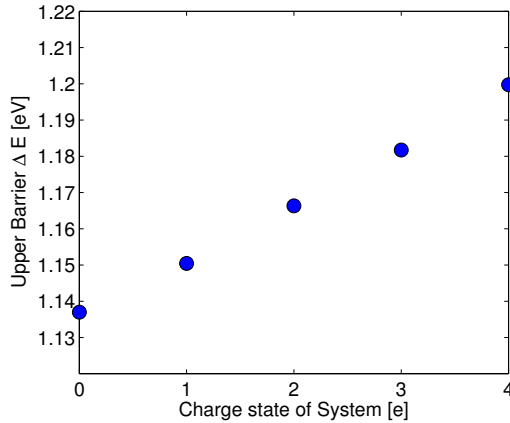


**Figure 6.10.:** Energy difference between 2 and 3 (the upper barrier) in dependence of the charge state of the system. These calculations have been done in a strained system with a lattice constant of  $a = 4.75 \text{ \AA}$ .

In this section the electrolyte materials at hand have been discussed, and what requirements have to be fulfilled by them. This showed impressively what a major task it is to find completely new materials, which perform better than the state of the art materials, and at the same time are applicable in SOFC environment. For this reason a further look at YSZ is meaningful, if taken from a different point of view. The basic properties of zirconium-oxide have been discussed, and especially the problems corresponding to the charge state of vacancies in YSZ have been addressed. With this foundation, the strain dependence of the migration barrier, being a crucial quantity for ionic motion in solid state bodies, is determined in pure zirconia, YSZ and SSZ giving new insights into this already well studied material.

## 7. Strain Dependent migration barrier

As mentioned before, one prerequisite to improve YSZ further is an understanding of the electrolyte under various conditions. In this chapter the dependence of the ionic conductivity on lattice strain is investigated based on DFT calculations and a conclusive analytic discussion of the phenomenon is provided. Due to different thermal expansion coefficients of the materials in use, the electrolyte already experiences strain. Engineering the strain in such a way, that it has a positive effect on the ionic conductivity of the electrolyte, will lead to an additional enhancement of the fuel cell efficiency.

In the first section the focus is on one basic migration configuration without any correlation effects over a wide range of strain to understand the physics behind the strain dependence [91]. Due to the exponential dependence (Eq. 4.15 and Eq. 4.25), the performance of the electrolyte is assessed only from the migration barrier at a given strain. Such an exponential dependence of the ionic conductivity with respect to external strain has been reported in [3, 4, 6, 8, 9, 10] supporting this kind of procedure.

To understand the DFT results, a simple atomic model consisting of five ions with Lennard-Jones (LJ) interactions between them has been set up. The strain dependence is accounted for by setting the zirconium ion distance corresponding to the one obtained in DFT for each strain value.

In the following sections of the chapter the investigations are extended to doped zirconia, to gain an understanding of the role of the dopants under strain.

### 7.1. Strain dependence in $ZrO_2$

#### 7.1.1. Ab initio approach

##### 7.1.1.1. DFT Calculations

To determine the strain dependency of the migration barrier  $\Delta E$  for the oxygen ion jumps in zirconia  $ZrO_2$  the DFT calculations used a plane wave basis set up to an energy cut-off of 600 eV, as well as a  $3 \times 3 \times 3$  Monkhorst-Pack mesh for the k-point sampling. For both, the plane wave basis set and the k-point sampling the energy convergence has been tested to guarantee accurate results. The computational cell is again built up by  $3 \times 3 \times 3$  unit cells<sup>1</sup>, with a total of 27 zirconium ions, 53 oxygen ions and one oxygen vacancy. The oxygen atoms have been described by 6 ( $2s^2 2p^4$ ) valence electrons and the zirconium atoms by 4 ( $4d^3 5s^1$ ). The results have also been tested by using another pseudo-potential with 12 valence electrons ( $4s^2 4p^6 4d^3 5s^1$ ) for the zirconium atoms, but no qualitative difference has been observed.

---

<sup>1</sup>The results are also confirmed in a  $4 \times 4 \times 4$  supercell with a total of 191 ions.

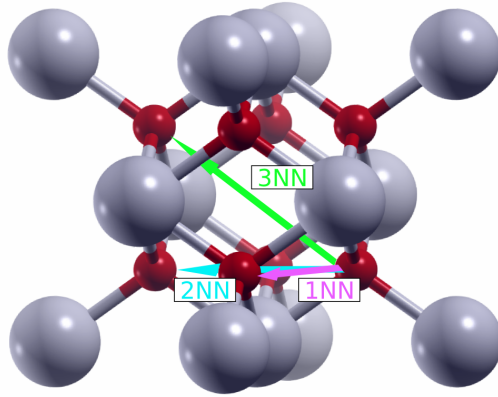


**Figure 7.1.:** The cubic fluorite phase of zirconia. The pathways for oxygen ion migration are shown as arrows. The three arrows indicate the possible jump processes to the nearest [1NN (purple)] location and to the next nearest ones [2NN (teal)], [3NN (green)]. A vacancy has to be present at the final position for any of these jumps to take place. (grey: zirconium, red: oxygen) [48]

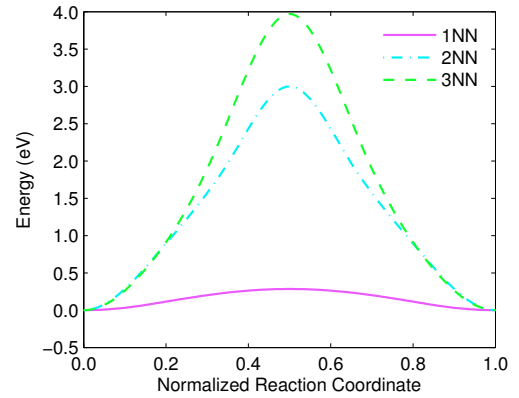


**Figure 7.2.:** The energies along the three different oxygen ion jump pathways in zirconia calculated in a lattice without external strain. The 2NN and 3NN pathways have a considerably larger migration barrier and can thus be neglected.

To avoid any correlation effects between the vacancy and other defects a migration process in pure zirconia with only one vacancy in the numerical cell is investigated at first. Since the effect of the yttrium doping or vacancy-vacancy interactions is neglected, it is possible to investigate the pure strain effect on the height of the migration barrier. To simulate yttrium content in the crystal without having it in the direct neighborhood of the jump process, the number of electrons in the system is adapted to double positively charge the vacancy as discussed in the previous chapter.

In the cubic phase of zirconia there are three direct oxygen ion migration pathways possible as shown in Fig 7.1. Typically only the Nearest Neighbor (1NN) jump from one tetrahedron to a neighboring one is considered. This is based on the assumption that the 2NN and the 3NN pathway could be neglected. This is investigated by calculating the MEP between those configurations. The results, as shown in Fig. 7.2, (as well as the strain dependence of these jump processes discussed in the next subsection and as presented in Fig. 7.5) justify this assumption: The migration barriers (about 3 eV for 2NN and 4 eV for 3NN, respectively) are much higher than that of the 1NN jump and can be neglected due to the exponential dependence of the conductivity on the height of the migration barrier.

The strain is introduced by calculating the migration barrier along the 1NN pathway for different lattice constants. The strain, if applied isotropically to the system, keeps the

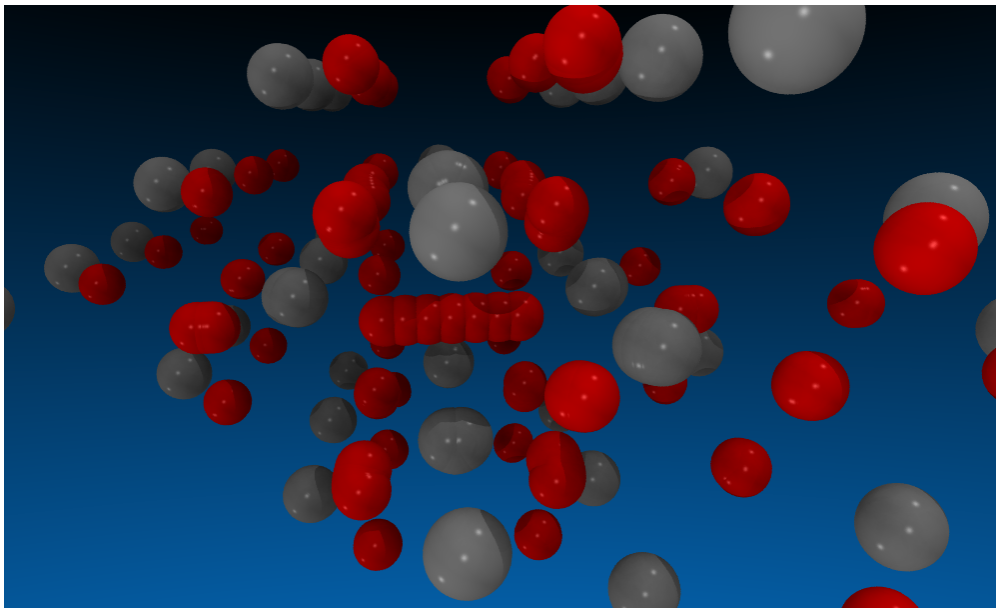


**Figure 7.3.:** Trajectory of the NN jump in pure zirconia at the equilibrium lattice constant. (grey: zirconium, red: oxygen)

cell shape cubic. The factor  $\sigma$  scaling the lattice constant in the DFT calculation defines the strain in the system, where  $\sigma = 1$  denotes the strain-free case. In this symmetrical jump, the maximum energy is, as expected, reached when the oxygen stands at the brink of two tetrahedrons being exactly located between two zirconium ions - these two ions will be referred to as the “gate ions”. As will be described below, only for very large strains this is not the case any more.

#### 7.1.1.2. DFT Results

The lattice constant of pure zirconia – with one vacancy in the system – was determined as 5.106 Å, which is very close to the experimental value [80] of 5.090 Å. Test-calculations have been executed to see the effect of an on-site Coulomb correction on the equilibrium lattice constant. With  $U = 6$  eV and  $J = 1$  eV the lattice constant increased to 5.3 Å, which deviates much stronger from the experimental value than the GGA-PBE results. This encouraged the application of the GGA-PBE formalism, which has the advantage of avoiding further parameters like  $U$  and  $J$ .

First, the migration barrier at zero pressure is computed to be  $\Delta E = 0.3$  eV, if a cubic lattice is enforced. In literature the migration barrier of YSZ is typically computed to be about 0.6 eV in DFT [90, 92]. This difference can be accounted for by considering that zirconia is not stable in the cubic phase at zero pressure. For small expansions of about  $\sigma \geq 1.01$  a tetragonally distorted configuration becomes more stable than the cubic one. Using an expanded lattices and permitting the oxygen ions to relax away from their perfect lattice sites, migration barriers of about 0.6 eV has been observed, as well. In

fact, Krishnamurthy et al. [92] reported that they observed a random displacement of oxygen ions away from their perfect fluorite sites in the 9YSZ system, which in average preserves the cubic lattice. This explains the difference in the determined migration barrier. In this chapter only the perfect cubic lattice is investigated, which is metastable for  $\sigma \geq 1.01$  in the pure zirconium cell.

As noted before, to gain a deeper understanding of the ionic motion in YSZ, it has to be observed under extreme conditions. Therefore, the strain dependence of the migration barrier up to very strong compressions is investigated here, leading to expected behavior for small strains and to an unexpected behavior at very high strains. The computations are executed in the following manner: Starting from the equilibrium lattice constant, the migration barrier is determined for compression and for expansion. For each strain value the initial and final position is first relaxed until the maximum force is smaller than  $1 \text{ meV}/\text{\AA}$  and subsequently the height of the migration barrier is determined with the NEB method. The trajectories of the oxygen ion in the strain-free case can be seen in Fig. 7.3.

As a result of the strain dependent DFT calculations (cf. Fig. 7.4), it was found that the migration barrier decreases with expansive strain in the neighborhood of the strain-free state, as expected from experiments. However, under compression the height of the migration barrier is no monotonically increasing function of the strain, but it rather has a maximum at a specific compression value ( $\sigma = 0.91$ ). For higher compressions the migration barrier decreases again until it vanishes. While it is intuitively clear, that the migration barrier decreases for expansion, it was not expected to find a decrease at high compression as well. VASP also provides the external pressure acting on the computational cell. Hence, the pressure required to observe the barrier maximum of this specific jump in zirconia was determined as 130 GPa. Such boundary conditions could be achieved by using a diamond anvil cell (DAC), in which pressures of up to 300 GPa can be produced [93]. To explain this unexpected behavior at strong compressions, DFT cannot help any further than just observing it. Therefore, a different approach was necessary to give an explanation. A model including the direct vicinity of the jump process and strain effects from the lattice is set up giving a possible origin of this behavior.

It has further been investigated how the vicinity of a jumping oxygen ion affects the height of the migration barrier. Since the gate ions move most to let the oxygen pass, it is first looked into their effect. To find out how costly it is to displace these two ions to the distance necessary for the oxygen ion to hop, they are fixed to the barrier-position distance and the rest of the lattice is relaxed. The energy changed by only 11 meV at  $\sigma = 1$ , by 0.4 eV at  $\sigma = 0.914$ , which corresponds to the maximal height of the migration barrier, and 0.24 eV at  $\sigma = 0.866$ . This indicates, that this contribution to the barrier at low compressions is negligible and the barrier only results from the movement of the oxygen ions itself. This originates on the one hand from the breaking of the bonds to the zirconium ions opposite to the jump direction, on the other hand from approaching the gate ions. At higher compressions this contribution to the barrier height is stronger. These types of computations are repeated for the special case of one yttrium gate ion, which are discussed in subsection 7.2.3.

The effect of further ion sets is investigated by constrained NEB, i.e. a NEB calculation

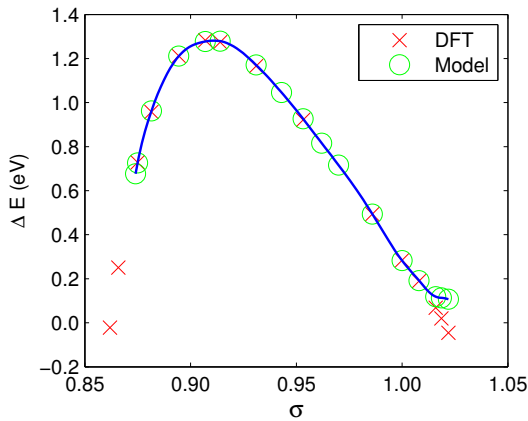


**Figure 7.4.:** Height of the migration barrier as a function of the strain  $\sigma$ . The blue line shows a spline interpolation of the model data. The model agrees over a wide strain range with the DFT results. For  $\sigma < 0.87$  the model is not valid any more and deviates for  $\sigma > 1.008$  (see text for discussion).

with a subset of ions fixed. Details about these constrained NEB calculations are given in the appendix A.3. Two findings can be deduced from these calculations. First, the migration barrier is a very sensitive quantity, which changes strongly when fixing presumably unimportant or distant ions; typically 0.1 eV per fixed ion at  $\sigma = 0.914$  and 0.4 eV per fixed ion at  $\sigma = 0.86$ . Considering, that the migration barrier results from a small difference of large energies (the total energy of the supercell changes by 200 eV in the overall strain range, while the migration barrier changes maximal only by about 1.3 eV) this sensitivity is not surprising. It shows that the jump process is a complex one being affected by not only near, but also more distant ions. Such sensitivity has been reported before [90, 92]. Secondly, it turns out, that the migration barrier maximum does not vanish if ions are prevented

from relaxing, but it rather shifts to stronger compression values, and at the same time increases the migration barrier height at all strains.

The migration barrier becomes negative in the regime of small  $\sigma$  values, and it has to be pointed out, that for negative migration barriers the system is not in the ground-state at initial and final position. Therefore, the system would deviate away from this configuration. However, these states are meta-stable and it is possible to determine a “negative migration barrier” in the same manner as for positive ones. Although they do not have a deeper physical meaning, they show a consistent behavior of the  $\Delta E(\sigma)$  curve even for negative migration barriers.

For  $\sigma \geq 1.01$  the lattice becomes sparsely filled leading to the coexistence of tetragonal and cubic phase. For  $\sigma \geq 1.01$  the tetragonal phase is more stable, but the cubic phase is still metastable permitting the calculation of the barrier analog to the calculation of “negative barriers”.

In order to check, whether the migration barriers of the 2NN and 3NN jumps can become small enough, to compete with the 1NN jump under strong compressive strain, their strain dependence has also been determined. However, these calculations, although showing the same qualitative behavior as the comprehensively investigated 1NN jump, are overall at least 1 – 2 eV higher. The 2NN barrier has a maximum of 3.75 eV and the 3NN barrier of 4.35 eV (cf. Fig. 7.5). Thus, the 2NN and the 3NN jump can also be neglected at higher compressions.

To validate that the strain dependence is not an artifact of boundary conditions, further computations of the barrier at various strain values in a larger  $4 \times 4 \times 4$  supercell

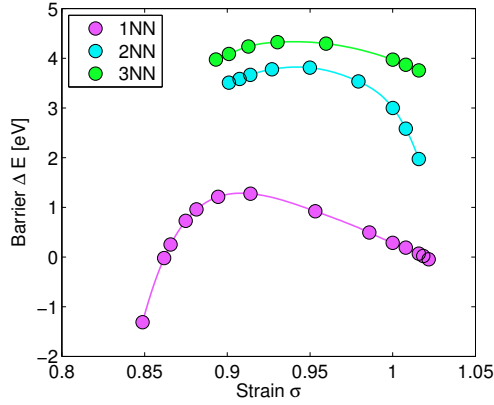


**Figure 7.5.:** Plot of the strain dependent barrier of the three possible jump directions in cubic zirconia. The markers are DFT calculations and the lines are cubic splines as a guide to the eye. This plotting type is used in all  $\Delta E(\sigma)$  plots in this thesis.

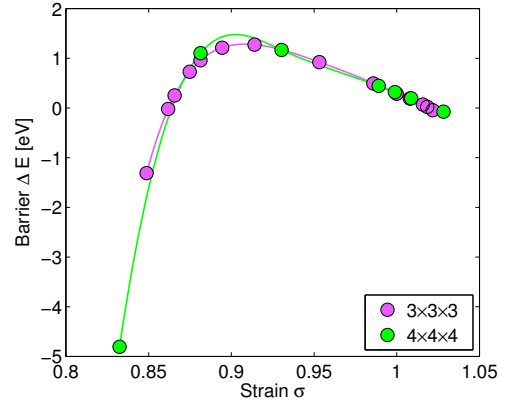


**Figure 7.6.:** Comparison of the strain dependence of the barrier  $\Delta E$  between the  $3 \times 3 \times 3$  supercell and a  $4 \times 4 \times 4$  supercell.

have been conducted and plotted together with the results of the previous calculation in the  $3 \times 3 \times 3$  supercell (Fig. 7.6). The curves fit over the complete strain range under consideration very well showing a sufficient convergence regarding the supercell size.

Another very important comparison can be done in the large supercell. It was assumed, that a supercell of pure zirconium with one vacancy inside is a model system for YSZ in case the nearest yttrium ions are far away from the jumping oxygen ion. This is tested by comparing the migration barrier in the  $4 \times 4 \times 4$  supercell with a lattice constant of  $a = 5.05 \text{ \AA}$ , with two yttrium ions having replaced zirconium ions to the corresponding migration barrier from the large zirconium cell in Fig. 7.6. The barrier in  $4 \times 4 \times 4$  supercell of pure zirconia with the homogeneous background-charge at this lattice constant ( $\sigma = 0.989$ ) is  $\Delta E_{\text{charge}} = 0.4435 \text{ eV}$ , while the barrier in the system with actual yttrium content is  $\Delta E_{\text{YSZ}} = 0.4417 \text{ eV}$ , which is up to a negligible difference of  $1.7 \text{ meV}$  the same. This shows, that at least for migration barriers, the pure zirconia system with charged vacancies is a very good model system for YSZ.

The DFT computations give the maximum of the migration barrier as a function of  $\sigma$ , but to gain further understanding a model is set up, which reproduces this unanticipated behavior and provides insight into the physics behind. In the next section this model will be described and its results discussed.

## 7.1.2. Analytic Approach

### 7.1.2.1. Model Description

Because of the Born Oppenheimer theorem (c.f. Eq. 3.3) the energy of the DFT functional  $E_{DFT}$  is at the same time the potential energy  $V$  of the  $N$  ions

$$V(r_1, r_2, \dots, r_{3N}) = E_{DFT}(r_1, r_2, \dots, r_{3N}). \quad (7.1)$$

This potential is not only complicated, but the changes of the ionic positions also become complicated as soon as one ion is moving towards a vacancy. The reason is the long-range interaction between the various ions. As noted above, even when only fixing the positions of ions not in the immediate neighborhood of the moving one, the migration barrier will change considerably – by 40% or more.

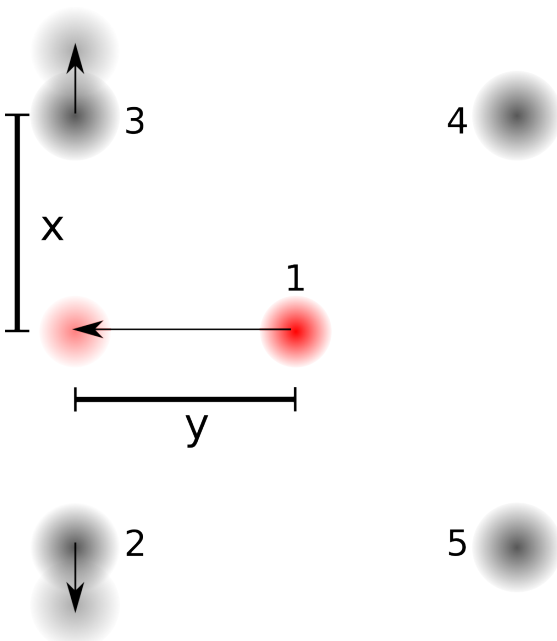


**Figure 7.7.:** Sketch of the atomic configuration considered in the model (shown two dimensionally). Ion 1 (red) is the oxygen ion, while the ions 2-5 (grey) denote the zirconium ions at the corners of the tetrahedron. The dynamics considered in modeling the jump process is indicated by the arrows. The origin of  $x$  and  $y$  is the center of mass of the two zirconium ions 2 and 3.

This complicated behavior is contrasted with the conjecture that in a motion to a vacancy just two coordinates seem to be essential, one (indicated by  $y$  in Fig. 7.7) being the coordinate of the oxygen ion in the direction of the vacancy, the other (indicated by  $x$  in Fig. 7.7) being half the distance of the two zirconium ions between which the oxygen ion will pass. However, when all the other coordinates are of marginal importance they can be integrated out in phase space. Because of the exponential dependence this amounts to the replacement

$$V_m(x, y) = \min_{r_3 \dots r_{3N}} V(x, y, r_3 \dots r_{3N}), \quad (7.2)$$

by which the problem has in fact been reduced to the supposed relevant coordinates. It will turn out that in contrast to the long range potential  $V$  the potential  $V_m$  can be represented by a sum of short ranged Lennard Jones potentials.

Next, one can see that the coordinates  $(x, y)$  are in fact the relevant ones and the potential  $V_m(x, y)$  the relevant potential. Indeed, if  $x$  and  $y$  are kept fixed at the saddle point values, all other variables relaxing from the initial positions should also take their saddle point positions. This is in fact the case. Consequently, the NEB

method applied to determining the saddle point in this two dimensional problem will not only lead to the correct initial and saddle point positions, but also to the correct energies at these points, and consequently to the correct migration barrier as well.

It is therefore tempting to extract the physics out of the potential  $V_m$  by constructing a simple model with interactions fitting  $V_m$ . This will be described in the following.

When an oxygen ion is moving to a vacancy, a displacement of many ions takes place due to the *long range* character of  $V$ . However, these displacements are expected to lead to a screening with the result that  $V_m$  is an effective *short range* potential. This will be demonstrated by replacing  $V_m$  with LJ potentials and taking into account only the direct neighborhood of the moving oxygen ion as shown in Fig. 7.7. This neighborhood consists of 4  $Zr^{4+}$  ions forming the corners of a tetrahedron with the  $O^{2-}$  ion initially located in the center. The interaction between zirconium and oxygen is represented by a LJ potential with constant parameters  $\epsilon_{Zr-O}$  and  $r_{Zr-O}$ . Furthermore, the motion of the  $Zr^{4+}$  ions 4 and 5 in Fig. 7.7 is neglected being small compared to the motion of the  $Zr^{4+}$  ions 2 and 3. Their motion is being exposed to other ions close by, which is taken care of with the following assumptions: These  $Zr^{4+}$  ions can move in  $x$ -direction only, and their LJ interaction depends on  $\sigma$ . In the DFT calculations  $\sigma$  was introduced as the scaling factor for the lattice constant, thus, scaling the side-length of the tetrahedron in the same linear way is a natural choice to simulate compression and expansion in the model. This length is chosen to be the in  $\sigma$  linearized DFT distances of the  $Zr^{4+}$  ions. The model potential  $V_M(x, y)$  is constructed in the following way:

$$\begin{aligned}
V_M(x, y) = & \\
& 2\epsilon_{Zr-O} \left( \left( \frac{r_{Zr-O}}{\sqrt{x^2+y^2}} \right)^{12} - 2 \left( \frac{r_{Zr-O}}{\sqrt{x^2+y^2}} \right)^6 \right) \\
& + 2\epsilon_{Zr-O} \left( \left( \frac{r_{Zr-O}}{\sqrt{x_i^2+(2y_i-y)^2}} \right)^{12} - 2 \left( \frac{r_{Zr-O}}{\sqrt{x_i^2+(2y_i-y)^2}} \right)^6 \right) \\
& + \epsilon_{Zr-Zr}(\sigma) \left( \left( \frac{r_{Zr-Zr}(\sigma)}{2x} \right)^{12} - 2 \left( \frac{r_{Zr-Zr}(\sigma)}{2x} \right)^6 \right),
\end{aligned} \tag{7.3}$$

with the initial coordinates  $(x_i, y_i)$ . Since the zirconium ions 4 and 5 do not move and the tetrahedron is symmetric, it is possible to express their distance to the oxygen ion by  $\sqrt{x_i^2 + (2y_i - y)^2}$ . The distance  $r_{Zr-O}$  is the equilibrium position of the  $Zr^{4+} - O^{2-}$  bond in the crystal. This can be determined from the corresponding distances in strain-free DFT calculations. Employing a radial distribution function the equilibrium distance can be determined as 2.198 Å, which conforms well to the findings reported by Li et al. [94]. The parameter  $\epsilon_{Zr-O}$  is fixed to  $\epsilon_{Zr-O} = 0.16$  eV. The values for  $r_{Zr-Zr}(\sigma)$  and  $\epsilon_{Zr-Zr}(\sigma)$  are chosen for each  $\sigma$  such that i) the initial configuration and ii) the resulting migration barrier fit to those obtained from DFT.  $\epsilon_{Zr-Zr}(\sigma)$ ,  $r_{Zr-Zr}(\sigma)$ , and  $\epsilon_{Zr-O}$  together reflect the highly complex impact of the surrounding lattice.

The energy of the model at the initial position is given by

$$E_i = V_M(x_i, y_i), \quad (7.4)$$

while the energy at the barrier position can analogously be described by

$$E_b = V_M(x_b, 0), \quad (7.5)$$

where the equilibrium distance at the barrier position  $x_b$  is determined by minimizing the energy with fixed  $y = 0$ .

With Eq. 7.4 and 7.5 the migration barrier

$$\Delta E_M(\sigma) = E_b(\sigma) - E_i(\sigma) \quad (7.6)$$

can be determined.

### 7.1.2.2. Model Results

In Fig. 7.4 the  $\Delta E(\sigma)$  curve resulting from this model is compared to the DFT values. By adapting  $r_{Zr-Zr}$  and  $\epsilon_{Zr-Zr}$  for each  $\sigma$  value, it is possible to fit the model curve to the DFT results over a wide range of strain. Below  $\sigma \approx 0.87$  the model cannot describe the situation correctly anymore, since the repulsion of the other ions in the vicinity cannot be described anymore by adapting the LJ interaction between the  $Zr^{4+}$  ions. In addition, the model deviates from the DFT curve for  $\sigma > 1.008$ , which corresponds to the occurrence of the tetragonal phase in DFT (cf. Sec. 7.1.1.2).

In Fig. 7.8 the decomposed energies of the model are shown as a function of  $\sigma$ . Several extrema can be observed near  $\sigma = 0.95$ : The energy of the  $Zr^{4+} - Zr^{4+}$  interaction have both a minimum at the initial position  $E_i(Zr - Zr)$  and at the barrier position  $E_b(Zr - Zr)$ . A weak minimum can also be found in the initial energies of the  $Zr^{4+} - O^{2-}$  interactions,  $E_i(Zr_{2,3} - O)$  and  $E_i(Zr_{4,5} - O)$ .

On the other hand, at the barrier position the energy of the interaction between the oxygen ion and the zirconium ions 2 and 3  $E_b(Zr_{2,3} - O)$  has a maximum and a distinct decrease for  $\sigma < 0.93$ . The explanation for this unexpected behavior is an increasing distance  $x_b$  between the zirconium ions  $Zr_{2,3}^{4+}$  and the oxygen ion (cf. Fig. 7.7). This increase occurs with compression for  $\sigma < 0.93$  and has been verified in the DFT calculations.

At the barrier position, the energy of the interaction between the oxygen ion and the zirconium ions 4 and 5  $E_b(Zr_{4,5} - O)$  has no extremum at all, but decreases continuously with decreasing  $\sigma$ . This can easily be understood: This bond is always attracting and therefore its energy decreases under compression.

It becomes obvious that there are two main reasons for the migration barrier to decrease again at stronger compression, although the energy difference of the  $Zr^{4+} - Zr^{4+}$  bond rises: a) the initial position becomes more and more unfavorable, since all four  $Zr^{4+} - O^{2-}$  bonds are contracted and thus strongly increasing the energy of the initial oxygen position, whereas the energy at the barrier position increases not this strongly

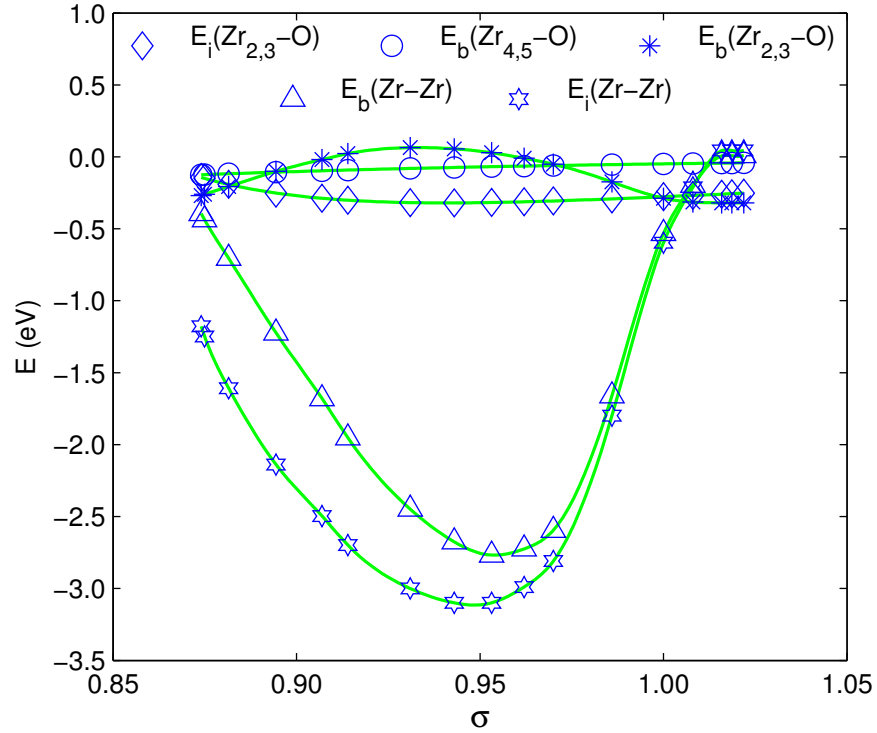


**Figure 7.8.:** Decomposed initial  $E_i$  and barrier  $E_b$  energies in the model as a function of  $\sigma$ . The energies  $E_{i,b}(Zr - Zr)$  incorporate the  $Zr^{4+} - Zr^{4+}$  interaction, the energies  $E_{i,b}(Zr_{2,3} - O)$  and  $E_{i,b}(Zr_{4,5} - O)$  incorporate the  $O^{2-}$  interaction with the corresponding  $Zr^{4+}$  ions. Note:  $E_i(Zr_{2,3} - O) = E_i(Zr_{4,5} - O)$ .

at large compressions. Furthermore, the potential acting on the zirconium ions in the x-direction is not very steep. This result, obtained from the DFT calculations, leads to a slow increase of the difference  $E_b(Zr - Zr) - E_i(Zr - Zr)$ . b) The distance between zirconium and oxygen increases again at strong compressions leading to a drop of the oxygen-zirconium repulsion at the barrier position. A further effect, which, however, is present at all compression values, is the decreasing energy  $E(Zr_{4,5} - O)$ . This effect diminishes the rise of  $\Delta E$ .

Taken a) and b) together, the model not only explains, why the 1NN barrier runs through a maximum of decreasing  $\sigma$ , but the model gives also a qualitative explanation why the barriers of the 2NN and 3NN jumps run through a maximum as well. In fact, these jumps start from the same initial states. As pointed out in a) the initial position becomes more and more unfavorable and hence maxima of these barriers as a function of  $\sigma$  are not surprising. Furthermore, the model also explains why the fixing of ion sets in DFT shifts the migration barrier maximum to stronger compression values. If the initial position is fully relaxed but one or more ions are fixed when calculating the migration

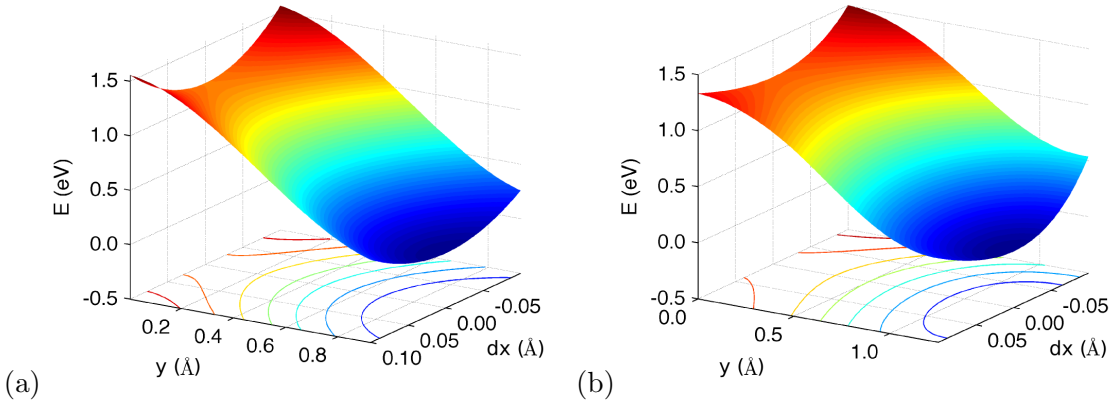


**Figure 7.9.:** The effective potential  $V_m(dx, y)$  at  $\sigma = 0.93$  in harmonic approximation from DFT is shown in (a) and  $V_M(dx, y)$  from the model in (b). The energy is plotted in dependence of  $y$  and  $dx$ , which is the deviation of the zirconium ions from their equilibrium distance for each  $y$ .

barrier, their missing relaxation gives rise to an additional energy contribution, which is compensated by the rising initial energy only after further compression.

In Fig. 7.9 the effective potential  $V_m(dx, y)$  of the DFT calculation in the harmonic approximation is compared with the potential  $V_M(dx, y)$  of the model. The energy is plotted in dependence of  $dx$  and  $y$ , where  $dx$  is the deviation from the reaction pathway in  $x$ -direction. For small deviations  $dx$ , the two potentials agree satisfactorily. This comparison shows that the model (Eq. 7.3) describes the effective potential of the DFT calculations well in the neighborhood of the reaction pathway.

The results in this section showed a new condition under which the migration barrier strongly decreases. This finding was observed in pure zirconia without any correlation effects, and has to be confirmed in more complex YSZ systems under consideration of correlation effects.

## 7.2. Strain dependence in YSZ

Up to this point only pure zirconia with appropriately charged vacancies has been considered. One can think of it as a YSZ system with no yttrium ions in the near of the jump process. This is a good approximation to investigate the general effect of strain on the migration barrier, but correlation effects due to the yttrium doping affect the profile of the curve (Fig. 7.4). In fact, it is well known that yttrium in the vicinity of the jump changes the barrier height intensely. Krishnamurthy et al. [92] reported that the migration barrier rises when one or both of the gate cations are yttrium  $E_{Zr-Zr} = 0.473$  eV,  $E_{Zr-Y} = 1.314$  eV and  $E_{Y-Y} = 2.017$  eV respectively. Pornpasertsuk et al. [90] computed the barrier change when any one or more of the cations in the direct neighbor of the initial and final position of the vacancy is yttrium. On some positions yttrium

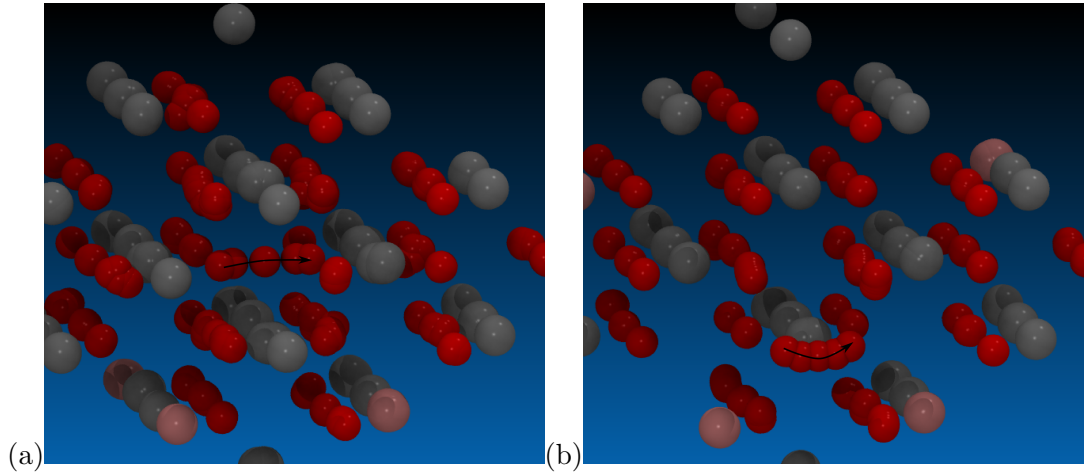


**Figure 7.10.:** Migration trajectories in 3.7%YSZ with a jump being symmetric in regard to the yttrium ions. In (a) only zirconium is in the direct neighborhood of the jump, and in (b) both the jumping oxygen ion and the vacancy has an yttrium ion as a nearest neighbor (the two gate ions are still zirconium) – the number of yttrium ions in the computational cell is two – the periodic boundary conditions make it look like four yttrium ions when all five frames of the MEP are plotted in one picture (grey: zirconium, red: oxygen, magenta: yttrium)

had a large effect, on some only a small one. However, this makes it obvious that an investigation of the strain dependent migration barrier with yttrium in the vicinity is required to complement the results of the previous section.

First, the effect of low yttrium doping is considered, where the two yttrium ions generating the vacancy are included. This amounts to an  $Y_2O_3$  doping of 3.7mol% in zirconium. 3.7YSZ is known as partly stabilized zirconia. Further results are presented including high-doped YSZ with 7.4mol% and the change of the barrier with yttrium as one of the gate ions.

### 7.2.1. Low-doped YSZ

In the low-doped YSZ system with one vacancy, the two yttrium ions are symmetrically arranged around the jump process as depicted in Fig. 7.10. In the first configuration (a) there is no yttrium in the direct vicinity of the jumping oxygen ion, while in (b) both the initial and final position of the vacancy have an yttrium ion as a nearest neighbor – but both gate ions are zirconium. In these two configurations the MEP is symmetric. Thus, the transition state is located exactly on half way from initial to final position, as in pure zirconium.

The addition of the larger yttrium ions induces an expansion of the lattice leading to an equilibrium lattice constant of  $a = 5.166 \text{ \AA}$ . In figure 7.11 the migration barrier in dependence of the compressive strain is plotted in the same manner as before – note that  $\sigma$  is always given in reference to the equilibrium lattice constant of the given system.

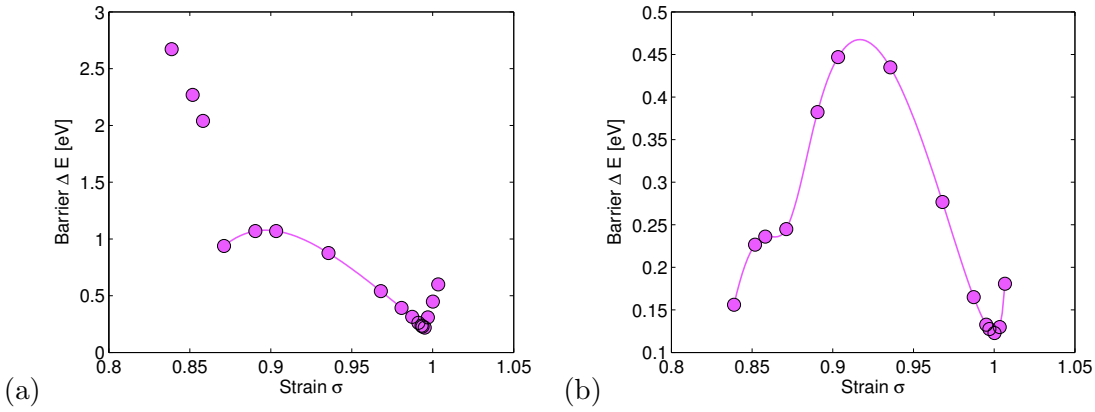


**Figure 7.11.:** Strain dependent migration barrier in 3.7%YSZ corresponding to the two jump processes depicted in Fig. 7.10

(a) is not one smooth curve as in the undoped system, it rather splits in three parts. The central part, from  $\sigma = 0.87$  to  $\sigma = 0.995$ , corresponds to the depicted jump process from configuration (a) and is in the cubic phase. This part agrees very well with the  $\Delta E(\sigma)$  curve of pure zirconia. For a lattice being more expanded than  $\sigma = 0.995$ , the

oxygen ions pass into the tetragonal phase as observed in pure zirconia. However, here the cubic phase is not metastable any more rendering it impossible to calculate the barrier of the metastable phase. Therefore, the plotted barrier values correspond to the oxygen migration starting and ending in the more stable tetragonal ground state, leading to an increase of the barrier with an expansion in the here considered strain domain. The emergence of the tetragonal phase in pure zirconia and 3.7YSZ is at similar lattice constants, in pure zirconia at  $a = 5.15 \text{ \AA}$  and in YSZ at  $a = 5.14 \text{ \AA}$ . As can be seen from Fig. 7.12, the preferred yttrium-vacancy distance is also strain dependent. This leads to an instability of the initial and final configuration in (a) below  $\sigma = 0.86$ . At this point the barrier to the yttrium near site totally vanished and the vacancy relaxes unhindered to the yttrium-ion near lattice site. This new configuration corresponds to the initial and final state of (b), while

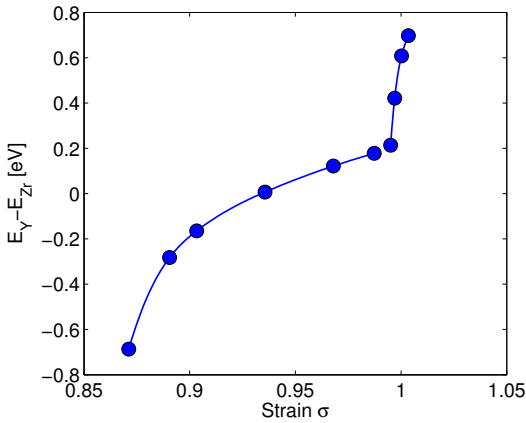


**Figure 7.12.:** Energy difference between the zirconium near vacancy and the yttrium near vacancy in dependence of strain (cf. Fig. 7.10). At  $\sigma < 0.86$  the zirconium near configuration goes over to the yttrium near configuration. At  $\sigma > 0.985$  the zirconium near configuration assumes the tetragonal phase, while the yttrium near one stays in the cubic one resulting in a much steeper change in energy.

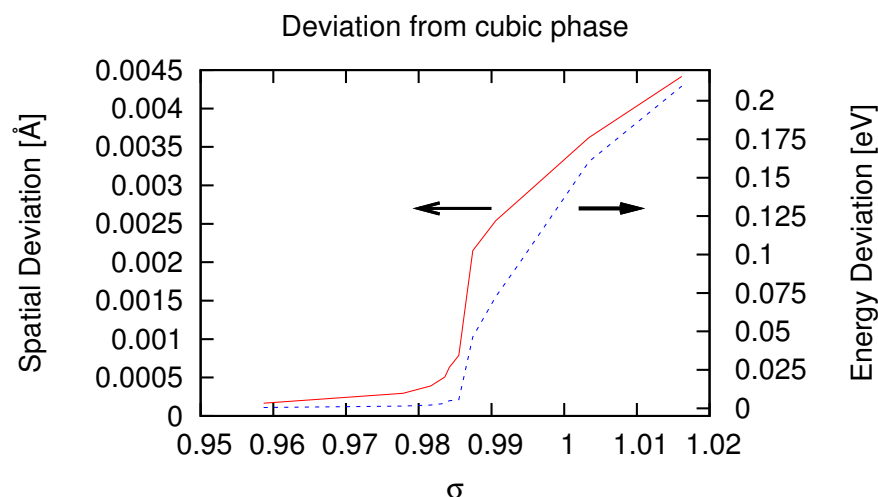


**Figure 7.13.:** Deviation from the cubic phase in the transition region of cubic to tetragonal phase. The spatial deviation is determined by the mean absolute deviation from the cubic lattice vectors. The energy-change in the relaxation process is assigned to the secondary y-axis.

still passing the transition state of (a). In fact, there are three oxygen ion jumps included in this process – or it can be considered as a triple jump of the vacancy. Since the yttrium near vacancy position is obviously more stable than the initial position of (a), and becomes even more stable with further compressions, the determined barrier increases.

To check whether the cubic phase is stable, or at least metastable, at a given unit-cell volume, the lattice vectors are relaxed with fixed internal degrees of freedom. The relaxation was executed for a specific number of steps to observe the change in total energy and the deviation of the cell vectors from the cubic ones. For this purpose, it is not necessary to reach convergence. These two quantities are nearly zero only, if the cubic phase is stable. In Fig. 7.13 both quantities rise at  $\sigma = 0.985$  coinciding with the occurrence of the increasing barrier in Fig. 7.10(a), corroborating the link between the barrier change and the stability of the cubic phase.

In case (b) of Fig. 7.10, in which the vacancy has an yttrium ion as a nearest neighbor both at the initial and final position, the qualitative profile of the curve is the same, but differs in details. The barrier maximum is already reached at  $\sigma = 0.917$  having a value of only  $\Delta E_{\max} = 0.468$  eV. The fact that the barrier is lower in such a configuration is already known [90] and now also carries over to the strain dependence. As in case (a), there are deviations from the uncorrelated strain dependence as observed in pure zirconia. Additionally, at strong compressions a shoulder in the curve appears that coincides with the instability domain in (a). This shoulder originates from detailed trajectories of the system.

For expansion of the lattice, an interesting phenomenon occurs (c.f. Fig. 7.14). While

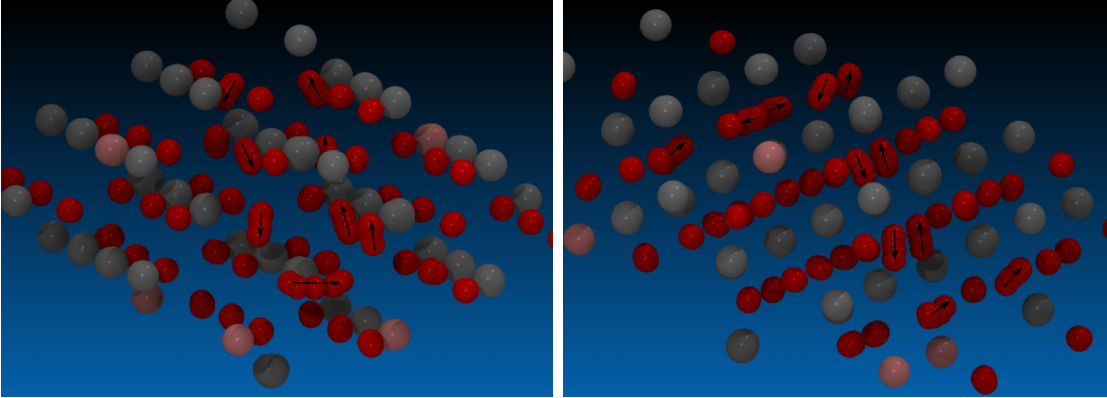


**Figure 7.14.:** Trajectories under expansive strain from two points of view. The arrows indicate the directions of motion. (grey: zirconium, red: oxygen, magenta: yttrium)

the adaption of the surrounding lattice to the jump has been observed before, the adaption shown in this case differs. Along two equivalent crystallographic directions oxygen ion rows move towards the vacancy and away from the oxygen ion, whereas the rest of the lattice moves little. Even more remarkable is the fact, that this displacement can only be observed in the directions without yttrium impurities. Due to symmetries, this displacement should be visible in four directions, but the yttrium ions prevent such a displacement past their locations. Such a deviation from the perfect fluorite sites resembles the tetragonal displacement of the oxygen ions. If this blocking effect also appears when phase transitions between cubic and tetragonal phases propagate through the lattice, a characteristic of yttrium is found, which inhibits the transition of YSZ into the cubic phase.

### 7.2.2. High-doped YSZ

A higher concentration of  $Y_2O_3$  doping in zirconia is achieved by substituting four zirconium ions by yttrium and removing two oxygen ions leaving two charged vacancies  $V_O^{2+}$  behind. The dopant concentration reaches 7.4 mol%, and by that fully stabilizes the cubic phase. Due to the further addition of yttrium, the equilibrium lattice constant increased to  $a = 5.188 \text{ \AA}$ . The second vacancy and the four zirconium ions in the system (c.f. Fig. 7.15) induce complex correlations and lead to an asymmetric potential along the MEP as shown in Fig. 7.16. In this case the barrier position of the MEP is no longer on the brink of the tetrahedron in between the gate ions, but is shifted towards the final state. In the case of the in Fig. 7.16 depicted MEP, the barrier position is shifted to a smaller vacancy-vacancy distance. However, from the strain dependence it can be seen that this changes under compression, and the vacancies start to attract each other below  $\sigma = 0.88$ . In this strain domain the backwards jump faces a higher barrier than the forward jump. From the qualitative progress of the  $\Delta E(\sigma)$  curves in Fig. 7.16 it can be deduced that this effect is purely based on the vacancy-vacancy interaction. The forward jump (where the vacancy-vacancy distance is larger) keeps dropping under

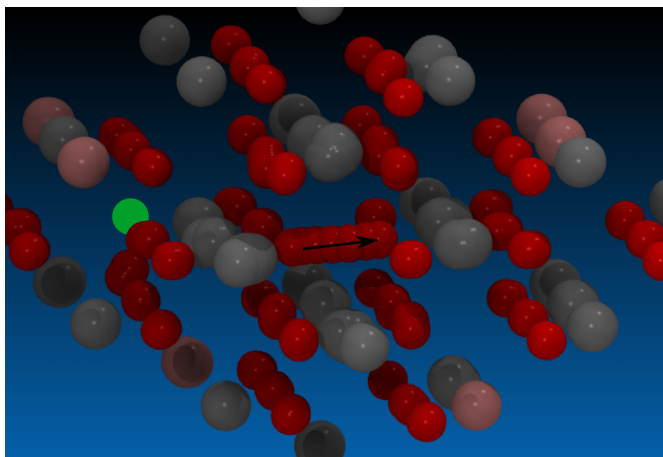


**Figure 7.15.:** Jump trajectories in the 7.4YSZ. The additional vacancy is indicated by a green sphere. (grey: zirconium, red: oxygen, magenta: yttrium)

compression, while the backward jump starts to rise again for  $\sigma < 0.89$ .

For strain values larger than  $\sigma = 0.98$ , the single jump shown in Fig. 7.15 is not stable any more, and a double jump including the secondary vacancy takes place changing the barrier and its strain dependence significantly.

From the results of the fully stabilized zirconia investigations it can basically be concluded that, although the correlation effects are large, the strain dependence of the migration barrier is qualitatively identical to the one in pure zirconia. As a difference, the maximum of the barrier is here already reached at  $\sigma = 0.93$  for the forward jump and  $\sigma = 0.92$  for the backward jump shifting the barrier maximum to a lower compressive pressure of about 71.5 GPa. This implies that the applied pressure necessary to observe the dropping of the barrier does not need to be that high in an experiment as the calculations in pure zirconia predicted. Although, this jump is just another example, and cannot represent all barriers in a complex system, its occurrence in 8YSZ is higher than the one from pure zirconia.

### 7.2.3. Yttrium at the barrier position

At last, the configuration with one yttrium gate-ion is investigated. On the one hand, it can be expected that the barrier is much higher than in the case of two zirconium gate ions. On the other hand, due to the sensibility of the  $\Delta E(\sigma)$  maximum to small changes in the neighborhood, a shift of the maximum to smaller  $\sigma$  values will probably occur. The system at hand is again a 3.7mol% yttria doped zirconia compound with two yttrium defects and one oxygen vacancy assembled to induce a symmetric jump. In Fig. 7.17 the trajectories passing the yttrium at three different strain values are shown. In (a) the effect of the inhibited oxygen displacement due to the yttrium dopant can be observed again. The four oxygen ions being direct neighbors to the initial and final position of the vacancy and of the zirconium gate ion deviate much stronger from their

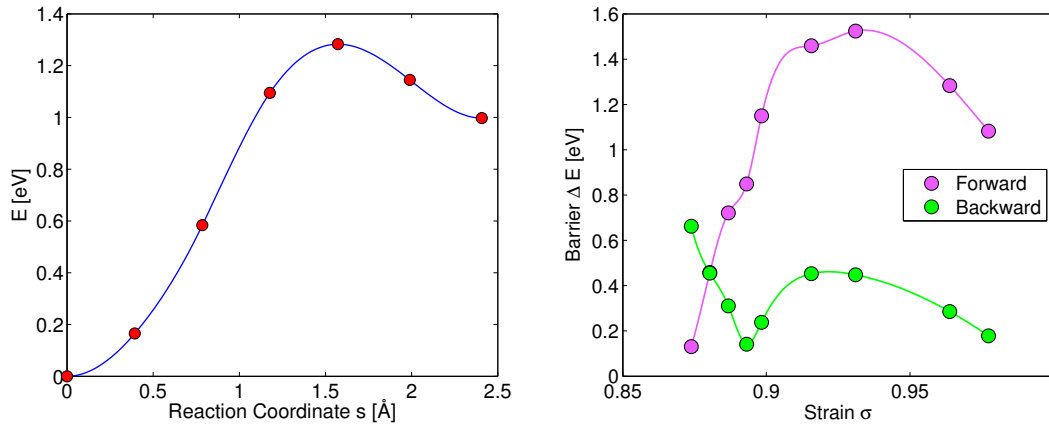


**Figure 7.16.:** The potential along the pathway ( $\sigma = 0.96$ ) shown in Fig. 7.15 (left) and the barrier height in dependence of the strain in the 7.4YSZ system (right). Due to the second vacancy the jump is asymmetric.

initial position than the four corresponding oxygen ions near the yttrium defect. In (b) it becomes obvious that the jumping oxygen ion avoids the position directly between the gate ions. Furthermore, it can be seen that the yttrium gate ion has to avoid the oxygen ion in a more sweeping motion than the zirconium gate-ion. This can be accounted for by the larger ionic radius of  $Y$  in contrast to  $Zr$ . In (c) this effect becomes even more pronounced, while the oxygen ion directly passes through the gate ions. The strain dependence of the barrier for this jump process (Fig. 7.18) shows two domains, while the barrier is overall higher than in the previously discussed cases. The plot looks like a superposition of two  $\Delta E(\sigma)$  curves, a lower one starting (in this plot) from  $\sigma = 1$

$\sigma$	$E_{\text{init}} - E_{\text{fixed}}$
1.0	0.065 eV
0.9	0.317 eV
0.88	1.127 eV
0.84	<i>barrier</i>

**Table 7.1.:** Gate-ion contribution to the migration barrier for one yttrium gate-ion. The statement *barrier* denotes a relaxation of the system to the barrier position.

exactly through the gate ions.

The effect of yttrium as one of the gate ions is further investigated by fixing the

assuming a pseudo<sup>2</sup> maximum at about  $\sigma = 0.9$ , and a second curve being mounted on the lower one starting at about  $\sigma = 0.89$  and assuming a real maximum at  $\sigma = 0.85$ . An explanation for these two domains is already given: In the domain  $\sigma > 0.89$  the oxygen ion moves from the initial to the final position by avoiding the position directly between the gate ions. Below this strain value, the oxygen ion is forced by the contracting lattice to take the direct trajectory passing ex-

<sup>2</sup>It is mathematically no maximum, since the curve only drop into one direction and passing into a plateau on the other one. But deducing from the previously investigated  $\Delta E(\sigma)$  curves a maximum would be expected at this strain value.

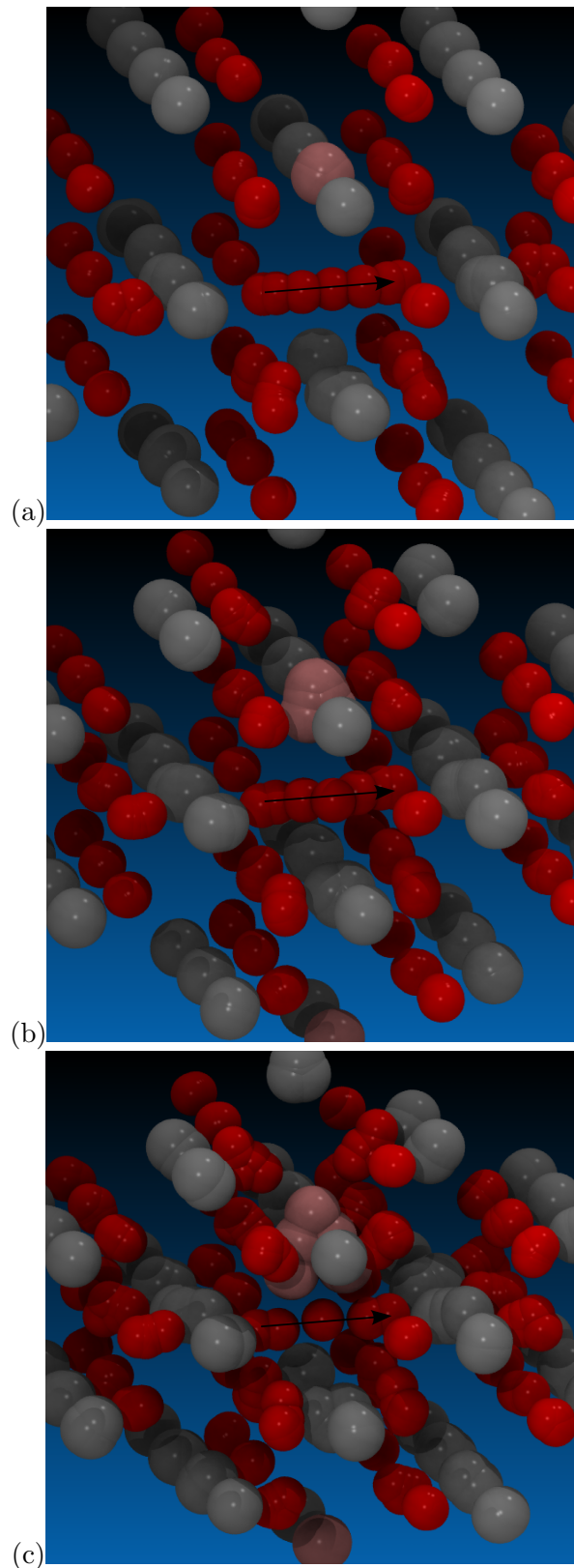


**Figure 7.17.:** Migration trajectories at three different strain values in YSZ with one of the gate ions being yttrium. (a)  $\sigma = 1$ , (b)  $\sigma = 0.88$  and (c)  $\sigma = 0.85$ . (grey: zirconium, red: oxygen, magenta: yttrium)

gate ions to the barrier distance and letting the rest of the lattice relax (comparable calculations with zirconium gate-ions have been presented in subsection 7.1.1.2). In this way the contribution of the gate-ions to the migration barrier can be estimated. Here, it is especially of interest how the contribution changes in the different domains of  $\Delta E(\sigma)$ . The results (Tab. 7.1) show a behavior similar to the one in pure zirconia

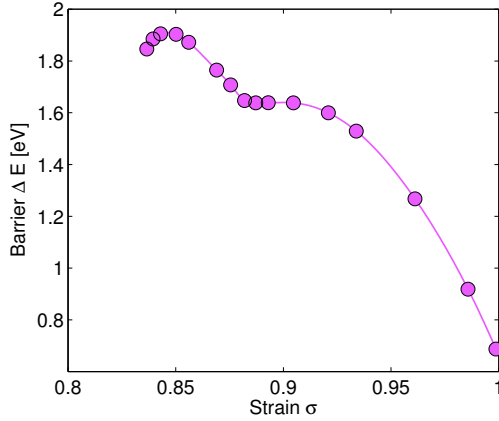


**Figure 7.18.:** Strain dependent migration barrier of oxygen ions when passing one yttrium and one zirconium ion.

for small compressions. The contribution is with 65 meV at  $\sigma = 1$  larger than in pure zirconia, but still very small. Also at  $\sigma = 0.9$  the contribution is comparable. This spans the whole lower domain of the  $\Delta E(\sigma)$  curve. It should be noted that in this domain the oxygen ion does not pass directly through the gate ions and by that the gate ions need to move less in the jump and thus have a relatively small contribution. At  $\sigma = 0.88$  the oxygen ion passes directly through the gate ions reflecting the sudden increase of the gate ion contribution. In fact, the total barrier at this strain is only 0.6 eV higher than the contribution of the gate ions. For strains values lower than  $\sigma = 0.84$  the system completely relaxes back to the barrier configuration. Hence, the gate-ions' distance fully determines the system.

### 7.3. Strain dependence in SSZ

As pointed out in Chapter 6, SSZ is one of the best electrolyte materials for SOFC applications. It has a high conductivity and is mechanically and chemically very stable. Obviously, it is very interesting to find out how the strain dependence looks like in comparison to YSZ. One of the reasons why the conductivity of YSZ decreases with high dopant concentration is the increase of yttrium induced high barrier numbers. It was shown before that the strain dependence of the oxygen jump passing the yttrium defect differs also significantly from the one in pure zirconia, or when passing only zirconium in YSZ. For that reason, the calculations from subsection 7.2.3 are repeated with yttrium replaced by scandium. The equilibrium lattice constant in 3.7SSZ is  $a = 5.133 \text{ \AA}$  being smaller than the corresponding value in YSZ ( $a = 5.166 \text{ \AA}$ ), as expected from the smaller dopant ion radius. In Fig. 7.19 the trajectories are depicted for three different strains. Comparing YSZ with SSZ just from the looks of the ionic motion, one can already see big differences. In the SSZ, the oxygen always moves directly along the straight pathway through the two gate ions. There is no difference between the trajectories of the two gate ions in (a) and (b). In (c) the scandium ion moves even less than the zirconium

ion. Looking at the strain dependence of this barrier (Fig. 7.20) one can recognize an undisturbed curve comparable to the one in pure zirconia, in the strain domain under consideration. At second glance, one can see that the maximal barrier is slightly lower than in pure zirconia.

Secondly, the configuration from Fig. 7.10(b) is repeated with scandium replacing the yttrium. Both the strain dependent barrier and the strain dependent energy difference between the scandium near and the scandium far vacancy position are depicted in Fig. 7.21. The  $\Delta E(\sigma)$  curve of this system exhibits larger barriers than the analog configuration in YSZ, but smaller barriers than in pure zirconia. Furthermore, the scandium near vacancy is more stable for vacancy at all strain values, showing a pure attractive behavior of vacancies and scandium increasing linearly in the energy difference.

## 7.4. Discussion of strain induced effects in doped zirconia

From this chapter it becomes obvious, that strain has a major impact on the oxygen migration barriers and the correlation effects in doped zirconia. The vacancy-dopant interaction is strongly strain dependent. In Fig. 7.12 the energy difference between the yttrium near vacancy (b) and the yttrium far vacancy (a) is plotted showing that the yttrium far configuration is more stable at low pressures and the yttrium near configuration is more stable at higher compressions ( $\sigma < 0.93$ ). That vacancies prefer 2NN positions to yttrium in YSZ at ambient pressure has been reported repeatedly before (e.g. [90] and [95]), the fact that this changes under compression is, however, new.

In SSZ this dopant-vacancy interaction is attracting at all compressions – extrapolating the data to expansion one finds that the 1NN distance becomes unfavorable at a slight expansion ( $\sigma = 1.01$ ) of the lattice. Since scandium has nearly the same ionic radius as zirconium, and the tendency to attract vacancies increases for both dopants, it can be concluded that the origin for the vacancy attraction is the different charge of the dopant ions. This can already be understood by electrostatics, since the positively charged vacancy  $V^{2+}$  is obviously less repelled by  $Y^{3+}/Sc^{3+}$  than from  $Zr^{4+}$ . However, in the case of yttrium another effect overlays the charge effect, the geometric disturbance of the lattice due to the larger yttrium-ion size. As can be seen from Fig. 7.14, yttrium blocks the motion and relaxation of the surrounding ions, thus, yttrium hinders the response of the direct vicinity to the vacancy. From this, one can deduce that in this way, the vacancy near ions cannot assume their optimal position leading to higher energies when the vacancy is 1NN to the yttrium. Under compression the charge effect dominates and the yttrium near lattice site becomes more favorable for the vacancy.

Under sufficient compression, the dopant reduced the 1NN energy and the barrier to the next lattice site that strongly, that the adjacent positions become completely unstable and the vacancy cannot move to the next lattice site any more. When attempting a double jump to the second next lattice site, the barrier to overcome is the sum of the trapping energy – extrapolation of the data in Fig. 7.12 or 7.21(a) to stronger compressions – and the usual barrier in zirconia at this strain value from Fig. 7.4. This barrier can also directly be seen from strain values  $\sigma < 0.86$  in Fig. 7.11(a) and is about

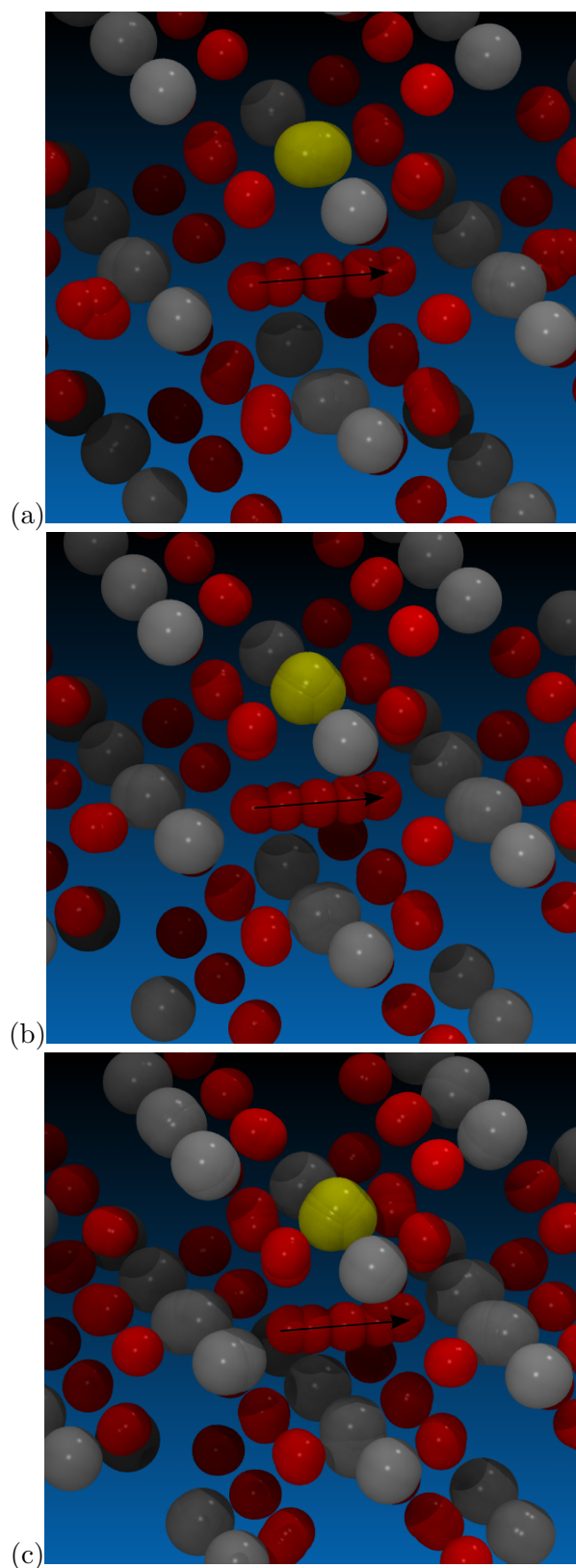


**Figure 7.19.:** Trajectories at three different strain values in the system with an scandium ion at the barrier. (a)  $\sigma = 1$ , (b)  $\sigma = 0.91$  and (c)  $\sigma = 0.86$ . (grey: zirconium, red: oxygen, yellow: scandium)

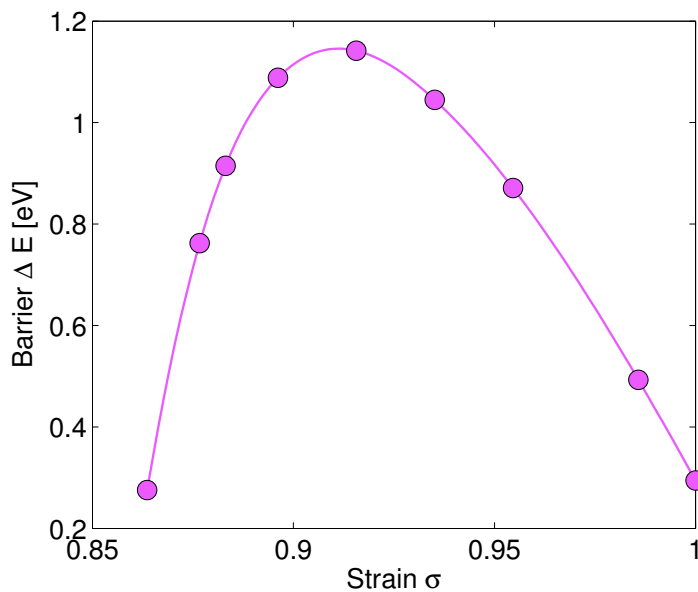


**Figure 7.20.:** Strain dependent migration barrier of oxygen ions when passing one scandium and one zirconium ion.

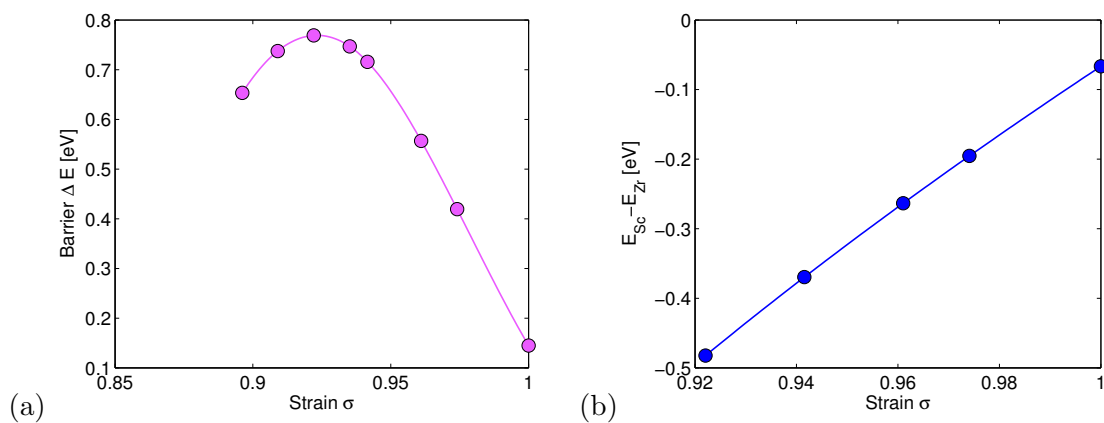


**Figure 7.21.:** (a) Strain dependent barrier corresponding the configuration in Fig. 7.10(b) with scandium replacing the yttrium. (b) Energy difference between the scandium near and the scandium far vacancy position.

2eV high, which makes an escape practically impossible. Since the energy of lattice sites around dopants are reduced for vacancies, only jumps to another site of the same kind are possible. This could be the direct low-barrier jump seen in 7.11(b). But also another jump is imaginable. If the second next lattice site has again a dopant ion as nearest neighbor, a double jump to this site is symmetric again having the transition state at the lattice site in between. However, the resulting barrier is equal to trapping energy of the dopant leading to a linearly increasing barrier (Fig. 7.12 or 7.21(a)).

This consideration and the previous ones about single jump barriers reveal that it is not meaningful to look only into one type of jump. It is important to find the relevant barrier in a given system. This does not need to be the highest barrier in the system, which, in the case of YSZ, would be the one passing yttrium, nor does it have to be the lowest one, which would be the one from one yttrium near site to another of the same type. As long as the yttrium concentration is low, the yttrium induced high barrier number is low and by that has only a minor impact on the overall conductivity, since the ions will always find a way around them. The barrier connected to a jump without yttrium directly nearby is then the relevant one. However, if the concentration is very high, this yttrium barrier becomes the relevant one. The same holds true for the smallest barrier. When the yttrium concentration is low, the number of such barriers can be neglected, and they do not contribute to a higher conductivity. However, in an intermediate concentration, the number of such jumps could be high enough to contribute strongly to the overall conductivity. In SSZ the question for the relevant barrier seems to have a more straightforward answer, since the geometric effect is not present and the charge effect is small at ambient pressure. Thus, for  $\sigma$  around one, the unperturbed zirconium jump is the relevant one, but under compression the scandium ions start to attract the vacancies significantly, preventing ionic motion at low scandium concentrations and increasing the conductivity at high scandium concentration.

These considerations referred only to the correlation effects induced by defects in the cation lattice. Additionally there are correlation effects between vacancies. Since vacancies are mobile, the repulsion observed in Fig. 7.16 does not imply a permanent blockage of the pathway, and is, therefore, not the relevant barrier. Just assuming the zirconia barrier as the relevant one is an oversimplification if the concentration of vacancies is high, and more sophisticated approaches are needed. This will be picked up again in the next chapter.

This concludes this chapter about the strain dependence of the migration barrier of oxygen ions in zirconia, YSZ and SSZ. It has been shown that the barrier decreases in principle with expansion, but in many cases the cubic phase lost stability and a transition into the tetragonal phase took place increasing the barrier again. Under compression the barrier first increases but at one point drops again and even becomes negative. By setting up an analytic model for the simple case of pure zirconia, it was possible to determine the reason for the dropping of the barrier under compression. Further investigations of more complex configurations in YSZ and SSZ exhibited strong correlation effects but preserve the overall shape of the  $\Delta E(\sigma)$  curve and especially the drop under compression.

In the next chapter a layered structure is introduced harnessing the strain dependence under expansion due to addition of yttrium, the reduction of the barrier due to intelligent

positioning of the yttrium content under avoidance of direct yttrium blockages and the neglecting of conductivity in one geometric direction of the compound.

## 8. Anisotropic YSZ

### 8.1. The layered structure

While conducting research on the electrolyte material YSZ, the idea was born that requiring high conductivities in all spatial dimensions of the electrolyte is a too strong constraint. Since basically only the ionic movement through the electrolyte needs to be high, it seems reasonable to systematically search for structures, which have an anisotropic conductivity, being high in the mentioned direction but probably low in other directions. An anisotropic conductivity requires a layered cation structure. Of course layers in many crystallographic directions are possible and most of them will be unfavorable [96]<sup>1</sup>. But the results of the previous chapters give criteria layered structures should fulfill thus excluding most of them. These criteria are:

1. Increase of the charge carrier number in the system without having any yttrium induced blockages along the pathways. This effect requires a layering of the cations of any reasonable thickness.
2. Obtaining oxygen lattice sites, which have exactly one yttrium ion as nearest neighbor, but at the same time all gate ions in the migration pathway are zirconium. This effect requires a clear alternating layering of the cations.
3. Increase of the lattice constant to introduce expansive strain, which decreases the migration barrier for oxygen ions. (This effect is desirable in any case)

One interesting layered structure has been found fulfilling these criteria, and having an enhanced conductivity into the direction of motion (c.f. Fig. 8.1). This is achieved by trading in the conductivity in another direction. Moving along the [001] direction in the fluorite structure, one passes layers of cations. In the proposed structure every second of these layers is a pure yttrium layer, and every other a pure zirconium layer. These layers lie in the plane spanned by the vectors [100] and [010]. The direction of oxygen ion motion is chosen in either of these two directions. The stoichiometry of this structure is  $Zr_2Y_2O_7$  exhibiting a vacancy concentration of 12.5%.

---

<sup>1</sup>E. Lee et al investigated the ionic conductivity in a structure having layers of pure yttrium in zirconium. Their idea was to have conduction channels without yttrium induced barriers. It turned out in their calculations, that the vacancies prefer the two anion planes directly at the yttrium layer. Therefore, they only observed oxygen migration along the yttrium plane exhibiting high migration barriers and conductivities lower than that of a system with randomly distributed yttrium ions. This is because one gate ion is always yttrium in the by them chosen layering. Such high barriers are avoided in the layered structure presented in this thesis.

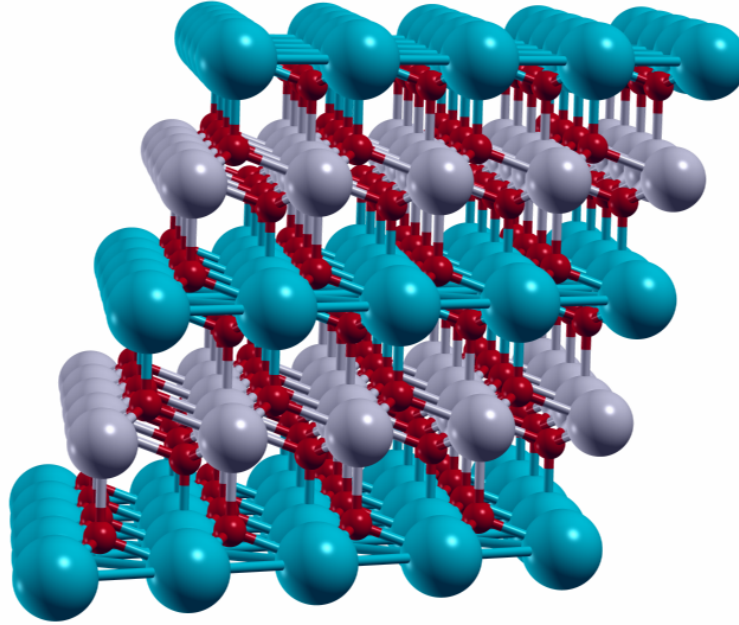


**Figure 8.1.:** Layered structure of the  $Y_2Zr_2O_7$  compound. For better visibility all oxygen atoms of the perfect fluorite structure are shown. (grey: zirconium, red: oxygen, teal: yttrium) [48]

The high yttrium content leads to an increased number of vacancies in the system. But due to the special arrangement of the cations, no yttrium induced high barriers are hindering the migration of oxygen ions between the electrodes (point 1). As shown in Eq. 4.25 the conductivity increases with the number of vacancies in the system. However, high vacancy concentrations give rise to vacancy clustering hindering the oxygen motion. It will be shown that no such clusters are formed in this construction. Pornpasertsuk et al. [90] already reported a decreased migration barrier, when the initial and final lattice site of an oxygen jump have one yttrium ion as nearest neighbor (point 2). The 1NN oxygen sites around yttrium ions are less favorable for vacancies, which reduces the relevant barrier in the migration pathway along the layering. Due to the high content of large yttrium ions, the lattice is expanded in comparison to pure zirconia. This is the origin of point 3. The strain effects have been discussed extensively in chapter 7. This is obtained just by increasing the yttrium content, independently of the dopant distribution – although a structure as proposed here leads to an anisotropic strain, and homogeneously distributed yttrium ions would give rise to isotropic strain. In contrast to this, point one and two require a clear layering of the cations. Point one just requires the cations to be ordered in layers, independently of the exact stacking order. Lastly, point two can only be achieved in a structure with alternating mono-layers in the  $[100][010]$  plane – or equivalent directions with the same symmetries. In the fluorite structure only this configuration exhibits pathways without yttrium gate ions and with nearest neighbor yttrium ions at each oxygen lattice site.

Since the vacancies disfavor 1NN positions to yttrium ions, the lattice sites with three yttrium ions as 1NN are avoided by the vacancies. This leads to a motion along zig-zag paths in the zirconium layers, which is effectively limited to two dimensions. In the third geometric direction, the barriers are very high due to the yttrium layers, making a motion into this direction basically impossible.

To represent the  $Zr_2Y_2O_7$  compound in a crystallographic cell, at least four fluorite unit cells are necessary. Basic investigations of the layered structure are done in a  $2 \times 2 \times 2$  supercell (4  $Zr^{4+}$ , 4  $Y^{3+}$ , 14  $O^{2-}$ , 2  $V^{2+}$ ), and extended calculations are done in a larger  $4 \times 4 \times 4$  supercell (32  $Zr^{4+}$ , 32  $Y^{3+}$ , 112  $O^{2-}$ , 16  $V^{2+}$ ).

**Anisotropic lattice** As pointed out before, the layered configuration of the cation sublattice gives rise to an anisotropic strain in the system, which leads to a deviation from the cubic crystal vectors. Many deviations are possible, but a simple ansatz is used to estimate possible deviations. In this ansatz, the directions of the unit vectors are constant, but their length can vary. Since no difference between the two lattice vectors in the plane of the layering can occur, only the deviation of the third vector [001] is considered. Thus, the unit vectors are given by:

$$a \cdot \begin{pmatrix} 0.5 & 0.5 & 0 \\ 0 & 0.5 & 0.5 \\ 0.5 \cdot c & 0 & 0.5 \cdot c \end{pmatrix} \quad (8.1)$$

where  $a$  is the cubic crystal constant and  $c$  denotes the deviation of the [001] vector from the other two vectors. The ground state is found by determining the cell volume with the lowest energy under variation of  $c$ . This minimization is done in two steps:

1. The cohesive energy of the system for four values of  $a$  is determined for fixed  $c$ . These energies are feed into a Birch-Murnaghan Equation of state (Eq. 6.1), by which the ground state  $E(V_0(c))$  for fixed  $c$  is determined.
2.  $c$  is varied and the respective ground states  $E(V_0(c))$  are determined until the energy minimizing deviation  $c_0$  is obtained. With  $c_0$  also the ground state volume  $V_0(c_0)$  is uniquely defined.

$$E(V_0(c_0)) = \min_c E(V_0(c)) \rightarrow V_0(c_0) \quad (8.2)$$

In the large cell all 16 vacancies are randomly distributed in the two zirconium layers. In such a configuration the following ground state is found<sup>2</sup>:

$$\begin{aligned}c &= 1.003 \\a &= 4 \cdot 5.282 \text{ \AA} \\V_0 &= 2364.90 \text{ \AA}^3 \\E_0 &= -1642.3951 \text{ eV} \\B_0 &= 159.69 \text{ GPa} \\\partial B_0 / \partial P &= 7.73516\end{aligned}$$

A cubic FCC cell with the same volume has a lattice constant of  $a_{\text{equiv}} = 5.285 \text{ \AA}$  (lattice constant of the corresponding fluorite unit cell), which is similar to the crystal constant determined in the cubic cell ( $a = 5.287 \text{ \AA}$ ). This shows a very small deviation from the cubic lattice vectors, indicating that a further consideration is not necessary.

In the next section, the stability of the cation lattice is taken into consideration using the small cell. In section 8.3 the correlation effects of vacancies are investigated, which are very important due to the high concentration of vacancies. Because the diversity of migration barriers occurring in this system is very high, it is impossible to determine one barrier as the relevant one. Rather, there is not one barrier alone that determines the activation energy, but many different barriers together. In such a complex system different means of evaluating the properties are necessary. Therefore, in section 8.4 ab-initio molecular dynamics calculations are presented, which yield the diffusivity and the activation energy – which can be considered as an efficient barrier – of the oxygen ion migration.

## 8.2. Stability considerations

The proposed structure is highly ordered. Due to entropy contributions, it will not form spontaneously, as long as the structure is not significantly more stable than all other possible configurations. However, technologically more sophisticated methods like Molecular Beam Epitaxy (MBE) are available that can assemble this structure layer by layer. This procedure is necessary to synthesize this structure. Still, the structure has to be at least metastable, even if the layered structure can be set up in MBE. Since cation diffusion in YSZ is very small at the operating temperature of a SOFC, such a metastability can be assumed (e.g. [97]). Nevertheless, a closer look into this aspect is mandatory. Therefore, this configuration is compared to a series of other structures of the same compound. Nevertheless, as long as the structure was formed by any synthesizing method capable of it, a high number of cation-vacancies are required to have any exchange of cations. It is a question of synthesizing accuracy how many

<sup>2</sup>Test calculations for further variational freedom have been executed. After determining  $c$ , the components of the [001] vector have each been optimized. This test led to minor changes of less than 1% in components inducing a negligible energy reduction of about 10 meV. Such small deviations could already be induced by varying vacancy distributions. Thus, it can be expected that including further degrees of freedom when optimizing the lattice vectors do not contribute to significant corrections.

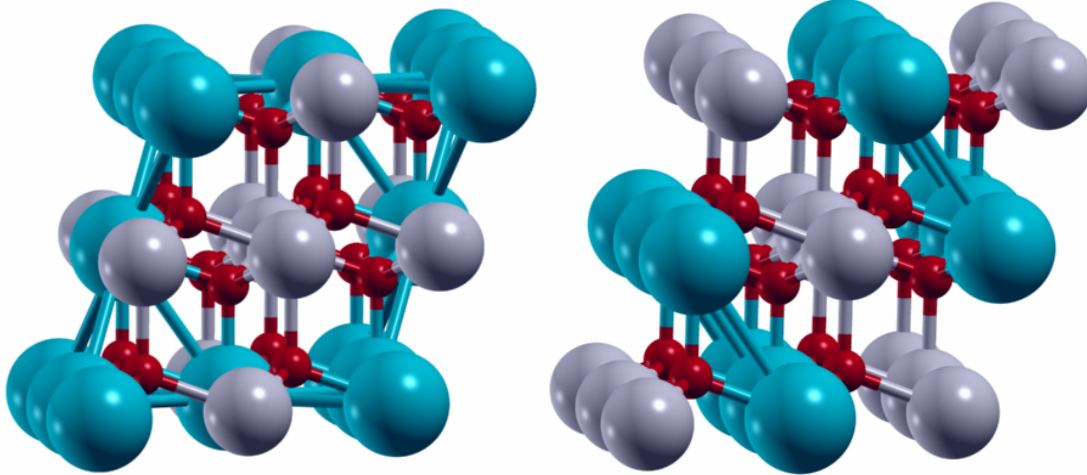


**Figure 8.2.:** The 3/1 (left) and the 2/2 (right) structure. (grey: zirconium, red: oxygen, teal: yttrium) [48]

cation-vacancies are present in the electrolyte facilitating the deviation from the perfect layer structure. However, as long as the migration barriers are large in comparison to the operating temperature, the structure will keep its configuration for a sufficiently long time.

	Energy (eV)	Volume ( $\text{\AA}^3$ )
4/0	-200.657	298.29
3/1	-200.264	298.51
2/2	-199.869	296.84

**Table 8.1.:** Energy and relaxed volumes of the layered and related configurations in the  $2 \times 2 \times 2$  cell without vacancies.

Different configurations of the 4 yttrium and 4 zirconium ions are compared in the  $2 \times 2 \times 2$  cell. In principle there are three different types of zirconium-yttrium configurations. The layered one [four zirconium ions in one layer, zero in the other (4/0)] (cf. Fig. 8.1), one configuration with two interchanged ions (3/1) (cf. Fig. 8.2 left) and one with equal amount of Y and Zr in both layers (2/2) (cf. Fig. 8.2 right). Although there are different con-

figurations in the (3/1) and the (2/2) distribution, only those are relevant, which have the lowest energy. In table 8.1 the energies of the system without vacancies (and adapted number of electrons) are shown. Although the 2/2 structure is also a perfectly layered structure in another crystallographic direction, it is less stable than the 4/0 structure. The 3/1 structure is also about 0.4 eV higher in energy than the 4/0 structure.

The calculations without vacancies show the pure effect of the cation ordering. Since the vacancy correlations have a strong impact on the configurational energy, the computations have to be complemented by calculations with vacancies. Previous publications reported that the second nearest neighbor position of vacancy to yttrium is the most favorable distance (e.g. [90]). Thus, the less yttrium ions are on 1NN positions to vacancies, the more stable the structure is. This can also be seen from the computational

	Energy (eV)	Volume ( $\text{\AA}^3$ )
4/0 f	-204.3542	269.16
3/1 r	-204.2092	297.8
3/1 f	-204.4888	298.28
2/2 r	-201.048	292.78
2/2 f	-203.4579	295.64

**Table 8.2.:** Energy and relaxed volumes of different  $Zr_2Y_2O_7$  structures, with favorable (f) positioned and randomly (r) positioned vacancies (one possibility). In the 4/0 structure only favorable vacancy positions are stable all 4/0 r configurations would relax towards a 4/0 f one.

are positioned at these sites, the 3/1 configuration becomes more stable than the 4/0 structure. However, from the 16 oxygen lattice sites, 12 are  $Zr_2/Y_2$ , two are  $Zr_0/Y_4$  and two are  $Zr_4/Y_0$  sites. Thus, only 2 lattice sites are favorable. The 2/2 structure is less stable, since there are only  $Zr_2/Y_2$  lattice sites in the system.

In the large  $4 \times 4 \times 4$  super cell, there are about  $1.8 \cdot 10^{18}$  combinations possible in the cation sub-lattice. Obviously, many of them are equivalent to each other and can be transferred by symmetry operations. Nevertheless, the sheer number of configurations prevents a rigorous investigation. It would also not help the understanding any further. Once the structure is synthesized, an exchange of cations is very unlikely.

The work by Predith et al. [98] further corroborates the assumption of stability for the here proposed structure. They investigated many different configurations for different compositions of the Y-Zr-O system in both the monoclinic and the cubic fluorite structure. They predicted that a composition of 33% Yttrium in zirconium oxide has the most negative formation energy. This energy of the most stable structure of a given composition increases only little up to an yttrium content of 60%. For the compound  $Y_2Zr_4O_{11}$  they predicted a layered structure in planes equivalent to the here proposed structure. One of their layers is completely filled with zirconium and every other with a mixture of yttrium and zirconium. The zirconium ions in this plane are surrounded by yttrium hexagons. Although their  $Y_2Zr_4O_{11}$  compound exhibited layers in the same direction as the here proposed structure, they did not report the here presented new electrolyte structure for enhanced conductivity. Furthermore, they did not investigate any ionic motion in these structures and only determined possible ground states at different compositions of the Y-Zr-O system.

results in Tab. 8.2. If the vacancies are set to lattice sites with as little yttrium neighbors as possible (favorable structures, referred to by the addition 'f'), the structure is more stable than in the case that they are randomly distributed (referred to by the addition 'r'). When the vacancies are positioned favorably, the 3/1f structure is more stable than the 4/0f structure. Based on the V-Y distance, this is quite clear: In the 4/0f structure, all favorable vacancy positions have three zirconium NN and one yttrium NN ( $Zr_3/Y_1$  lattice sites), while in the 3/1f structure, there are two lattice sites with no yttrium NN at all ( $Zr_4/Y_0$ ). Thus, if the vacancies

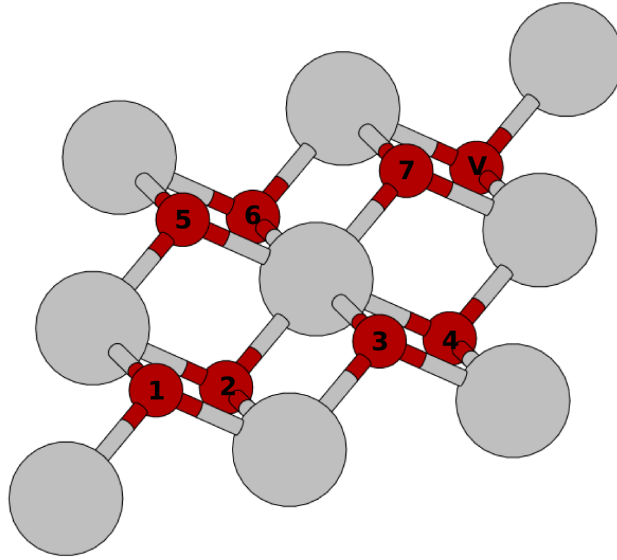


**Figure 8.3.:** Representation of a single zirconium layer in the  $2 \times 2 \times 2$  cell with vacancy position indices. As in any VASP computation periodic boundary conditions apply here. This means that the four depicted corner ions are in fact one and the same ion. Thus e.g. position 1 and 4 are direct neighbors. [48]

### 8.3. Vacancy-Vacancy interactions

Position of 2 <sup>nd</sup> vacancy	Energy in eV
1	-202.78
2	-204.28
3	-204.37
4	-204.28
5	-204.37
6	-204.30
7	-204.37

**Table 8.3.:** Energies of vacancy configurations in one zirconium layer (cf. Fig. 8.3). One of the two vacancies is located in the 'V' position, and the other one takes all seven possible positions. Note, that these are the total energies of the  $2 \times 2 \times 2$  supercell.

From now on it will be assumed that the layered structure as depicted in Fig. 8.1 has been build and is metastable. The following considerations only address the distribution and motion of oxygen ion vacancies.

In the  $2 \times 2 \times 2$  cell two vacancies are present. The vacancies prefer the lattice sites with three zirconium NN and one yttrium NN ( $Zr_3/Y_1$ ). In fact, if set to the  $Zr_1/Y_3$  positions, the vacancies will relax in most cases to a nearby  $Zr_3/Y_1$  site. Interactions with other vacancies might prevent that, but the energy is minimal if all vacancies are on  $Zr_3/Y_1$  lattice sites. This reduces the number of oxygen lattice sites taking part in the migration process by half. Consequently, there are only eight lattice site available for vacancies in the

$2 \times 2 \times 2$  cell. For one fixed vacancy, seven different sites are available for the second vacancy (cf. Fig. 8.3 and Tab. 8.3 for the energies). Here it turns out that most pairs are very close in energy. Only position 1 of the second vacancy leads to a higher energy. Due to the periodic boundary conditions, the two vacancies form a [111] vacancy pair in this configuration.

In the  $4 \times 4 \times 4$  layered cell with only two vacancies ( $e^-$  number adapted) these correlations are checked again. It turns out that not only the [111] pair, but also the [100] and [110] pairs are unstable. This was not visible in the small cell, since the vacancies cannot have a greater distance than 2NN. Because only the  $Zr_3/Y_1$  lattice sites are accessible by the vacancies, they move away in plane. Starting from either a [100] or a [110] pair, the vacancy end up in [121] pairs. Such a pair is simply one oxygen site more distant than in the [110] pair. Starting from a [111] pair, one of the vacancies move one site further and they assume a [211] distance. The energies of the two stable pairs in the  $4 \times 4 \times 4$  cell are  $E_{[120]} = -1613.032 \text{ eV}$  and  $E_{[211]} = -1613.014 \text{ eV}$ . The energy of the system, when the two vacancies are located as far away from each other as possible in the given cell, is  $E_{\text{far}} - 1613.446 \text{ eV}$ . This indicates that the vacancies are repelling each other even over a longer distance.

While in this system the vacancies cannot keep nearby lattice sites, such behavior was not observed in this way in 8YSZ. However, the tendency is already visible in Fig. 7.16, in which the configuration with the smaller distance between vacancies was less stable than the one with large distance. In contrast, it is known that, especially at high vacancy concentrations, the vacancies will cluster and form stable pairs. Such pairs are not seen in any calculation of the layered structure.

To figure out, whether the absence of vacancy clustering is a numerical problem, or in fact physical, the vacancy pairs are calculated in pure zirconia ( $3 \times 3 \times 3$  cell). In these simulations it turns out that the [111] pair is  $\Delta E_{[100][111]} = 0.5 \text{ eV}$  more stable than a [100] pair, but the [110] is  $\Delta E_{[110][111]} = -0.43 \text{ eV}$  more stable. The resulting energies of the vacancy pairs are  $E_{[100]} = -769.859 \text{ eV}$ ,  $E_{[110]} = -770.789 \text{ eV}$ , and  $E_{[111]} = -770.358 \text{ eV}$ . With the ordering  $E_{[100]} > E_{[111]} > E_{[110]}$ , there is clearly a stable vacancy pairing along the [110] direction possible in pure zirconia. Although, in literature typically the [111] vacancy pair is denoted as the most stable one (e.g. [99]), there are reports that in some cases the [110] pair is the most stable one. T. Bredow [82] assumed that the [110] pair becomes more stable when the cubic phase is not fully stabilized, which is consistent with the here used pure zirconia system. This shows, that the formation of vacancy pairs as described in literature is reproduced in the pure zirconia system and the absence of this clustering effect is due to the specific configuration, and not due to numerics.

Using again the  $4 \times 4 \times 4$  cell with only two vacancies, the migration barrier is computed. Since vacancy pairs closer than the [120] pairs are unstable, the next vacancy is either on the [120] position, or one site farer away. In Fig. 8.4 the MEP between these two positions is shown. Due to the second vacancy, the jump is not symmetric. Both the forward and the backward jump have a barrier of about  $\Delta E \approx 0.1 \text{ eV}$ . This is by a factor of three smaller than the equilibrium volume jump in pure zirconia, and a factor six smaller than the literature values corresponding to a randomly displaced oxygen

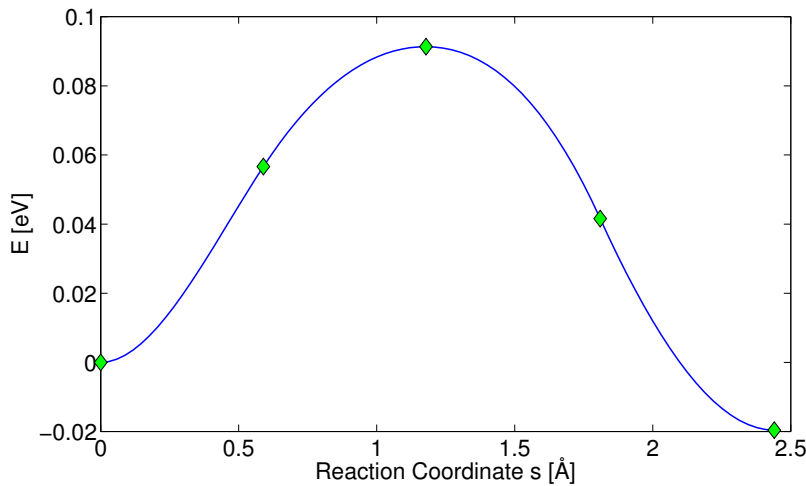


**Figure 8.4.:** MEP of a jump in the layered structure. The ending point has the larger vacancy-vacancy distance.

sub-lattice [92]. In fact, this tetragonal displacement of the oxygen sub-lattice has also been observed in the layered structure, which is reasonable considering the large lattice constant. Thus, the barrier of 0.1 eV actually has to be compared to the value 0.6 eV. However, this barrier is determined in an idealized case, where only two vacancies are present in the system and are sufficiently far away from each other. It will become clear that in the case of small barriers it is the correlation of vacancies, which mainly determines the activation energy of the diffusion process. Hence, the potential surface in the 16 vacancy case is highly complicated and cannot fully be grasped by determining migration barriers alone, but the dynamics in the whole system needs to be accounted for.

To investigate this long range interaction further, the configurational energy of different pairs is determined in the two vacancy system. From these computations the general trend that larger vacancy separations lead to smaller energies even over a large distance can be seen. However, this is no monotonous function of the vacancy separation since there is also a dependence on the crystallographic direction of the vacancy-vacancy pair. Separations smaller than  $4.58\text{\AA}$  are not stable (cf. Fig. 8.5), because the energy difference to the next farer site is larger than the small barrier of 0.1 eV in between.

As has been pointed out before, the low barrier between neighboring oxygen sites does not at all determine the activation energy of the diffusion process in the zirconium layers. The 16 vacancies are located on the  $64 Zr_3/Y_1$  lattice sites. Consequently, every fourth oxygen site is occupied by a vacancy, which leads to an average vacancy-vacancy distance of  $7.5\text{\AA}$ . To get an idea how the barriers in the system with all vacancies look like, the 16 vacancies have randomly been distributed throughout the two zirconium layers of the  $4 \times 4 \times 4$  supercell. Except for choosing only  $Zr_3/Y_1$  sites no further rules have been applied in the distribution. After setting up the cell, the system has been relaxed to

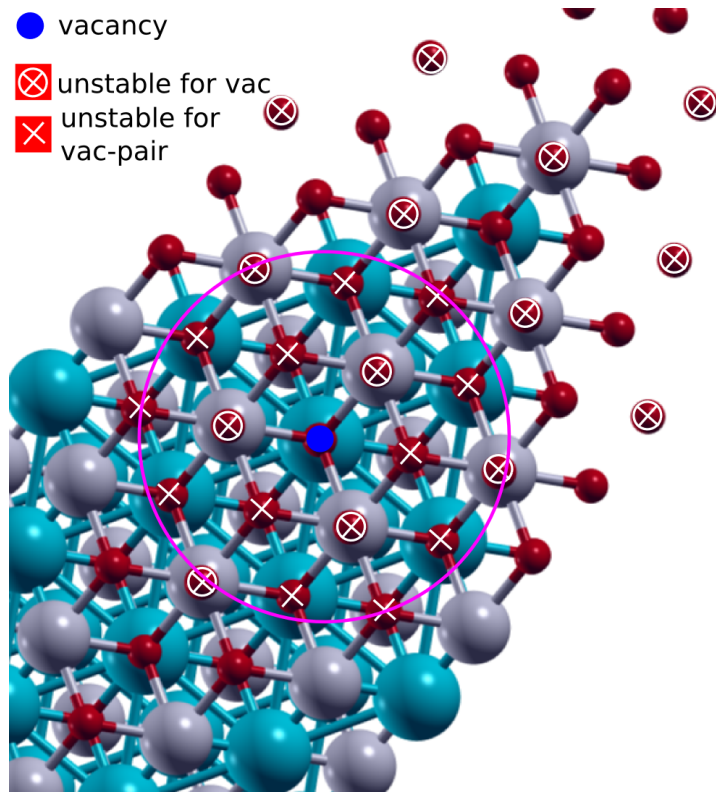


**Figure 8.5.:** Local vacancy-vacancy correlation in one layer with two vacancies. When a vacancy is located at the blue spot, there can be no second vacancy on the surrounding oxygen sites. The simple crosses indicate unstable position for a second vacancy due to the V-V repulsion and the circled cross indicates  $Zr_1/Y_3$  lattice sites being generally unstable for vacancies. (grey: zirconium, red: oxygen, teal: yttrium) [48]

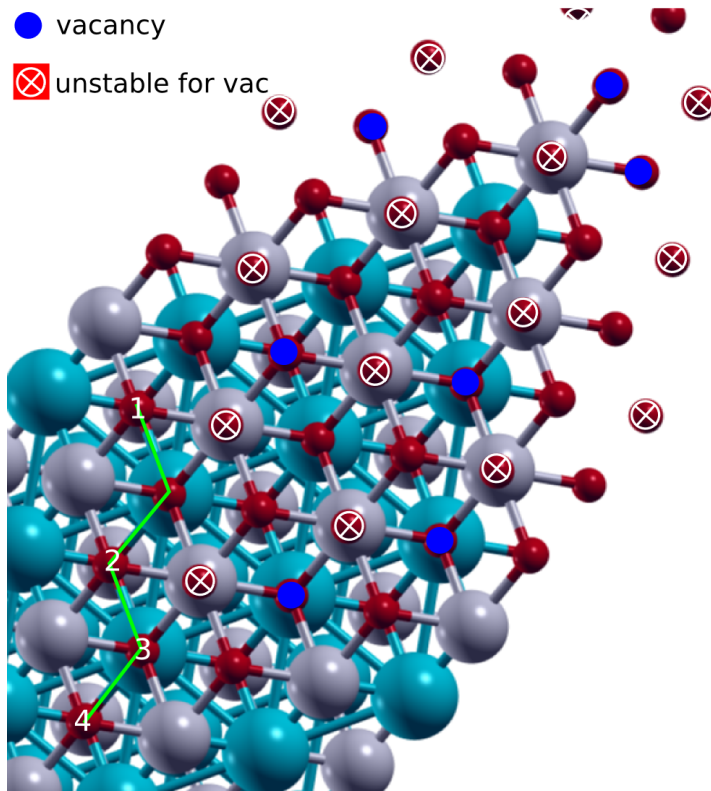


**Figure 8.6.:** Distribution of vacancies in the layered structure (not optimized vacancy position). The numbers correspond to the vacancy positions in the in Fig. 8.7 depicted MEPs. (grey: zirconium, red: oxygen, teal: yttrium) [48]

the next local minimum. Subsequently, the MEP for the motion of one vacancy over five lattice sites has been computed with the NEB method. The vacancy distribution and the pathway of the moving vacancy are shown in Fig. 8.6. First, one can see that in these calculations vacancies can keep closer than the  $4.58\text{\AA}$  observed before. In fact, it is possible for two vacancies to be on directly neighboring lattice sites, if further vacancies surrounding their positions prevent their departure. It has to be pointed out that this is a special case and the computations do not give any statement how stable this configuration is, and how likely it is for this configuration to arise in a dynamical system.

The potential surface experienced by the moving vacancy is shown in Fig. 8.7. The maximal barrier is  $1.9\text{eV}$ , which is much higher than the barrier resulting from the lattice ( $\Delta E_{\text{lat}} \approx 0.1\text{eV}$ ). This high barrier can surely be avoided by moving along different pathways, but due to the high concentration of vacancies, it is unlikely to find one without any such high barriers for a given vacancy distribution.

Between layers there is also a correlation between the vacancies. But due to the large distance and the shielding by the yttrium layer, they are less relevant than the ones in plane. A  $[111]$  vacancy pair through the layer is over  $0.5\text{eV}$  higher in energy than

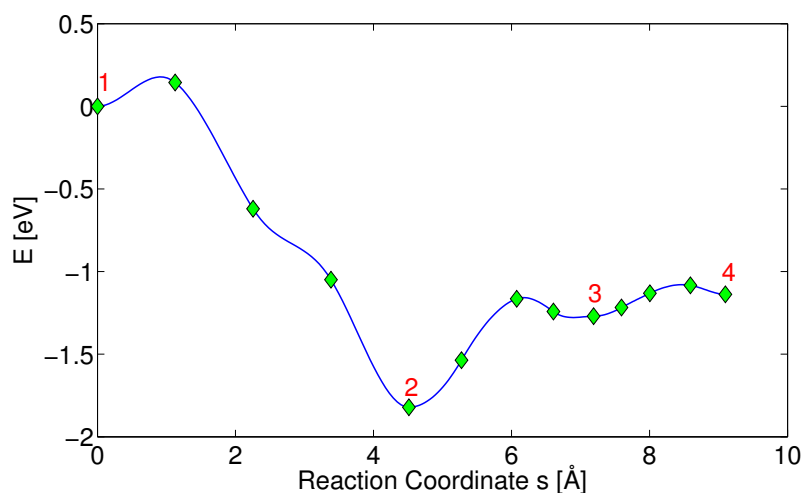


**Figure 8.7.:** Minimum Energy Pathway for a vacancy in the layered structure with all 16 vacancies in the relaxed non cubic cell. From the first to the last vacancy position this pathway spans five oxygen sites in which the first jump, from 1 to 2, is a jump over two sites.

at farer distance, but is still metastable. These correlations vanish in the layer under consideration, as soon as the invoking vacancy makes a jump away.

In figure 8.8 the density of states of the layered structure in the  $4 \times 4 \times 4$  supercell with all 16 vacancies is depicted. This shows, that the layered structure is still a wide band gap insulator with a band gap in these computations of  $E_{\text{Gap}} = 3.5 \text{ eV}$ , which is even  $0.4 \text{ eV}$  larger than the one determined in pure zirconia (cf. 6.3).

Although this looks that we jumped out of the frying pan and into the fire when introducing this system, there is one consideration that could safe the day: These high barriers do not result from vacancy pair bonds, but from vacancy repulsion. This means that as soon as the vacancy inducing such correlation effects moves away, the barrier in this direction will drop.

Before moving to the MD calculations a last point needs to be mentioned: As has been seen in Fig. 8.6 it is possible for vacancies to take nearby sites for a short time, if another driving force is present. This could be caused by other nearby vacancies, which have to move away before the two vacancies under consideration can depart, or the extraction of oxygen ions by the fuel at the anode of the SOFC. It is not clear, whether the extraction of oxygen by the fuel is a strong enough driving force to impose such unfavorable configurations to the electrolyte, but if such situations occur at one side of the electrolyte, the vacancies will literally be pushed into the electrolyte, probably leading to an enhanced motion in a layer near to the anode.

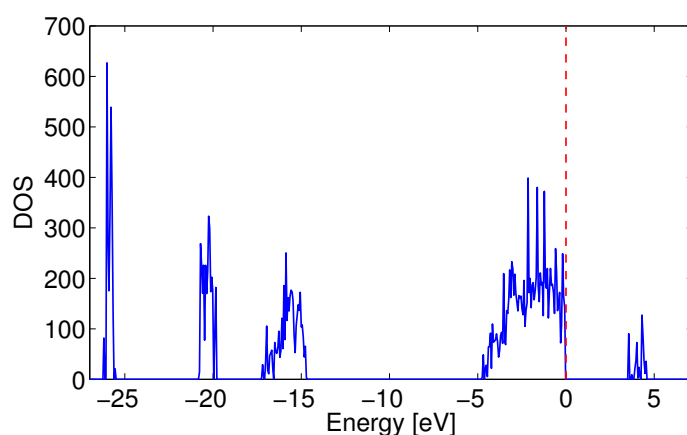


**Figure 8.8.:** Density of states of the layered structure with vacancy concentration being in accordance to the yttrium content.

## 8.4. Molecular Dynamics

As mentioned before, the correlation effects in the layered structure due to the high number of vacancies lead to a complexity, which cannot be fathomed by straightforward inspection of the migration barriers as it has been done in chapter 7. If the interactions between the vacancies would be purely electrostatic, such an approach would be feasible, but the relaxation of the lattice around a vacancy contributes not insignificantly to this interaction. The energy change resulting from the adaption of the lattice for two nearby vacancies cannot easily be determined from the relaxation pattern of separated vacancies. Alternatively, it is possible to compute the system with all changes and interactions as a whole by doing Molecular Dynamics (MD). Classical pair-potentials as the Buckingham potential are often used for this purpose. They are computationally inexpensive but the results are doubtful, especially in such complex systems. To determine the diffusion in the layered structure on basis of a very accurate description of interactions, ab-initio molecular dynamics as implemented in VASP are employed. From the computational demand of this framework follows a rather limited size of the calculations both in spatial and temporal extent. Thus, this approach clearly has the caveat that the statistics are not as good as in classical pair-potential MD. This is especially the case at low temperatures, when the dynamics is low and the number of jumps is small. Nevertheless, it is better to determine an accurate activation energy with larger error bars, than a wrong activation energy with small error bars.

The MD computations are executed in the  $4 \times 4 \times 4$  supercell of the layered structure including plane waves up to an energy cut off of 300 eV and sampling the Brillouine zone using only the gamma point. For the description of the thermodynamics, a micro-canonical ensemble is considered. In this way the temperature is not controlled by a thermostat and is therefore fluctuating throughout the MD run. At the beginning of a MD run VASP assigns gaussian distributed velocities to the ions in such a way, that the

initial temperature corresponds to a given starting value. In this procedure, it is not meaningful to allocate a mean temperature and mean squared displacement (MSD) for one run. Therefore, each time step, with its own temperature value, of all MD runs with different starting temperatures is plotted together with the corresponding MSD of the oxygen ions. The Einstein relation (Eq. 4.20) can be rewritten as

$$\langle r^2 \rangle (t) = D_0 \cdot t \cdot 2 \cdot d \cdot e^{-E_A/k_B T} \quad (8.3)$$

with the time  $t$ , the dimensionality of the diffusion process  $d$ , the activation energy  $E_A$  and the diffusivity at infinite temperature  $D_0$ . As has been pointed out before, the diffusion process only takes place in plane, and is thus two dimensional. However, the ionic movement for small deviations has a not insignificant component in the third dimension due to the zig-zagging through the zirconium layer. Although this error becomes small for large deviations, it will be accounted for by projecting the displacement of the oxygen ions into the layer-plane. In this way no deviation in the third dimension is included and the usage of  $d = 2$  in Eq. 8.3 is fully justified. Due to the periodic boundary conditions, the oxygen ions can leave the cell and enter it again on the corresponding position on the other side of the cell. This has explicitly been accounted for when computing the MSD, by considering the motion of such jumping ions as smooth movement out of the computational cell. Now, with  $d = 2$  Eq. 8.3 can be written as

$$\ln \left( \frac{1}{4} \langle r^2 \rangle (t) \right) - \ln(t) = \ln(D_0) - \frac{E_A}{k_B T}. \quad (8.4)$$

Plotting the left side of the equation, which is the logarithm of the instantaneous diffusivity  $\ln(D)$  from the MD run, over the inverse temperature results in an Arrhenius plot of all data points. Linearly fitting the cloud of data points in this plot corresponds to executing the time-averaging of the left side of the equation (time averaging of  $\ln(D)$ ) and of the inverse temperature

$$\left\langle \ln \left( \frac{1}{4} \langle r^2 \rangle (t) \right) - \ln(t) \right\rangle = \ln(D_0) - \frac{E_A}{k_B} \cdot \left\langle \frac{1}{T} \right\rangle. \quad (8.5)$$

This yields the activation energy of the oxygen ion diffusion in the layered structure  $E_A$  and the maximum diffusivity  $D_0$ , which together determine  $D$  at all temperatures.

#### 8.4.1. Computational Results

First a specific configuration is set up, in which all 16 vacancies are located in one half of the cell distributed over both zirconium layers. The vacancies are that closely packed in this configuration, that they directly repel each other and strive for an homogeneous distribution in the zirconium layers. This extreme concentration gradient gives some idea, how strongly the vacancies push each other when a concentration gradient is present in the electrolyte. This is always the case in an operating SOFC. Due to the periodic boundary conditions, the vacancies can move in both directions to equilibrate the distri-

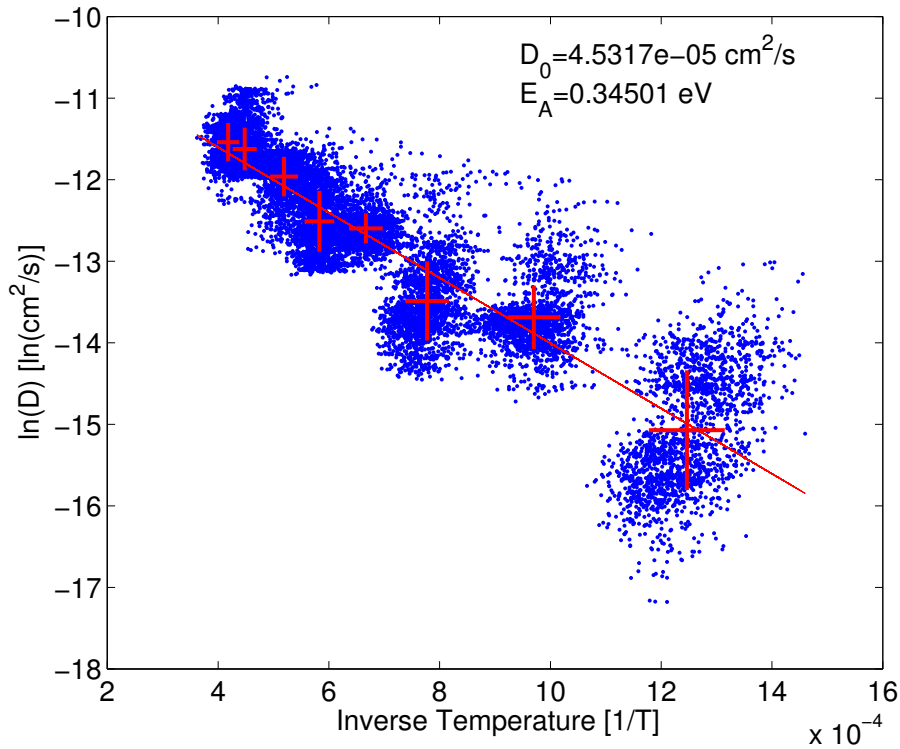


**Figure 8.9.:** Arrhenius plot of the MD data. The blue dots are the data-points from the MD calculation, the red line is the linear fit of all of these data-points in this plot. The crosses indicate the error-bars of each MD run.

bution. In fact, after only 1.1 ps the concentration gradient vanished and the vacancies assumed stable distances to each other. In this MD run, it was again very well visible that the yttrium-near positions are mostly avoided by the vacancies. However, in some cases, vacancies moved over into the yttrium layer, when the repulsion of other vacancies nearby made it energetically possible. These yttrium-near vacancies only have a short lifetime and move back into the zirconium layer once other nearby vacancies moved away. This MD run was executed over a total of 10 picoseconds in order to bring the system to a state near the thermodynamic equilibrium.

This end state (after local relaxation of the ionic positions) is then used as a starting configuration for a series of MD runs with different initial temperatures to determine the diffusivity, the activation energy and the conductivity of the layered structure. Statistical data are collected over 10 picoseconds for each starting temperature.  $E_A$  and  $D_0$  are subsequently obtained by Eq. 8.5. To check, whether the sampling-time is long enough, one MD run has been executed for 25 ps leading to no change of the diffusivity determined at the temperature of the considered MD run.

Since the vacancies hinder each other's motion, it is expected that the diffusivity is low

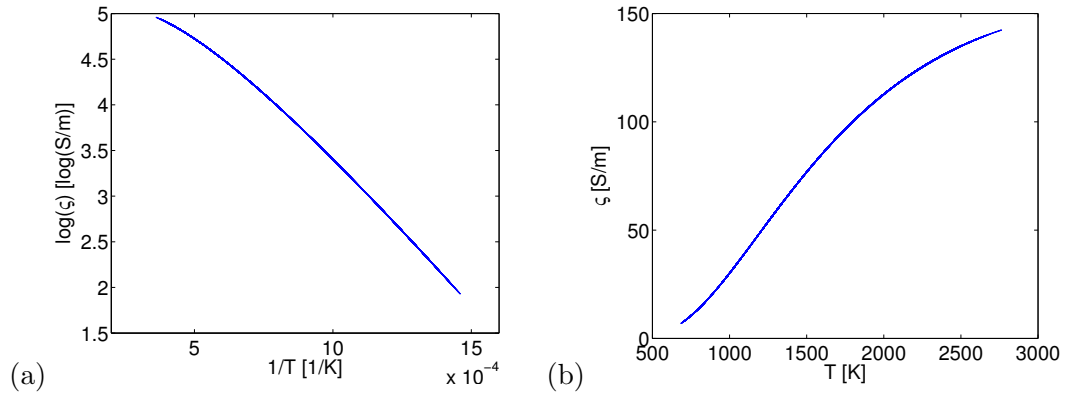


**Figure 8.10.:** Ionic conductivity in the layered structure: (a) as an Arrhenius plot, and (b) as the temperature dependent ionic conductivity.

and the activation energy is high. In Fig. 8.9 the MD results are shown in Eq. 8.5. The migration barrier is with  $E_A = 0.34$  eV higher than the migration barrier determined without vacancy interactions  $\Delta E = 0.1$  eV, but much lower, than the high barriers seen in Fig. 8.7 of about  $\Delta E \approx 1.9$  eV. In fact, obtaining an activation energy of about 0.3 eV is a very good result, showing, how the intelligent positioning of cations in the system leads to a reduction in activation energy. In experiments the value for 8YSZ is typically about 0.8 eV to 1 eV [95]. The absolute value of the diffusivity is, at a temperature of  $T = 800$  K, about two orders of magnitude higher than the experimental results of 10YSZ from Kilo et al. [100], while their activation energy was  $E_A = 0.99$  eV. In simulations, the obtained migration barriers are typically lower than the experimental ones. Devanathan et al. gave a summary of some numerically determined migration barriers in 8YSZ from different sources, lying between 0.2 eV and 1 eV. The lowest reported value was from Li and Hafsjold [101], who used classical pair potentials to determine their barrier and obtained very different results for different sets of interaction parameters. Typical values of more reliable sources are about 0.6 eV. In Fig. 8.10 the conductivity is determined from the diffusivities using Eq. 4.23. Ivers-Tiffée et al. [69] give a comparison of experimental conductivities of different solid state electrolytes, in which LSGM is the one with highest conductivity of  $\sigma_{\text{LSGM}}(T = 800^\circ\text{C}) = 18$  S/m, while YSZ has a conductivity of  $\sigma_{\text{YSZ}}(T = 800^\circ\text{C}) = 2$  S/m. Other publications give similar values [73, 102, 103]. The in this thesis discussed layered structure has a two-dimensional conductivity of  $\sigma_{\text{layer}}(T = 800^\circ\text{C}) = 42$  S/m being even higher than the LSGM conductivity. This is even more remarkable, when considering that only half of the oxygen ions, those in the zirconium layer, take place in the diffusion process, and the MSD, is accordingly averaged over all oxygen ions in the system.

This shows that the diffusivity as well as conductivity of the layered structure is much higher than 8YSZ and LSGM. Even though this structure was specially designed to have such high conductivities, it was still surprising to obtain such high performances considering the vacancy-vacancy interactions.

## 8.5. Conclusions

In this chapter, a new intelligent configuration of YSZ has been proposed harnessing the strain dependent barrier, the avoidance of yttrium induced high barriers along the pathway, and the reduction of the relevant migration barrier by neighboring yttrium dopants. In this way an increased diffusivity and conductivity of the compound has been achieved in two dimensions, while the ionic mobility in the third dimension has been sacrificed. The activation energy of this diffusion process is only  $E_A = 0.34$  eV leading to a conductivity at  $T = 800^\circ\text{C}$  of  $\sigma_{\text{layer}} = 42$  S/m, which is more than double the one of LSGM. Due to the small barrier, the conductivity at lower temperatures is in comparison to other electrolytes even higher than this. At  $500^\circ\text{C}$  the conductivity of 8YSZ is only  $\sigma_{\text{YSZ}} = 0.11$  S/m,  $\sigma_{\text{LSGM}} = 0.9$  S/m for LSGM and the layered structure exhibits a conductivity of  $\sigma_{\text{layer}} = 13$  S/m. It need to be noted, that simulation results often underestimate the migration barriers in YSZ (difference 0.6 eV in many simulations to 1 eV in typical experiments), thus, the here presented conductivities might be overestimated as well, but in comparison to other simulations it is still a remarkable enhancement. This advantage has to be bought with exchanging the simple and fast synthesizing methods like Sol-Gel and sintering with more complicated synthesizing methods as molecular beam epitaxy. It might be advantageous to reduce the number of vacancies to obtain less repulsion and thus have a smaller activation energy. However, reducing the number of charge carriers has a contrary effect and whether a reduction of vacancies increases or decreases the performance cannot be answered without further investigations. For such cases, the yttrium content in the system can be reduced, to decrease the number of vacancies, by e.g. using the layered structure of  $\text{Y}_2\text{Zr}_4\text{O}_{11}$  found by Predith et al., which has an overall vacancy concentration of 9%.



## 9. Summary

This thesis is dedicated to investigate zirconia based solid oxide electrolytes, its ground state properties and especially the oxygen migration within. Since classical approaches to enhance the mobility of oxygen ions are basically exhausted, alternative ways need to be chosen to understand and enhance the ionic migration in these materials. In particular quantum mechanical investigations of strain dependent migration barriers and of a new superior electrolyte material with anisotropic conductivity have been conducted. In the process of understanding the widely in this thesis used NEB method, a new modification of this method was devised, the MsNEB, which could find low-lying minima in complex phase spaces

DFT computations in connection with the NEB method showed a decreasing migration barrier with an expansion of the lattice, but additionally a maximum of the migration barrier at a strong compression, after which the barrier dropped again. This unexpected behavior at high compressive strain had been analyzed in a simple model. This complementary model offered the conclusive explanation, that the ground state energy is elevated in a way, that the total barrier drops under sufficient compression. From this, one can deduct that it might be advantageous, not only to look for a reduction of the maximal energy along a migration pathway, but also try to raise the energy of the ground state, which effectively decreases the barrier, as well. This opens up new perspectives to enhance the performance of electrolyte materials. In fact, this has been done when developing a new material with enhanced ionic conductivity.

Realizing that ionic motion is not necessary in all three dimension of an electrolyte also facilitate new possibilities. This has been applied by developing a zirconia base electrolyte with alternating layers of yttrium ions and zirconium ions in the fluorite structure. The ionic migration in the zirconium layers is strongly enhanced, while the mobility through the yttrium layers has been sacrificed. Overall three effects are combined to obtain the superior conductivity in plane: (1) The high dopant concentration leads to a high charge carrier concentration, but the structure avoids high barriers induced by yttrium ions in the pathway. (2) Vacancies disfavor nearest neighbor positions to yttrium ions, but only lattice sites with at least one yttrium neighbor exist in this structure, which increases the energy of the lattice sites, and at the same time induces a reduction of the energy at the barrier due to the nearby yttrium ions, leading to an effective reduction of the barrier. (3) The large number of yttrium ions expands the fluorite lattice inducing expansive strain to the zirconium layers, which reduces the barrier.

The average migration barrier in this structure is with  $E_A = 0.34$  eV much smaller than in 8YSZ (simulations  $\approx 0.6$  eV, experiments  $\approx 1$  eV). This leads to conductivities of 42 S/m at 800°C and 13 S/m at 500°C. With these results, the new structure outperforms 8YSZ by far and even exceeds the high performance electrolyte LSGM. In

fact, the conductivity of 8YSZ at  $800^{\circ}\text{C}$  is only  $2\text{S/m}$ , which is by about a factor of six less than the conductivity of the layered structure at  $500^{\circ}\text{C}$ . This advantage has to be bought with exchanging the simple and fast synthesizing methods like Sol-Gel and sintering with more complicated synthesizing methods as molecular beam epitaxy (MBE) or chemical vapor deposition (CVD) methods. However, in times when it becomes clear that simple methods for enhancing the conductivity of electrolytes do not suffice to meet the requirements for batch production, science and industries have to dare to use more exotic approaches, and need to be willing to utilize complex structures to obtain fuel cells of higher performance.

Throughout the extensive application of the NEB method to determine migration barriers, a modification of NEB was devised leading to a deeper understanding of the method itself and has a very interesting and useful application. The Minimum search Nudged Elastic Band (MsNEB) method is, in fact, able to find not only transition states, but also new ground states. Moreover, the underlying functionality differs already in the principle from energy-based methods like simulated annealing and the genetic algorithm, making it a complementary scheme. Until now, the MsNEB has not been applied to the electrolyte materials itself, but already showed its power by finding a new most stable isomer in the trial case  $P_8$ .

# A. Appendix

## A.1. Solvers for eigenvalue problems

### A.1.1. Blocked Davidson algorithm (DAV)

The Davidson algorithm [104] is suited to compute the eigenpairs of outer blocks of a large symmetric sparse matrix. Doing this block-wise, it is possible to determine the eigenpairs of the whole matrix. The core quantity is the residual vector

$$|R_i\rangle = (\mathcal{H} - E) |\phi_i\rangle \quad \text{with} \quad E = \frac{\langle \phi_i | \mathcal{H} | \phi_i \rangle}{\langle \phi_i | \phi_i \rangle}. \quad (\text{A.1})$$

These residual vectors are first preconditioned to obtain a better convergence

$$|p_i\rangle = \mathcal{K} |R_i\rangle \quad (\text{A.2})$$

with the precondition operator  $\mathcal{K}$ . In the next step the preconditioned residual vector is orthonormalized to the wave-functions

$$g_i = \left( 1 - \sum_{i'} |\phi_{i'}\rangle \langle \phi_{i'} | \mathcal{I} \right) |p_i\rangle \quad (\text{A.3})$$

with  $\mathcal{I}$  being the identity matrix. With the preconditioned and orthonormalized residual vectors  $g_i$  the blocked Davidson algorithm can start:

1. Initialize wave-functions  $\{\phi_i^0, i = 1 \dots N_{bands}\}$ , the superscript 0 denotes the initial guess (e.g. superposition of atomic orbitals)
2. Choose a subset (block) of all bands  $\{\phi_i^0, i = 1 \dots N_{bands}\}$ ,  $\{\phi_k^0, k = 1 \dots i_1\}$
3. Optimize the  $\phi_k^0$  by adding  $g_k^0$  to the subspaces spanned by  $\{\phi_k^0, k = 1 \dots i_1\}$

$$\left\{ \phi_k^0 / g_k^0 = \left( 1 - \sum_{i=1}^{N_{bands}} |\phi_i\rangle \langle \phi_i | \mathcal{I} \right) \mathcal{K} (\mathcal{H} - \epsilon_{\text{approx}} \mathcal{I}) \phi_k^0 | k = 1 \dots i_1 \right\} \quad (\text{A.4})$$

4. Find the  $i_1$  lowest vectors  $\phi_k^1$  using the Raighley-Ritz method in the subspace under consideration

5. Add further preconditioned orthonormal residuals  $g_k^1$  computed from the  $\phi_k^1$

$$\left\{ \phi_k^1 / g_k^0 / g_k^1 = \left( 1 - \sum_{i=1}^{N_{\text{bands}}} |\phi_i\rangle \langle \phi_i | \mathcal{I} \right) \mathcal{K} (\mathcal{H} - \epsilon_{\text{approx}} \mathcal{I}) \phi_k^1 | k = 1 \dots i_1 \right\} \quad (\text{A.5})$$

6. Go back to 4. until the wave-functions  $\phi_k$  converged.
7. Update  $\{\phi_i, i = 1 \dots N_{\text{bands}}\}$  with the converged bands  $\phi_k$ . Go back to 3. with a new subset of bands  $\{\phi_k^0, k = (i_1 + 1) \dots (2 \cdot i_1)\}$  until all bands are converged
8. Apply the Raighley-Ritz optimization to the whole set of converged wave-functions

### A.1.2. Residual minimization scheme, direct inversion in the iterative subspace (RMM-DIIS)

In the residual minimization scheme not the eigenvalues itself are optimized but the norm of the residual vector

$$\langle R_i | R_i \rangle = \langle \phi_i | (\mathcal{H} - \epsilon)^+ (\mathcal{H} - \epsilon) | \phi_i \rangle. \quad (\text{A.6})$$

This norm possesses a quadratic minimum at each eigenfunction  $\phi_i$  of the hamiltonian  $\mathcal{H}$ . Knowing this, the direct inversion in the iterative subspace, also known as Pulay mixing, is used to find the minima [105, 106].

Pulay proposed to update the parameters of a quadratic problem by linear combination of previous approximations of the parameters

$$\left\{ \phi_i^m = \sum_{k=1}^{m-1} c_k \phi_i^k, i = 1 \dots N_{\text{bands}} \right\} \quad (\text{A.7})$$

where the first step, or all steps as long as the system is not in the quadratic region, is done by using an approximate Hessian  $\mathcal{H}_0$

$$\phi_i^1 = \phi_i^0 - \mathcal{H}_0^{-1} \left. \frac{\partial \langle R_i | R_i \rangle}{\partial \phi_i} \right|_{\phi_i = \phi_i^0} \quad (\text{A.8})$$

The residuum vector is also approximated as a linear combination

$$|R_i^m\rangle = \sum_{k=1}^{m-1} c_k |R_i^k\rangle \quad (\text{A.9})$$

and the condition

$$\sum_{k=1}^{m-1} c_k = 1 \quad (\text{A.10})$$

has to hold. This leads to the Lagrangian

$$\mathcal{L} = \sum_{k,l=1}^{m-1} c_k B_{kl} c_l - \lambda \left( \sum_{k=1}^{m-1} c_k - 1 \right), \quad \text{with} \quad B_{kl} = \langle R_i^k | R_i^l \rangle \quad (\text{A.11})$$

with the Lagrange parameter  $\lambda$  enforcing the constraint Eq. A.10 to be fulfilled. This set of only  $m$  equations can be solved without big computational effort providing a new set of  $c_k$ . The DIIM method (Eq. A.7, A.9, and A.11) is iterated until convergence. A great advantage of this method is that each band  $\phi_i$  can be optimized independently of all other bands. Thus, if one cpu computes one or more bands, no communication between the cpus are necessary. However, a Gram-Schmidt orthogonalization over the  $\phi_i$  is necessary each time all bands have been updated, since otherwise all bands will converge to the lowest one.

## A.2. Charge mixing methods

### A.2.1. Broyden Mixing

The Broyden mixing [107, 41] treats the charge density update very similarly to a pseudo Newton scheme, by iteratively finding the Jacobian

$$\mathcal{J} = \frac{\partial R(n)}{\partial n} \quad (\text{A.12})$$

with the residual  $R(n) = F(n) - n$ , where  $F(n)$  is a functional of the old charge density evaluating the new charge density. The ground state charge density obviously satisfies  $R(n) = 0$ . The new charge density  $n_{j+1}$  can be calculated from the old charge density  $n_j$  by

$$n_{j+1} = n_j + \mathcal{J}_j^{-1} R(n_j). \quad (\text{A.13})$$

Starting from an initial guess, the Jacobian is updated each step together with the charge density, since the Jacobian is neither known nor easily invertible. The new Jacobian is chosen such that the previous step is still reproduced and the norm of the change in the Jacobi matrix  $Q = \left| \mathcal{J}_{j+1}^{-1} - \mathcal{J}_j^{-1} \right|$  is minimized. The resulting update of the Jacobian is

$$\mathcal{J}_{j+1}^{-1} = \mathcal{J}_j^{-1} \frac{(\delta n_{j+1} - \mathcal{J}_j^{-1} \delta R_{j+1}) \delta R_{j+1}}{\langle \delta R_{j+1} | \delta R_{j+1} \rangle} \quad (\text{A.14})$$

with the change in charge density  $\delta n_{j+1} = n_{j+1} - n_j$  and the change of the residual  $\delta R_{j+1} = R_{j+1} - R_j$ .

### A.2.2. Kerker Mixing

In the Kerker Mixing scheme, the charge density is mixed in momentum space and is updated by

$$n_{ij+1}(q) = n_{j|in}(q) + \alpha \frac{|q|^2}{|q|^2 + q_0^2} (n_{j|out}(q) - n_{j|in}(q)). \quad (\text{A.15})$$

Here  $\alpha$  and  $q_0$  are mixing parameters and  $n_{j|in}$  denotes the input charge density of the iteration step  $j$  and  $n_{j|out}$  respectively the updated charge density after step  $j$ .

### A.3. Consideration of ion fixing for the barrier height in strained zirconium oxide

To determine the contribution of the motion of specific ions in the jump process to the overall barrier height, a series of constrained NEB calculations has been conducted. The results are presented in Tab. A.1, which refers to the numbering of ions in Fig. A.1.

Only the configurations fixed20, fixed22 and fixed24 show the drop of the migration barrier under compression in the considered strain domain. It can be expected that the configurations fixed17 and fixed18 also show this qualitative behavior since the effect of the fixed ions is marginal at  $\sigma = 0.914$ .

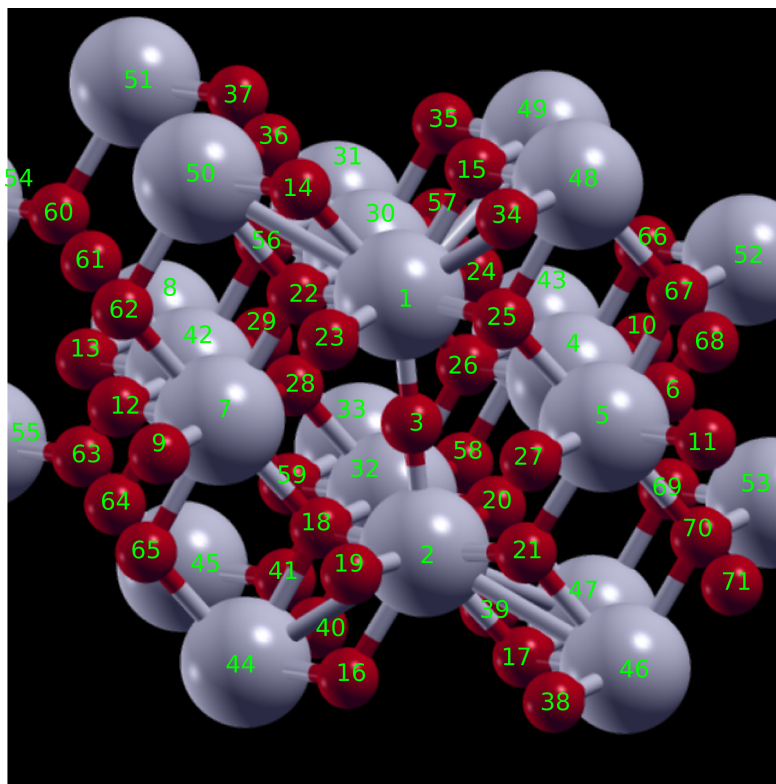


**Figure A.1.:** Configuration of the zirconia lattice at the barrier position with indices for all ions in the visible lattice. The jumping oxygen ion (ion 3) is located between the two zirconium ions 1 and 2.

Reference	Configuration (not fixed ions)	$\Delta E$ ( $\sigma = 0.914$ )	$\Delta E$ ( $\sigma = 0.86$ )
free	all	1.274	-0.02
fixed0	1-3, 14-17		2.619
fixed1	1-17	1.595	2.237
fixed2	fixed1, 18-25	1.525	2.071
fixed3	fixed1, 26-29	1.586	
fixed4	1-9, 14-17	1.625	
fixed5	1-5, 7-8, 10-17	1.616	
fixed6	1-13	1.89	
fixed7	1-3, 6, 9-17	1.642	
fixed8	3-17	2.59	
fixed9	fixed1, 30-33	1.5923	
fixed10	fixed1, 34-41	1.5948	
fixed11	1, 2, all $O^{2-}$	1.569	2.484
fixed12	fixed1, all $O^{2-}$	1.494	1.9255
fixed13	fixed11, 30-33	1.555	
fixed14	fixed11, <i>Zr</i> -ion between 1,2 (*)	1.569	
fixed15	fixed12, 30-33	1.4866	
fixed16	fixed15, 42, 43	1.4858	
fixed17	fixed16, 44-51	1.2954	
fixed18	fixed17, 52-55	1.2795	
fixed19	fixed1, 44-51	1.549	
fixed20	fixed19, all $O^{2-}$	1.323	0.176
fixed21	fixed19, 18-25	1.433	1.4423
fixed22	fixed21, 26-29	1.423	1.4078
fixed23	fixed22, without 4, 5, 7, 8	1.562	2.411
fixed24	fixed22, 34-41	1.4213	1.407
fixed25	fixed19, 26-29	1.539	1.914
fixed26	fixed25, without 10-13	1.585	2.2505

**Table A.1.:** Fixing of ion sets in the determination of the migration barrier. The configuration denotes which ions in the lattice are not fixed in the calculation. The numbering refers to Fig. A.1. Not all configuration has been calculated at both strains. (\*: This is the zirconium ion lying between 1 and 2 connected over the boundary conditions. It is not visible in the picture.)

## Bibliography

- [1] R. Hansch, M.R.R. Chowdhury, and N.H. Menzler, “Screen printing of sol-gel-derived electrolytes for solid oxide fuel cell (SOFC) application”, *Ceram. Int.* **35**, 803 (2008).
- [2] K. Suzuki, M. Kubo, Y. Oumi, R. Miura, H. Takaba, A. Fahmi, A. Chatterjee, K. Teraishi, and A. Miyamoto, “Molecular dynamics simulation of enhanced oxygen ion diffusion in strained yttria-stabilized zirconia”, *Appl. Phys. Lett.* **73**, 1502-1504 (1998).
- [3] C. Korte, A. Peters, J. Janek, D. Hesse, and N. Zakharov, “Ionic conductivity and activation energy for oxygen ion transport in superlattices—the semicoherent multilayer system YSZ ( $ZrO_2 + 9.5 \text{ mol\% } Y_2O_3$ )/ $Y_2O_3$ ”, *Phys. Chem. Chem. Phys.* **10**, 4623-4635 (2008).
- [4] N. Schichtel, C. Korte, D. Hesse, and J. Janek, “Elastic strain at interfaces and its influence on ionic conductivity in nanoscaled solid electrolyte thin films—theoretical considerations and experimental studies” *Phys. Chem. Chem. Phys.* **11**, 3043-3048 (2009).
- [5] W. Araki, Y. Imai, and T. Adachi, “Mechanical stress effect on oxygen ion mobility in 8 mol% yttria-stabilized zirconia electrolyte”, *J. Eur. Ceram. Soc.* **29**, 2275-2279 (2009).
- [6] A. Kushima and B. Yildiz, “Oxygen ion diffusivity in strained yttria stabilized zirconia: where is the fastest strain?”, *J. Mater. Chem.* **20**, 4809-4819 (2010).
- [7] M. Sillassen, P. Eklund, N. Pryds, E. Johnson, U. Helmersson, and J. Böttiger, “Low-Temperature Superionic Conductivity in Strained Yttria-Stabilized Zirconia”, *Adv. Funct. Mater.* **20**, 2071-2076 (2010).
- [8] K. Sato, K. Suzuki, R. Narumi, K. Yashiro, T. Hashida, and J. Mizusaki, “Ionic Conductivity in Uniaxial Micro Strain/Stress Fields of Yttria-Stabilized Zirconia”, *Jpn. J. Appl. Phys.* **50**, 055803 (2011).
- [9] I. Kosacki, C. M. Rouleau, P. F. Becher, J. Bentley, and D. H. Lowndes, “Nanoscale effects on the ionic conductivity in highly textured YSZ thin films”, *Solid State Ionics* **176**, 1319-1326 (2005).
- [10] T. J. Pennycook, M. J. Beck, K. Varga, M. Varela, S. J. Pennycook, and S. T. Pantelides, “Origin of Colossal Ionic Conductivity in Oxide Multilayers: Interface Induced Sublattice Disorder”, *Phys. Rev. Lett.* **104**, 115901 (2010).

- [11] N. Schichtel, C. Korte, D. Hesse, N. Zakharov, B. Butz, D. Gerthsen, and J. Janek, "On the influence of strain on ion transport: microstructure and ionic conductivity of nanoscale YSZ| $Sc_2O_3$  multilayers", *Phys. Chem. Chem. Phys.*, **12**, 14596-14608 (2010).
- [12] J. Garcia-Barriocanal, A. Rivera-Calzada, M. Varela, Z. Sefrioui, E. Iborra, C. Leon, S. J. Pennycook, and J. Santamaria, "Colossal Ionic Conductivity at Interfaces of Epitaxial  $ZrO_2 : Y_2O_3 / SrTiO_3$  Heterostructures", *Science* **321**, 676-680 (2008).
- [13] E. Fabbri, D. Pergolesi, and E. Traversa, "Ionic conductivity in oxide heterostructures: the role of interfaces", *Sci. Technol. Adv. Mater.* **11**, 054503 (2010).
- [14] G. H. Vineyard, "Frequency factors and isotope effects in solid state rate processes", *J. Phys. Chem. Solids* **3**, 121-127 (1957).
- [15] D. Sheppard, R. Terrell, and G. Henkelman, "Optimization methods for finding minimum energy paths", *J. Chem. Phys.* **128**, 134106 (2008).
- [16] G. Henkelman, B. P. Uberuaga and H. Jónsson, "A climbing image nudged elastic band method for finding saddle points and minimum energy paths", *J. Chem. Phys.* **113**, 9978 (2000).
- [17] G. Henkelman, G. Jóhannesson, and H. Jónsson, "Nudged elastic band method for finding minimum energy paths of transitions", in *Theoretical Methods in Condensed Phase Chemistry*, edited by S.D. Schwartz (Kluwer Academic Press, 2002), p. 269-300
- [18] N. Metropolis, A. W. Rosenbluth, M. N. Rosenbluth, A. H. Teller, and E. J. Teller, "Equation of State Calculations by Fast Computing Machines", *J. Chem. Phys.* **21**, 1087-1092 (1953).
- [19] A. S. Fraser, "Simulation of Genetic Systems by Automatic Digital Computers", *Aust. J. Biol. Sci.* **10**, 484-491 (1957).
- [20] J. A. Hirschfeld, *Tomographic problems in the diagnostics of fuel cell stacks* (Diploma thesis, Universität Duisburg-Essen, 2008).
- [21] C. E. Mortimer and U. Müller, *Chemie*, (Georg Thieme Verlag, Stuttgart, 2003)
- [22] Eduard Job Foundation; [www.job-stiftung.de](http://www.job-stiftung.de)
- [23] W. Vielstich, A. Lamm, and H. A. Gasteiger, *Handbook of fuel cells Vol. 1*, (John Wiley & Son Ltd., West Sussex, 2003)
- [24] L. J. M. J. Blomen, and M.N. Mugerwa, *Fuel Cell Systems*, (Plenum Press, New York, 1993)

- [25] C. Rayment and S. Sherwin, *Introduction to fuel cell technology*, (University of Notre Dame, 2003)
- [26] Freedom CAR & Vehicle Technologies Program. U.S. Department of Energy, 2003, “Just the Basics: Diesel Engine”, [http://www1.eere.energy.gov/vehiclesandfuels/pdfs/basics/jtb\\_diesel\\_engine.pdf](http://www1.eere.energy.gov/vehiclesandfuels/pdfs/basics/jtb_diesel_engine.pdf)
- [27] K. Wippermann, *Brennstoffzellen - Eine Zukunftstechnologie?*, (lecture notes FH Aachen, 2004)
- [28] [http://www.fz-juelich.de/SharedDocs/Pressemitteilungen/UK/DE/2012/12-03-19Rekord\\_SOFC.html](http://www.fz-juelich.de/SharedDocs/Pressemitteilungen/UK/DE/2012/12-03-19Rekord_SOFC.html)
- [29] K. Kordesch and G. Simader, *Fuel Cells and Their Applications*, (VCH Verlagsgesellschaft GmbH, Weinheim, 1996).
- [30] A. Gierlich, *All-Electron GW Calculations for Perovskite Transition-Metal Oxides* (PhD thesis, RWTH Aachen, 2011).
- [31] D.R. Hartree, “Creating The wave mechanics of an atom with a non-Coulomb central field”, *Mathematical Proceedings of the Cambridge Philosophical Society*, **24**, 89-110 (1928).
- [32] L. H. Thomas, “The calculation of atomic fields”, *Mathematical Proceedings of the Cambridge Philosophical Society* **23**, 542 (1927).
- [33] E. Fermi, “Eine statistische Methode zur Bestimmung einiger Eigenschaften des Atoms und ihre Anwendung auf die Theorie des periodischen Systems der Elemente.”, *Atti Accad. Naz. Lincei, Cl. Sci. Fis. , Mat. Nat.* **6**, 602 (1927).
- [34] R.Zeller, in *Computational Condensed Matter Physics*, Schriften des Forschungszentrums Jülich, Vol. **32**, edited by S. Blügel, G. Gompper, E. Koch, H. Müller- Krumbhaar, R. Spatschek, and R. Winkler (Forschungszentrum Jülich GmbH, 2006).
- [35] P. Hohenberg and W. Kohn, “Inhomogeneous Electron Gas”, *Phys. Rev.* **136**, B864 (1964).
- [36] M. Levy, “Universal variational functionals of electron densities, first-order density matrices, and natural spin-orbitals and solution of the v-representability problem”, *Proceedings of the National Academy of Sciences of the United States of America* **76**, 6062 (1979).
- [37] W. Kohn and L. J. Sham, “Self-Consistent Equations Including Exchange and Correlation Effects”, *Phys. Rev.* **140**, A1133 (1965).
- [38] D. M. Ceperley and B. J. Alder, “Ground State of the Electron Gas by a Stochastic Method”, *Phys. Rev. Lett.* **45**, 566 (1980).

- [39] J. P. Perdew and Y. Wang, “Accurate and simple analytic representation of the electron-gas correlation energy”, *Phys. Rev. B* **45**, 13244 (1992).
- [40] J. P. Perdew, K. Burke and M. Ernzerhof, “Generalized Gradient Approximation Made Simple”, *Phys. Rev. Lett.* **77**, 3865 (1996).
- [41] H. Toffoli, *Principles of Density Functional Theory*, (Lecture Scripts - Middle East Technical University)
- [42] J. Hafner, “Ab-Initio Simulations of Materials Using VASP: Density-Functional Theory and Beyond”, *J. Comput. Chem.* **29**, 2044–2078 (2008).
- [43] VASP Users manual <http://cms.mpi.univie.ac.at/vasp/vasp/vasp.html>
- [44] C. C. Broyden, “A Class of Methods for Solving Nonlinear Simultaneous Equations”, *Math. Comp.* **19**, 577-593 (1965).
- [45] G. P. Kerker, “Efficient iteration scheme for self-consistent pseudopotential calculations”, *Phys. Rev. B* **23**, 3082–3084 (1981).
- [46] E. Bitzek, P. Koskinen, F. Gähler, M. Moseler, and P. Gumbsch, “Structural Relaxation Made Simple”, *Phys. Rev. Lett.* **97**, 170201 (2006).
- [47] P. E. Blöchl, C. J. Förster, and J. Schimpl, “Projector augmented wave method: ab initio molecular dynamics with full wave functions”, *Bull. Mater. Sci.* **26**, 33–41 (2003).
- [48] This picture, or part of this picture has been done with the atomic view XCrysDen – A. Kokalj, “Computer graphics and graphical user interfaces as tools in simulations of matter at the atomic scale”, *Comp. Mater. Sci.* **28**, 155 (2003).; Code available from <http://www.xcrysden.org/>
- [49] J. A. Hirschfeld and H. Lustfeld, “Finding stable minima using a nudged-elastic-band-based optimization scheme”, *Phys. Rev. E* **85**, 056709 (2012).
- [50] R. O. Jones and D. J. Hohl, “Structure of phosphorus clusters using simulated annealing—P<sub>2</sub> to P<sub>8</sub>”, *J. Chem. Phys.* **92**, 6710 (1990).
- [51] S. Hwang and R. Smith, “Application of simulated annealing (SA) to the synthesis of heterogeneous catalytic reactor”, *Korean J. Chem. Eng.* **29**, 25-35 (2012).
- [52] C. C. Queirolo, L. Silva, O. R.P. Bellon, and M. P. Segundo, “3D Face Recognition Using Simulated Annealing and the Surface Interpenetration Measure”, *IEEE Trans. Pattern Anal. Mach. Intell.* **32**, 206-219 (2010).
- [53] S.-H. Yanga, J. Srinivasa, S. Mohana, D.-M. Leea, and S. Balajib, “Optimization of electric discharge machining using simulated annealing”, *J. Mater. Process. Technol.* **209**, 4471-4475 (2009).

- [54] A. Tabatabaeenejad and M. Moghaddam, "Inversion of Subsurface Properties of Layered Dielectric Structures With Random Slightly Rough Interfaces Using the Method of Simulated Annealing", *IEEE Trans. Geosci. Remote Sens.* **47**, 2035-2046 (2009).
- [55] A. D. Stivala, P. J. Stuckey, and A. I. Wirth, "Fast and accurate protein substructure searching with simulated annealing and GPUs", *BMC Bioinformatics* **11**, 446 (2010).
- [56] J. S. Liu, A. J. Caley, A. J. Waddie, and M. R. Taghizadeh, "Comparison of simulated quenching algorithms for design of diffractive optical elements", *Appl. Optics* **47**, 807-816 (2008).
- [57] X. Zhou, J. Zhao, X. Chen, and W. Lu, "Structural and electronic properties of  $Sb_n$  ( $n=2-10$ ) clusters using density-functional theory", *Phys. Rev. A* **72**, 053203 (2005).
- [58] G. H. Jóhannesson, T. Bligaard, A. V. Ruban, H. L. Skriver, K. W. Jacobsen, and J. K. Nørskov, "Combined Electronic Structure and Evolutionary Search Approach to Materials Design", *Phys. Rev. Lett.* **88**, 255506 (2002).
- [59] W. Cheah and M. W. Finnis, "Structure of multilayer  $ZrO_2/SrTiO_3$ ", *J. Mater. Sci.* **47**, 1631-1640 (2012).
- [60] G. Seifert and R. O. Jones, "Structure of phosphorus clusters by simulated annealing", *Z. Phys. D.* **26**, 349-351 (1993).
- [61] M. D. Chen, R. B. Huang, L. S. Zheng, and C. T. Au, "The prediction of isomers for phosphorus clusters  $P_8$  and  $P_9$ ", *J. Mol. Struct. -Theochem* **499**, 195-201, (2000).
- [62] M. D. Chen, J. T. Li, R. B. Huang, L. S. Zheng, and C. T. Au, "Structure prediction of large cationic phosphorus clusters", *Chem. Phys. Lett.* **305**, 439-445, (1999).
- [63] B. M. Gimarc and S. Warren, "Relative Energies and Strain Energies of Proposed Structures for  $P_8$ ", *Inorg. Chem.* **32**, 1850-1856 (1992).
- [64] R. Janoschek, "Die hypothetischen Phosphor-Cluster  $P_6$  und  $P_8$  - welche Isomeren waren die stabilsten?", *Chem. Ber.* **125**, 2687-2689 (1992).
- [65] V. Kumar, "Electronic and atomic structures of  $Sb_4$  and  $Sb_5$  clusters", *Phys. Rev. B* **48**, 8470, (1993).
- [66] V. Sundararaman and V. Kumar, "Ab initio molecular dynamics study of antimony clusters", *J. Chem. Phys.* **102**, 9631 (1995).
- [67] J. B. Goodenough, "Oxide-Ion Electrolytes", *Annu. Rev. Mater. Res.* **33**, 91-128 (2003).
- [68] F. Tietz, private communication.

- [69] E. Ivers-Tiffée, A. Weber, and D Herbstritt, “Materials and technologies for SOFC-components”, *Journal of the European Ceramic Society* **21**, 1805–1811 (2001).
- [70] J. Emsley, *”Yttrium”. Nature’s Building Blocks: An A-Z Guide to the Elements.* (Oxford University Press, Oxford) 495–498 (2001).
- [71] Mineralinfo.org; <http://www.mineralinfo.org/Substance/Scandium/Sc.pdf>
- [72] [www.metal-pages.com](http://www.metal-pages.com/metalprices/yttrium/); <http://www.metal-pages.com/metalprices/yttrium/>
- [73] S. J. Skinner and J. A. Kilner, “Oxygen ion conductors”, *materials today* **6**, 30–37 (2003).
- [74] E. V. Tsipis and V. V. Kharton, “Electrode materials and reaction mechanisms in solid oxide fuel cells: a brief review”, *J. Solid State Electrochem.* **12**, 1039–1060 (2008).
- [75] P. Aldebert and J-P. Traverse, “Structure and Ionic Mobility of Zirconia at High Temperature”, *J. Am. Ceram. Soc.* **68**, 34-40 (1985).
- [76] F. Birch, “Finite Elastic Strain of Cubic Crystals”, *Physical Review* **71**, 809–824 (1947).
- [77] A. P. Bechepeche, O. Treu Jr., E. Longo, C. O. Paiva-Santos, and J. A. Varela, “Experimental and theoretical aspects of the stabilization of zirconia.”, *Journal of Material Science* **34**, 2751 – 2756 (1999).
- [78] R. H. French, S. J. Glass, F. S. Ohuchi, Y. N. Xu, and W. Y. Ching, “Experimental and theoretical determination of the electronic structure and optical properties of three phases of  $ZrO_2$ ”, *Phys. Rev. B.* **49**, 5133 (1994).
- [79] C. R. Aita and C. K. Kwok, “Fundamental Optical Absorption Edge of Sputter-Deposited Zirconia and Yttria”, *J. Am Ceram. Soc.* **73**, 3209 (1990).
- [80] E. V. Stefanovich, A. L. Shluger, and C. R. A. Catlow, “Theoretical study of the stabilization of cubic-phase  $ZrO_2$  by impurities”, *Phys. Rev. B* **49**, 11560 (1994).
- [81] S. A. Ostanin and E. I. Salamatov, “Microscopic Mechanism of Stability in Yttria-Doped Zirconia”, *JETP Letters* **74**, 552–555 (2001).
- [82] T. Bredow, “Theoretical investigation of nitrogen substitution in cubic zirconia”, *Phys. Rev. B* **75**, 144102 (2007).
- [83] M. Hillert and T. Sakuma, “Thermodynamic modeling of the c  $\rightarrow$  t transformation in  $ZrO_2$  alloys”, *Acta Metall. Mater.* **39**, 1111 (1991).
- [84] S. Fabris, A. T. Paxton, M. W. Finnis, “A stabilization mechanism of zirconia based on oxygen vacancies only”, *Acta Materialia* **50**, 5171–5178 (2002).

- [85] J. X. Zheng, G. Ceder, T. Maxisch, W. K. Chim, and W. K. Choi, "First-principles study of native point defects in hafnia and zirconia", *Phys. Rev. B* **75**, 104112 (2007).
- [86] A. I. Ioffe, D. S. Rutman, and S. V. Karpachov, "On the Nature of the Conductivity Maximum in Zirconia-Based Solid Electrolytes", *Electrochim. Acta* **23**, 141 (1978).
- [87] A. Eichler, "Tetragonal Y-doped zirconia: Structure and ion conductivity", *Phys. Rev. B* **64**, 174103 (2001).
- [88] S. Kasamatsu, T. Tada, and S. Watanabe, "Comparative Study of Charged and Neutral Oxygen Vacancies in Cubic Zirconia from First Principles", *Appl. Phys. Expr.* **2**, 061402 (2009).
- [89] G. Stapper, M. Bernasconi, N. Nicoloso, and M. Parrinello, "Ab initio study of structural and electronic properties of yttria-stabilized cubic zirconia", *Phys. Rev. B* **59**, 797-810 (1999).
- [90] R. Pornpasertsuk, P. Ramanarayanan, C.B. Musgrave, and F.B. Prinz, "Predicting ionic conductivity of solid oxide fuel cell electrolyte from first principles", *J. Appl. Phys.* **98**, 103513 (2005).
- [91] J. A. Hirschfeld and H. Lustfeld, "First-principles study and modeling of strain-dependent ionic migration in  $ZrO_2$ ", *Phys. Rev. B* **84**, 224308 (2011).
- [92] R. Krishnamurthy, Y.-G. Yoon, D.J. Srolovitz, and R. Car, "Oxygen Diffusion in Yttria-Stabilized Zirconia: A New Simulation Model", *J. Am. Ceram. Soc.* **87**, 1821-1830 (2004).
- [93] R.J. Hemley and N.W. Ashcroft, "The Revealing Role of Pressure in the Condensed Matter Sciences", *Phys. Today* **51**, 26 (1998).
- [94] J. Li, S. Meng, J. Han, and X. Zhang, "Valence electron structure and properties of the  $ZrO_2$ ", *Sci. China Ser. E.* **51**, 1858-1866 (2008).
- [95] R. Devanathan, W. J. Weber, S. C. Singhal, and J. D. Gale, "Computer simulation of defects and oxygen transport in yttria-stabilized zirconia", *Solid State Ionics* **177**, 1251-1258 (2006).
- [96] E. Lee, F. B. Prinz, and W. Cai, "Enhancing ionic conductivity of bulk single-crystal yttria-stabilized zirconia by tailoring dopant distribution", *Phys. Rev. B* **83**, 052301 (2011).
- [97] R. Krishnamurthy, D. J. Srolovitz, K. N. Kudin, and R. Car, "Effects of Lanthanide Dopants on Oxygen Diffusion in Yttria-Stabilized Zirconia", *J. Am. Ceram. Soc.*, **88**, 2143-2151 (2005).

- [98] A. Predith, G. Ceder, C. Wolverton, K. Persson, and T. Mueller, “Ab initio prediction of ordered ground-state structures in  $ZrO_2$ - $Y_2O_3$ ”, Phys. Rev. B **77**, 144104 (2008).
- [99] A. Bogicevic and C. Wolverton, “Nature and strength of defect interactions in cubic stabilized zirconia”, Phys. Rev. B **67**, 024106 (2003).
- [100] M. Kilo, C. Argirusis, G. Borchardt, and R. A. Jackson, “Oxygen diffusion in yttria stabilised zirconia—experimental results and molecular dynamics calculations”, Phys. Chem. Chem. Phys. **5**, 2219–2224 (2003).
- [101] X. Li and B. Hafskjold, “Molecular dynamics simulations of yttrium-stabilized zirconia”, J. Phys.: Condens. Matter **7**, 1255 (1995).
- [102] V. Thangadurai and W. Weppner, “Recent progress in solid oxide and lithium ion conducting electrolytes research”, Ionics **12**, 81–92 (2006).
- [103] F. Krok, I. Abrahams, W. Wrobel, A. Kozanecka-Szmigiel, and J. R. Dygas, “Oxide-ion conductors for fuel cells”, Materials Science-Poland **24**, 13 – 23 (2006).
- [104] E. R. Davidson, “The iterative calculation of a few of the lowest eigenvalues and corresponding eigenvectors of large real-symmetric matrices”, J. Comput. Phys. **17**, 87–94 (1975).
- [105] P. Pulay, “Convergence acceleration of iterative sequences. the case of scf iteration”, Chem. Phys. Lett. **73**, 393 (1980).
- [106] D. M. Wood and A. Zunger, “A new method for diagonalising large matrices”, J. Phys. A: Math. Gen. **18**, 1343-1359 (1985).
- [107] D. Heidarian, *Metal-Insulator Transitions in Two Dimensions*, (PhD thesis - School of Natural Sciences, Tata Institute of Fundamental Research, Mumbai, 2006)

## **Acknowledgements**

I would like to thank my supervisor PD. Dr. Hans Lustfeld for his patience and his massive confidence in me. But especially I thank him for always finding time to discuss my problems and advise me in solving them. The cooperation with him was always efficient and very fruitful.

Furthermore, I want to thank Prof. Dr. Stefan Blügel to enable me to do my PhD research in his institute, for supporting my work and raising funds for my position.

Special thanks go to my girlfriend Mei Ding for always supporting me, especially in the times of writing down this thesis. Furthermore, I thank her for her help concerning the abstract in Chinese language.

The DFT calculations have been performed on the supercomputer JUROPA at the Jülich Supercomputing Center with a grant from the FZ-Jülich.